

ND-R100 719

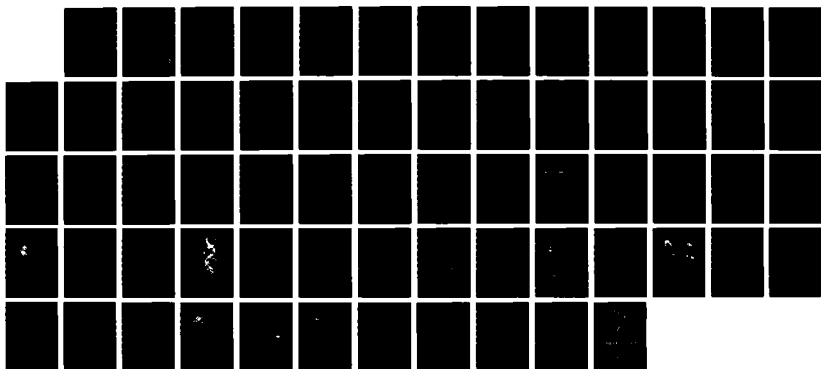
THE EFFECTS OF OPTICAL SMOOTHING TECHNIQUES ON  
FILAMENTATION IN LASER PLASMAS (U) NAVAL RESEARCH LAB  
WASHINGTON DC A J SCHMITT 29 DEC 87 NRL-MR-6142

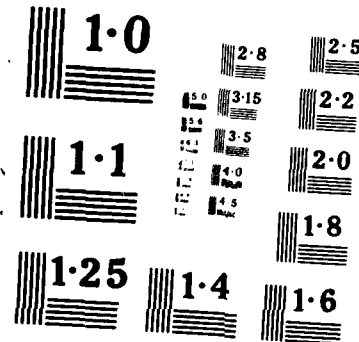
1/1

UNCLASSIFIED

F/G 20/6

ML





Naval Research Laboratory

Washington, DC 20375-5000

DTIC FILE COPY



NRL Memorandum Report 6142

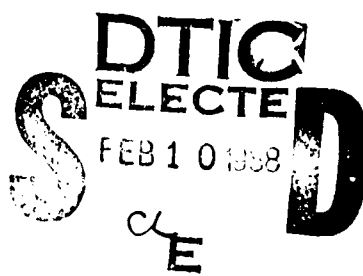
## The Effects of Optical Smoothing Techniques on Filamentation in Laser Plasmas

ANDREW J. SCHMITT

*Laser Plasma Branch  
Plasma Physics Division*

AD-A 188 719

December 29, 1987



## REPORT DOCUMENTATION PAGE

Form Approved  
OMB No 0704-0188

1a. REPORT SECURITY CLASSIFICATION UNCLASSIFIED		1b. RESTRICTIVE MARKINGS			
2a. SECURITY CLASSIFICATION AUTHORITY		3. DISTRIBUTION/AVAILABILITY OF REPORT Approved for public release; distribution unlimited.			
2b. DECLASSIFICATION/DOWNGRADING SCHEDULE					
4. PERFORMING ORGANIZATION REPORT NUMBER(S) NRL Memorandum Report 6142		5. MONITORING ORGANIZATION REPORT NUMBER(S)			
6a. NAME OF PERFORMING ORGANIZATION Naval Research Laboratory	6b. OFFICE SYMBOL (If applicable) Code 4730	7a. NAME OF MONITORING ORGANIZATION			
6c. ADDRESS (City, State, and ZIP Code) Washington, DC 20375-5000		7b. ADDRESS (City, State, and ZIP Code)			
8a. NAME OF FUNDING/SPONSORING ORGANIZATION Department of Energy	8b. OFFICE SYMBOL (If applicable)	9. PROCUREMENT INSTRUMENT IDENTIFICATION NUMBER			
8c. ADDRESS (City, State, and ZIP Code) Washington, DC 20545		10. SOURCE OF FUNDING NUMBERS			
		PROGRAM ELEMENT NO	PROJECT NO	TASK NO	WORK UNIT ACCESSION NO
11. TITLE (Include Security Classification) The Effects of Optical Smoothing Techniques on Filamentation in Laser Plasmas					
12. PERSONAL AUTHOR(S) Schmitt, Andrew J.					
13a. TYPE OF REPORT Interim	13b. TIME COVERED FROM 10/86 TO 10/87	14. DATE OF REPORT (Year, Month, Day) 1987 December 29		15. PAGE COUNT 55	
16. SUPPLEMENTARY NOTATION					
17. COSATI CODES		18. SUBJECT TERMS (Continue on reverse if necessary and identify by block number) Laser plasma interaction Inertial confinement fusion			
19. ABSTRACT (Continue on reverse if necessary and identify by block number) The effect of the induced-spatial-incoherence (ISI) and the random-phase-screen (RPS) optical smoothing techniques on the filamentation instability in laser plasmas has been investigated numerically and analytically. A two-dimensional time-dependent laser-plasma propagation code, including both ponderomotive and thermal-conduction dominated filamentation, is used to simulate the laser-plasma interaction. The results of these simulations are compared to the predictions of a simple theory that describes the filamentation of both coherent light and spatially and temporally incoherent light. It is shown that filaments driven by the thermal mechanisms tend to cluster together and produce greater large-scale nonuniformities in the laser illumination than the ponderomotively-driven filaments. The RPS optical smoothing technique is found to reduce filamentation only if fast focusing optics ( $F \leq 5$ ) are used. The ISI smoothing method suppresses filamentation for fast or slow focusing optics, and requires only moderate laser bandwidth ( $\Delta\omega/\omega = 0.1\%$ ). In general, the ISI smoothing method provides the best suppression of filamentation. Under common laboratory conditions, filamentation is pronounced at longer laser wavelengths ( $1.06 \mu m - 0.53 \mu m$ ), suggesting that current experiments may be dominated by filamentation effects. Optical smoothing methods can suppress, but not eradicate, filamentation effects at these wavelengths.					
20. DISTRIBUTION AVAILABILITY OF ABSTRACT <input checked="" type="checkbox"/> UNCLASSIFIED UNLIMITED <input type="checkbox"/> SAME AS RPT <input type="checkbox"/> DTC USERS			21. ABSTRACT SECURITY CLASSIFICATION UNCLASSIFIED		
22a. NAME OF RESPONSIBLE INDIVIDUAL Andrew J. Schmitt			22b. TELEPHONE (Include Area Code) (404) 767-3681   Code 4730		

19. ABSTRACT (Continued)

The optical smoothing methods are most effective in short-wavelength (0.25  $\mu\text{m}$ ) laser-driven plasmas. At 0.25  $\mu\text{m}$  laser wavelength, ISI is found to completely eliminate filamentation effects in both time-averaged and instantaneous intensity distribution.

Accession For	
NTIS GRA&I	<input checked="" type="checkbox"/>
DTIC TAB	<input type="checkbox"/>
Unannounced	<input type="checkbox"/>
Justification	
By	
Distribution/	
Availability Codes	
Dist	Avail and/or Special
A-1	



## CONTENTS

I.	INTRODUCTION .....	1
II.	GOVERNING EQUATIONS AND NUMERICAL DESCRIPTION .....	3
	A. Light Propagation .....	3
	B. Plasma Response .....	4
III.	ANALYTIC FORMULATION OF FILAMENTATION .....	8
	A. Basic theory of filamentation .....	8
	B. ISI and filamentation .....	9
IV.	ANALYSIS AND DISCUSSION .....	11
	A. Filamentation in Homogeneous, Nonabsorbing Plasmas:	
	Gaussian Filaments .....	11
	B. Filamentation in Homogeneous, Nonabsorbing Plasmas:	
	Complex Laser Beams .....	13
	i. Definition and Construction of Complex Laser Beams .....	13
	ii. Filamentation of Generic Laser Beams .....	15
	iii. Filamentation of RPS Laser Beams .....	16
	iv. Filamentation of ISI Laser Beams .....	16
	C. Filamentation of Complex Laser Beams in Laboratory Plasmas .....	18
V.	CONCLUSIONS .....	21
	ACKNOWLEDGEMENTS .....	22
	APPENDIX .....	23
	A.1 Ponderomotive Filamentation .....	23
	A.2 Thermal Filamentation .....	24
	REFERENCES .....	27
	TABLE I .....	29
	TABLE II .....	30
	FIGURES .....	31

# THE EFFECTS OF OPTICAL SMOOTHING TECHNIQUES ON FILAMENTATION IN LASER PLASMAS

## I. Introduction

The production of uniform laser illumination has been a fundamental concern in the laser-fusion community for many years. The quality of the laser-plasma coupling and symmetry of the pellet implosion are dependent on the illumination uniformity. Illumination uniformity analysis can be divided naturally into large and small scale categories. Large scale illumination uniformity is primarily determined by the gross intensity profile of the incident laser beams, the inter-beam energy balance, and the geometry of the targeting on the pellet. This aspect of the uniformity problem has been previously addressed, and the results indicate that the gross uniformity can probably be controlled to within tolerable limits<sup>1,2</sup>. The detailed structure of the individual laser beam is responsible for small scale nonuniformities, and is more difficult to suppress or control. The laser-plasma filamentation instability is seeded by these small scale nonuniformities and tends to increase the nonuniformity, exacerbating the problem.

The filamentation instability is a nonlinear optical effect that has been studied for many years.<sup>3</sup> Filamentation is caused by perturbations or nonuniformities in light that produce local changes in the dielectric constant, or index of refraction, of a medium. If the change in the dielectric constant is positive in regions of higher intensity, a focusing lens is produced there. This increases the perturbation and starts the instability. The instability will saturate when the focusing tendency of the intensity hot spot is balanced by diffraction, but at this point the filament intensity may be orders of magnitude higher than the initial perturbation.

In laser plasmas, there are a variety of mechanisms that give rise to an intensity-dependent dielectric constant and produce filamentation. Among these are ponderomotive force effects<sup>4,5</sup>, plasma heating or thermal effects<sup>6</sup>, and relativistic effects.<sup>7</sup> The ponderomotive and thermal effects change the dielectric constant by expelling the plasma density from the high intensity region; these mechanisms are active in laser-fusion plasmas. The relativistic mechanism affects the dielectric constant via the increase in electron mass from the relativistic quiver velocity in the electromagnetic wave; this is generally unimportant at the intensity ranges used in laser fusion applications.

Intensity hot spots caused by filamentation of the laser can seriously degrade the laser-plasma coupling, and may affect the ablation pressure uniformity. The high intensity filaments can induce other harmful laser-plasma instabilities, such as stimulated Raman scattering or two plasmon decay.<sup>8</sup> Since filamentation has one of the lowest instability thresholds, and produces conditions favorable for other instabilities, it effectively lowers the thresholds and increases the growth rates of these other instabilities. These instabilities degrade the coupling quality by producing superthermal electrons which can preheat the fuel and spoil the gain. The enhancement of secondary instabilities also obscures our understanding of the underlying physics of the laser-plasma interaction: since filamentation is itself hard to measure directly, it is even more difficult to diagnose the effect of filamentation on other phenomena. There is also the concern that the laser filaments may produce ablation pressure nonuniformities which seed or drive the Rayleigh-Taylor instability in the imploding pellet.

To avoid the filamentation instability, as well as to provide some control over the gross laser beam profile, new optical smoothing techniques have been developed. One of these is the induced spatial incoherence (ISI) method; another is the random phase screen (RPS) method.<sup>10,11</sup> Experimental results using these techniques are incomplete and are still under investigation. The ISI results to date are favorable<sup>12</sup>; diagnostics of most laser-plasma instabilities (e.g.,  $2\omega_0$ ,  $3\omega_0$ , Raman scatter, SBS scatter) show significant reductions when compared to results with an unsmoothed beam. The RPS method has also shown some reduction in  $3\omega_0/2$  emission when used in a spherical illumination geometry.<sup>13</sup>

The implementation of each of these optical smoothing methods involves trade-offs. The RPS technique requires fast focusing optics to work effectively, but can be implemented with only minor modifications to existing lasers. ISI promises to be a more robust smoothing technique, but requires a broadband laser ( $\Delta\omega/\omega \sim 0.1\%$ ). Glass lasers can be converted to run broadband at  $1.06\mu\text{m}$  and  $0.53\mu\text{m}$  laser wavelengths; for short wavelengths, the KrF laser is an excellent candidate for ISI.<sup>14</sup>

Evaluation of these optical smoothing techniques requires information on how the filamentation instability is modified by the incident laser beam structure. Experimental data on filamentation has been sparse or nonexistent because of difficulties in controlling and diagnosing both the laser intensity structure and the plasma conditions, and theoretical techniques are insufficient to handle the complexity and nonlinearity inherent in the problem. Computational techniques are also severely tested, especially when modelling ISI or RPS. Both ISI and RPS require resolution of a large range of scalelengths (typically from less than one to a few hundred laser wavelengths). This requires large computational meshes, and the resolution constraints invalidate the use of well developed ray-tracing computational methods, which ignore diffractive effects that are important at the small scales.<sup>15</sup>

We will analyse the limitations of optical control techniques and compare these smoothing methods with traditional (unsmoothed) high-power lasers. The paper is organised as follows: in section II, we describe the construction of a two dimensional, time dependent, laser-plasma propagation code that includes both ponderomotive and thermal filamentation mechanisms. A steady state version of this code is also developed to treat problems without inherent time dependence. Next, a general analytic perturbation formalism of filamentation is presented in section III, and is extended to account for filamentation of incoherent ISI laser light. Finally, section IV presents the results of the numerical codes for a variety of laser beam profiles, and compares these results to the analytic predictions.

We will show that there is a qualitative difference between thermal and ponderomotive filamentation: filaments created by the thermal mechanism tend to bunch together and cause greater nonuniformity than ponderomotive filaments, which interact less. This clustering can result in a different saturation mechanism for thermal filamentation. We also find that the RPS optical smoothing method is dependent upon the use of fast optics ( $F/\# \lesssim 5$ ), and that the ISI method is capable of suppressing filamentation effects and providing smooth time-averaged intensity distributions using moderate laser bandwidth. In spite of the smoothing effects, ISI can also produce noticeably enhanced intensities in the plasma. In laboratory conditions, however, ISI is shown to suppress filamentation effects more completely than RPS or generic laser beams. At longer laser wavelengths filamentation occurs readily, and optical smoothing techniques suppress, but do not eliminate, the filamentation tendency. The best results for all optical methods are found with short-wavelength ( $\lambda_0 \sim 0.25\mu\text{m}$ ) laser-irradiated plasmas, where high absorption helps to reduce filamentation. In these plasmas, the ISI technique can completely eliminate filamentation.

## II. Governing Equations and Numerical Description.

In this section, we will develop the basis of the numerical scheme and discuss the relevant physics involved. We first derive the equations describing the laser light propagating in a plasma in which the dielectric constant has been perturbed; then we derive the equations describing the perturbation of the dielectric constant caused by changes in the plasma density responding to the laser light. We will treat two mechanisms responsible for plasma density changes. The first is the ponderomotive force, which directly expels the plasma from regions of high laser intensity. The second is thermal conduction dominated plasma heating, which creates temperature (and thus pressure) gradients and also forces the plasma out of high intensity regions.

The numerical algorithms that handle the governing equations will also be outlined in this section. Two versions of this code have been created. The first is time-dependent and is used primarily for the ISI calculations. The other model solves the equations in a quasi-steady state approximation, and is used to calculate filamentation effects when the incident light is stationary in time.

The analysis in this paper uses a two-dimensional (2D) cartesian description of the interaction. The spatial growth rates and amplification wavenumber-spectrum are very similar in two and three dimensions, as we will show in section III. The 2D numerical analysis also reduces computational memory and time constraints to manageable levels, and allows a large region of parameter space to be covered by using many simulations. Cartesian rather than cylindrical geometry is needed to study filamentation in 2D, since cylindrical geometry artificially favors on-axis focusing and cannot equitably treat the random-phasing required in optical smoothing simulations<sup>16,17</sup>. The main difference between the 2D calculations and three-dimensional (3D) calculations occurs in the peak intensity values: 3D filaments can typically reach much higher peak intensities. However, rapidly varying intensity profiles may restrain large peak intensities in 3D: preliminary results of 3D simulations of ISI show that the light energy distribution is comparable to 2D simulations.<sup>18</sup>

### A. Light Propagation

The laser propagation and filamentation will be described by the parabolic wave approximation to the Maxwell wave equation. Starting with the Maxwell equations, we assume that the divergence of the electric field is small ( $k_o \cdot \nabla \epsilon / \epsilon \ll k_o^2$ ), and set  $\nabla \cdot \mathbf{E} = 0$ . The electric field is separated into fast and slow space-time scales with the substitution:  $\mathbf{E}(x,z,t) = 1/2[\Psi(x,z,t)\exp\{-ik_o z + i\omega_o t\} + \text{c.c.}]$ .  $\Psi(x,z,t)$  is the wave envelope of the electric field,  $k_o(z)$  is the (real) laser wavenumber ( $k_o^2(z) = \omega^2 \epsilon_{or}(z)/c^2$ ),  $\epsilon_{or}$  is the real part of the unperturbed plasma dielectric constant ( $\epsilon_o = \epsilon_{or} + i\epsilon_{oi}$ ), and  $\epsilon_{or}(z) = 1 - n_e(z)/n_c$ , where  $n_e(z)$  is the unperturbed plasma electron density, and  $n_c$  is the plasma critical density. (The subscript 'o' appended to a variable means that it is evaluated at the background or unperturbed state.) If the wave envelope  $\Psi(x,z,t)$  varies slowly with respect to the laser wavelength and frequency, the Maxwell wave equation reduces to the parabolic wave equation:<sup>19</sup>

$$\{2ik_o \frac{\partial}{\partial z} - \nabla_\perp^2\} \Psi = \left[ \frac{\omega_o^2}{c^2} (\epsilon(z,x,t) - \epsilon_{or}(z)) - i \frac{\partial}{\partial z} k_o \right] \Psi \quad (2.1)$$

where  $\epsilon(z,x,t) = 1 - \omega_p^2(z,x,t)/\omega_o^2 - i\omega_p^2(z,x,t)\nu_{ei}(z,x,t)/\omega_o^3$  is the fully perturbed plasma dielectric constant;  $\omega_p = 4\pi e^2 n_e/m_e$  is the electron plasma frequency, and  $\nu_{ei}$  is the electron-ion collision frequency. (The time derivative ( $\partial \Psi / \partial t$ ) can be formally eliminated by transforming to the frame moving with the pulse group velocity<sup>20,21</sup>, with the variable substitution  $t' = t - s/v_g$ . In practice, one can simply ignore the time derivative term if the transit time of the propagation region is much smaller than any characteristic time for changes in the dielectric constant.) We normalize all spatial coordinates by the laser vacuum wavelength,  $\lambda_o$ , and define the transformation (using the spatially normalized coordinates):

$$\Psi = \Psi \exp\left\{\frac{1}{2} \int_0^z dz' \left[ k^{-1} (2\pi \epsilon_{oi}(z') - \partial k / \partial z') \right] \right\} \quad (2.2)$$

where  $k = k(z, z')$ ,  $\omega_o$ , and  $\epsilon_{oi} = -\omega_o^2(z) \nu_{ei}(z) / \omega_o^3$  is the imaginary part of the unperturbed plasma dielectric constant. This transformation accounts for ambient absorption and swelling due to intensity

inhomogeneity. Redefining the variable in the  $z$  direction as  $\eta = \int^z dz' / k(z')$ , we arrive at the parabolic wave equation in canonical form:

$$(4\pi i \frac{\partial}{\partial \eta} - \nabla_1^2) \psi = 4\pi^2 \delta\epsilon(\eta, x, t) \psi \quad (2.3)$$

where  $\delta\epsilon = \epsilon(\eta, x, t) - \epsilon(z)$  is the change in the plasma dielectric constant induced by the laser EM field. The effect of the plasma on the propagating field is concentrated in this term. For the cases of interest here, this induced change is entirely due to changes in the plasma density ( $\delta\epsilon = (n(z) - n(\eta, x, t)) / n_c$ ), and is found by solving the equations governing the plasma response to the laser.

The parabolic wave equation (2.3) is solved numerically on a mesh in  $x$ - $z$ ( $\eta$ ) space, with time treated as an independent parameter. The numerical algorithm consists of a split-step fast-Fourier-transform (FFT) technique<sup>22</sup>. To accommodate the Fourier transform technique, the computational mesh is periodic and equally spaced in the transverse ( $x$ ) direction.

The periodicity of the mesh affects the manner in which the initial laser field is numerically constructed. The focusing optics separate the incident laser beam into many individual beamlets, which are focused onto a target where they overlap one another. In the code, these overlapped beamlets are approximated as plane waves incident on the plasma at different angles; this is a good approximation in the center of the focal spot. For a high-power laser without optical smoothing, these beamlets correspond to light from different sections of the beam, and they will be slightly incoherent with respect to one another (depending upon the degree of aberration in the beam). In the case of the ISI and RPS smoothing techniques, these beamlets are incoherent with respect to one another, and correspond to the light coming from different echelon steps or phase shift regions of the random phase screen.

The incident wave field is constructed on the Fourier transformed plasma mesh which has the spacing  $\Delta k_x = 2\pi/X_{\max}$ , where  $X_{\max}$  is the length of the mesh in the  $x$  direction. Each beamlet has a unique wavenumber  $k$ : the wavenumber of the  $i$ -th plane-wave beamlet incident at angle  $\theta_i$  has a  $k_x$  component  $k_{xi} = k_0 \sin \theta_i$ . The angles  $\theta_i$  are given by the relation  $\theta_i = \tan^{-1}(d[i-(1+N_b)/2]/f)$ , where  $d$  is the width of the echelon step, phase shift area, or spatial coherence distance;  $f$  is the focal length of the lens, and  $i$  varies from 1 to  $N_b$  ( $N_b$  is the number of beamlets used). For moderate-to-large  $F/\#$  optics,  $\theta_{\max}$  is small and  $\tan \theta_i \approx \sin \theta_i \approx \theta_i$ . The modes corresponding to the individual beamlets are then assigned to the nearest point on the  $k$ -space transform mesh; the mesh spacing  $\Delta k_x = 2\pi/X_{\max}$  of the Fourier transformed mesh corresponds to an spatial angular resolution  $\Delta\theta = \lambda_0/X_{\max}$ . The real and imaginary parts of the electric field of each beamlet at wavenumber  $k_{xi}$  are then added to the value at the assigned mesh point. In general, the electric field at each  $k_x$  mesh point at  $z=0$  is independently assigned a random amplitude or phase (or both) depending upon the type of beam being simulated. For ISI simulations, the phases of each beamlet are chosen to be uniformly random and their amplitudes are selected with a Gaussian probability distribution. For RPS and other lasers, we typically use constant amplitude but uniformly random-phased modes. (More detail on the construction of laser profiles is given in section IV). The laser electric field  $E(x, z=0, t_0)$  is then found by inverse Fourier transforming this distribution. For the ISI simulation, this process is repeated again after every interval  $t_c$  to produce a new randomly generated  $E$  field.

### B. Plasma Response

The nonlinear change in the dielectric constant,  $\delta\epsilon(x, z, t, \psi)$ , is found by solving for the plasma density using a one-fluid plasma model. The calculation is greatly simplified by ignoring fluid coupling to itself along the direction of propagation of the laser ( $z$  axis). This approximation is valid when the plasma gradients along the  $z$ -axis are much smaller than gradients perpendicular to the  $z$ -axis, and is consistent with the slowly-varying-envelope approximation used previously for the laser electric field. The approximation also ignores fluid flow along the laser axis (which is typically supersonic in the underdense regions of laser-fusion plasmas<sup>23</sup>). The effect of flow on filamentation has been considered elsewhere<sup>24</sup> and can be ignored if the flow gradients are small and the fluid flow velocity is not too supersonic. The presence of counterpropagating axial supersonic flow reduces the amount of filamentation growth, so the results presented here may overestimate filamentation.

The continuity and momentum equations for the quasi-neutral one-fluid plasma in the presence of the laser ponderomotive force are linearized, and combined to give a driven ion-acoustic wave equation for the electron density<sup>20</sup>:

$$\left[ \frac{\partial^2}{\partial t^2} + \nu \frac{\partial}{\partial t} - C_s^2 V_\perp^2 \right] \ln(n_e) = V_\perp^2 C_s^2 + a V_\perp^2 \Psi \Psi^* \quad (2.4)$$

where  $a = Ze^2/4m_e m_i \omega_o^2$  and  $C_s^2 = (ZT_e + T_i)/m_i$ , and a phenomenological damping term  $\nu$  has been included. This equation describes the plasma responding as an ion-acoustic wave driven by temperature (pressure) gradients (first term on the right) and the ponderomotive force (second term). The variable  $\ln(n_e)$  preserves the correct nonlinear isothermal steady state behavior, and ensures positivity of the density in the transient regimes. The term  $\sim V_\perp \ln(n_e) V_\perp C_s^2$  is ignored, as it is second order in the perturbation. For all of the cases considered in this paper, the condition  $\delta n_e/n_{eo} \ll 1$  is valid; typical values of  $\delta n_e/n_{eo}$  in the time-dependent calculations are less than  $\sim 5\%$ . (For ISI laser light, hot-spots shift randomly on the order of the coherence time ( $\sim$ psec), which is faster than the density can respond. Intense ISI filaments are not precluded, though, since even shallow density channels can produce substantial refraction over long propagation distances. For long pulse non-ISI lasers, quasi-steady state density equilibration can occur, and a different, nonlinear steady-state formulation for the electron density is used. This algorithm will be described later.)

The ion temperature is assumed to be constant in time, since the ion-electron energy equilibration time is typically on the order of nanoseconds in these plasmas, and this is much longer than time-scales of interest. The background ion and electron temperatures are assumed to be equal. (The model and results are insensitive to the ratio of background electron-to-ion temperatures, and in any case the results can be easily renormalized to account for different ratios.) The perturbed electron temperature is then found by solving the relevant energy balance equation:

$$\frac{3}{2} n_e \frac{\partial}{\partial t} T_e = - V_\perp \cdot Q + S(n_e, T_e) \quad (2.5)$$

$Q$  is the electron thermal heat flux  $-\kappa_e V_\perp T_e$ ,  $S$  is the Joule heating source given by  $\kappa_b \Psi \Psi^*$ ,  $\kappa_e(T_e)$  is the electron thermal conductivity (including any flux-limiting effects), and  $\kappa_b(n_e, T_e)$  is the inverse bremsstrahlung absorption coefficient. Compression effects and electron-ion energy coupling are ignored since they are much smaller than the terms included in (2.5) for the cases studied here.

The equations (2.4) and (2.5) can be put into a form that depend on dimensionless quantities describing the magnitudes of relevant physical phenomena. We define:

$$\gamma_p \equiv \frac{\text{ponderomotive pressure}}{\text{plasma thermal pressure}}$$

$$\gamma_p = \frac{e^2 \Psi_o^* \Psi_o}{4m_e \omega_o^2 T_{eo} (1 + \frac{1}{Z})} = \frac{1}{4(1 + \frac{1}{Z})} \frac{V_o^2}{V_{Te}^2} \approx .00933 \frac{\lambda_o^2 [\mu\text{m}] I_o [10^{14} \frac{\text{W}}{\text{cm}^2}]}{\sqrt{\epsilon_o} (1 + \frac{1}{Z}) T_{eo} [\text{keV}]} \quad (2.6a)$$

$$\gamma_{T1} \equiv \frac{\text{thermal conduction transit time across laser wavelength dimensions}}{\text{ion-acoustic transit time across laser wavelength dimensions}}$$

$$\gamma_{T1} = \frac{3}{2} \frac{C_{so} n_{eo} c}{\kappa_{eo} \omega_o} \approx 1.35 \times 10^{-5} \frac{(n_{eo}/n_c) \ln \Lambda}{T_{eo}^2 [\text{keV}] \lambda_o [\mu\text{m}]} \frac{Z}{\varphi(Z)} \left( \frac{Z+1}{\Lambda} \right)^{1/2} \quad (2.6b)$$

$$\gamma_{T2} = \frac{\text{inverse bremmstrahlung heating rate}}{\text{thermal conduction cooling rate across laser wavelength dimensions}}$$

$$\gamma_{T2} = \frac{c^2 \kappa_b \psi^* \psi}{\omega_o^2 \kappa_{eo} T} \approx 8.95 \times 10^{-9} \frac{I_o [10^{14} \frac{W}{cm^2}]}{T_e^5 [keV] \sqrt{\epsilon_o}} \frac{Z^2 \ln \Lambda^2}{\phi(Z)} \left( \frac{n_{eo}}{n_c} \right)^2 \quad (2.6c)$$

where  $A$  and  $Z$  are the plasma ion mass and charge,  $\ln \Lambda$  is the Coulomb logarithm, and  $\phi(Z) \equiv (Z+24)/(1+24Z)$ .<sup>25</sup> The subscript 'o' again refers to evaluation of the variable at an unperturbed or initial value.

$\gamma_{T2}$  is the scaling constant of the steady-state temperature perturbation in the plasma, which is the active force in the thermal filamentation mechanism. The sensitive dependence upon plasma temperature is due to the temperature dependencies of the electron-ion collision frequency ( $\sim T_e^{-3/2}$ ) and electron thermal conductivity ( $\sim T_e^{5/2}$ ). As the temperature rises, both the decreasing collision frequency and increasing thermal conduction act together to smooth temperature gradients and quench the mechanism. For this reason thermal filamentation is more important in cooler dense plasmas, such as those created by short wavelength ( $\lambda_o < 0.5 \mu m$ ) irradiation. The ponderomotive force, on the other hand, is more important in long wavelength laser irradiation of plasmas ( $\gamma_p \sim I_o \lambda_o^2 / T_o$ ) because of its explicit dependency on laser wavelength.

Another important difference between these two types of filamentation is the mechanism by which they couple the laser light to the plasma. The ponderomotive force is almost instantaneously felt by the plasma (on times of order  $\omega_o^{-1}$ ), and is stronger for hot spots with shorter scalelengths. In contrast, the thermal forces in the plasma require the establishment of temperature gradients. The temperature distribution is created on a characteristic time scale that is longer for larger scalelengths ( $T \sim n_e L^2 / \kappa_e$ ), so the force is transmitted more slowly for large scale filaments. At shorter scalelengths, the force is suppressed by the diffusive thermal conduction smoothing. Thus, thermal forces are greatest at large scalelengths and long times, as opposed to ponderomotive forces which are greatest at short scalelengths at all times. These characteristics are the basis of the qualitative differences in the two filamentation mechanisms.

Using the quantities (2.6), the plasma response equations (2.4) and (2.5) can be re-written as:

$$\left[ \frac{\partial^2}{\partial t^2} + \frac{\nu \lambda}{C_s} \frac{\partial}{\partial t} - \nabla_1^2 \right] \ln(\bar{n}_e) = \frac{1}{(1+1/Z)} \nabla_1^2 \bar{T} + \gamma_p \nabla_1^2 \bar{I} \quad (2.7)$$

$$2\pi \gamma_{T1} \bar{n}_e \frac{\partial}{\partial t} \bar{T} = \nabla_1 \cdot \bar{\kappa}_e \bar{E}_1 \bar{T} + 4\pi^2 \gamma_{T2} \bar{I} \quad (2.8)$$

Again, the spatial coordinate  $x$  is normalized to the laser wavelength  $\lambda$ , and the time is normalized to  $\lambda/C_{so}$ , the ion-acoustic transit time across a laser wavelength. The overbar indicates that the variable is normalized with respect to its initial or unperturbed value, e.g.,  $\bar{n}_e = n_e(x, z, t)/n_{eo}(z)$  and  $\bar{I} = I(x, z, t)/I_o(z=0)$ .

In the computer code, the plasma variables  $n_e(x, z, t)$ ,  $\partial n_e(x, z, t)/\partial t$ , and  $T_e(x, z, t)$  are defined on the same  $\{x, z\}$  mesh as the laser electric field. The numerical algorithm for the hydrodynamics of eqn. (2.7) uses a combination of FFTs and an analytic solution. Assuming relatively small variations in the sound speed in  $x$ , the driven ion-acoustic wave equation can be Fourier transformed to yield:

$$\left[ \frac{\partial^2}{\partial t^2} + qk_x \frac{\partial}{\partial t} + k_x^2 \right] \ln(n_e) = -k_x^2 \left[ \gamma_p \bar{\psi}^* + \frac{1}{(1+1/Z)} \bar{T} \right] \quad (2.9)$$

where  $q$  is the ratio of the imaginary to real frequency of the ion acoustic wave,  $\propto k_x C_s$ . In the analysis presented here,  $q$  is generally taken to be  $1/2$ , in accordance with the significant Landau

damping for  $T_e \approx T_i$ ). For the purposes of the calculation, the driving terms are assumed to be approximately constant over the time step used in the code (on the order of a picosecond). The solution to (2.9) for a source that is constant from  $t_0$  to  $t_0 + \tau$  is then found analytically:

$$\ln(n[k_x, t_0 + \tau]) = e^{-k_x q \tau / 2} \left[ \left( \frac{\partial}{\partial t} \ln(n[t_0]) + \frac{k_x q}{2} [\ln(n[t_0]) + G] \right) \frac{\sin \kappa \tau}{\kappa} + [\ln(n[t_0]) + G] \cos \kappa \tau \right] - G \quad (2.10)$$

where  $\kappa = (1-q^2/4)^{1/2} k_x$  and  $G = \{\gamma_p \bar{\psi}^* \bar{\psi}(k', t' + \tau/2) + \bar{T}(k_x, t + \tau/2) / (1 + 1/Z)\}$ . This result is inverse Fourier transformed numerically to yield the plasma density at the advanced time  $t_0 + \tau$ .

The plasma energy balance eqn. (2.8) is solved with a three-point predictor-corrector method and is subject to the same periodic boundary conditions imposed by the Fourier treatment of the laser light and plasma density calculations. This can cause problems, since the net energy deposited by inverse bremsstrahlung at a given axial position cannot be lost either by heat flow out of the system or conversion to axial plasma kinetic energy. Under these circumstances, the plasma at any given axial position will continually gain energy (temperature) as the interaction progresses, in contrast to the real system which will reach a quasi-steady equilibrium with laser energy converted to plasma blowoff and target acceleration. To avoid this unphysical behavior, the spatially averaged energy gain  $(4\pi^2 \int dx' \gamma T_2(x', t') \bar{T}(x', t') / X_{\max})$  is subtracted from the source term of eqn. (2.8) to keep the mean temperature constant. This is equivalent to assuming that the energy losses (to axial conduction or flow) are independent of the coordinate  $x$ .

A harmonic-mean flux-limited formalism is used for the heat flux:

$$q = \left[ 1 + \frac{\kappa_e |\nabla_{\perp} T_e|}{f n T_e \nabla_{\perp} T} \right]^{-1} \kappa_{e \perp} \nabla_{\perp} T \quad (2.11)$$

$\kappa_e$  is the Spitzer electron thermal conduction coefficient of the plasma and  $f$  is a phenomenological flux-limiter. Anomalous flux limiting in laser plasmas has been implied by indirect experimental measurements of axial heat flow in the region between the critical density and the ablation surface. However, the magnitude of flux limiting in transverse heat transport in the underdense region is speculative at best. The semi-classical value  $f=0.1$  is used here simply to ensure that the heat flux stays within physically allowed bounds<sup>26</sup>. In most of the calculations presented here (and in all of the ISI calculations) the heat flux is much smaller than this limit, so the results are insensitive to the flux-limiter.

For time independent problems (i.e., laser-plasma interactions with non-ISI lasers and pulse lengths long compared to hydro times), the calculation of the plasma density is simplified. The solution of the steady-state momentum balance equation for time-independent sources  $\psi^* \psi(x, z)$  and  $T_e(x, t)$  is

$$n_e(x, z) = \frac{C'(z)}{C_s^2(x, z)} \exp(-\gamma_p \int_x^X dx'' C_s^{-2}(x'', t) \nabla_{x''} \bar{\psi}^* \bar{\psi}(x'', z)) , \quad (2.12)$$

where  $C'$  is a constant of integration given by the definition of average density:  $C' = n_{\max} X_{\max} / \int dx'' C_s^{-2}(x'') \exp(-\gamma_p \int dx'' C_s^{-2} \nabla_{x''} \bar{\psi}^* \bar{\psi})$ . The temperature  $T_e(x, z)$  is found by iterative solution of eqn. (2.8) with arbitrary time steps, performed until the solution converges. These separate solutions for  $T_e(x, z)$  and  $n_e(x, z)$  are then iterated alternately to obtain a convergent steady-state solution for both.

### III. Analytic Formulation of Filamentation

Before proceeding with the computational analysis of filamentation, we present an analytic treatment of filamentation that is based upon the perturbation solution of the complete Maxwell's wave equation. The formalism is developed in general terms, then applied to the ponderomotive and thermal filamentation mechanisms separately. The general formalism is also heuristically extended to include spatially and temporally incoherent ISI light. Results for both ponderomotive and thermal filamentation of ISI light are also presented. In section IV, we will then compare results of the computational and analytic treatments of filamentation.

#### A. Basic theory of Filamentation

The formalism used here to describe the scaling of thresholds and growth rates of filamentation is well established<sup>27,25</sup>. Perturbations of plane waves in homogeneous plasmas are analyzed using the exact Maxwell's wave equation for the electric field and an expansion of the dielectric constant in terms of the perturbed laser intensity,  $\epsilon(<\underline{E}+\delta\underline{E}>^2) \approx \epsilon + \epsilon' \underline{E} \cdot \delta\underline{E}$ . Choosing  $\underline{E} = E_x^0 \exp[i(w_o t - k_o z)]$ , and assuming the perturbed field  $\delta\underline{E}$  has the form  $\delta\underline{E} \exp[i(w_o t - k_o z) + k_g z + i(k_x x + k_y y)]$  where  $k_g^2 \ll k_x^2 + k_y^2$ , one finds a general dispersion relation for both ponderomotive and thermal mechanisms:

$$(k_x^2 + k_y^2) \left[ \frac{2\delta\epsilon}{\epsilon_0} (k_o^2 - k_x^2) - (k_x^2 + k_y^2) \right] = 4k_o^2 k_g^2 \quad (3.1)$$

where  $\delta\epsilon = \partial\epsilon(k_x, k_y, I_o + \delta I)/\partial(\delta I/I_o)$ ;  $\delta\epsilon = (n/n_c)\gamma_p$  for the ponderomotive mechanism and  $\delta\epsilon = (n/n_c)\gamma_{T2}/[k_x^2 + k_y^2]$  for the thermal mechanism. (For notational convenience, we define  $k$  as a wavenumber normalized by the laser vacuum wavenumber; i.e.,  $k_\perp = k_\perp c/w_o$ ). We have assumed  $\delta\underline{E}$  parallel to  $\underline{E}$ , as this is the fastest growing configuration. For the one dimensional case we let  $k_y = 0$ ,  $k_x = k_\perp$ , and assume that the two dimensional case is confined to  $k_x = k_y = k_\perp/\sqrt{2}$ ; then the general expression for the instability threshold in  $N$  transverse dimensions (where  $N=1$  or 2) is:

$$k_\perp^2 \leq \left[ \frac{1}{2\delta\epsilon} + \frac{1}{N\epsilon_0} \right]^{-1} \quad (3.2)$$

For any interaction strength ( $\delta\epsilon$ ), there will be some range of unstable perturbation wavelengths of the incident light intensity. There remains the questions as to whether this range is relevant (contained in the interaction region), and if so, whether the perturbations have room to grow within the propagation region. The spatial growth rate has a maximum at a value  $k_\perp^{\max}$  determined by the a root of the equation:

$$(1 + \frac{2}{N} \frac{\delta\epsilon}{\epsilon_0}) [k_\perp^{\max}]^4 - \left\{ \frac{1}{N} \frac{\delta\epsilon'}{\epsilon_0} + \epsilon_0 \delta\epsilon \right\} [k_\perp^{\max}]^2 + \delta\epsilon' = 0 \quad (3.3)$$

where  $\delta\epsilon'$  is differentiation of  $\delta\epsilon$  with respect to  $(k_\perp)^2$ . For the ponderomotive mechanism  $\delta\epsilon' = 0$ , and for the thermal mechanism  $\delta\epsilon' = (n/n_c)\gamma_{T2}$ . Using these relations in (3.3) yields the fastest growing modes and their associated growth rates for the thermal and ponderomotive cases. The results are shown in Table I; they will be compared to numerical solutions later.

Although the fastest growing thermal mode has an infinite wavelength, the growth rate is approximately constant for  $k_\perp \ll 1$ , which is generally the region of interest. Thus, for thermal filamentation, most modes grow at the same rate. In contrast, the ponderomotive growth rate is  $\sim k_\perp$  for small  $k_\perp$ . If the ponderomotive force is strong enough, there is some value of  $k_\perp$  at which the ponderomotive and thermal growth rates are equal. This point occurs for filaments of size  $\lambda_\perp/\lambda_o = (\gamma_p/\gamma_{T2})^{1/2}$ . Ponderomotive filamentation is dominant for filaments smaller than this size, while thermal filamentation is more important for the larger filaments. This suggests a scenario whereby the thermal and ponderomotive mechanisms can couple: large wavelength modes can begin to focus to due thermal filamentation, then become dominated by ponderomotive filamentation when the filament becomes small enough.

### B. ISI and filamentation.

The ISI optical smoothing technique leads to rapid, random fluctuations in the laser intensity. If we average these fluctuations over a time  $t_{avg}$ , then the fluctuations compared to the mean are proportional to  $(t_c/t_{avg})^{1/2}$ , where  $t_c$  is the coherence time of the laser.<sup>9</sup> Since the characteristic plasma hydrodynamic response time is much longer than the typical laser coherence time, the plasma dielectric constant will respond to the time-averaged intensity. As a simple way to account for this, we will substitute this time-averaged intensity perturbation  $(I_o(t_c/t_{avg})^{1/2})$  for the background intensity ( $I_o$ ) in the formulas for the dielectric response, using a suitable value for  $t_{avg}$ . After this substitution, the filamentation formulas given in the last section will be re-derived.

This analysis ignores some effects which may contribute to the suppression or enhancement of filamentation. For instance, the stochastic-like fluctuations in the density will increase the light scattering and counteract filamentation.<sup>28</sup> On the other hand, the time average of the intensity fluctuation is treated linearly, although the interaction is itself nonlinear; this underestimates the filamentation. It is implicitly assumed that corrections due to these effects are small.

The averaging time  $t_{avg}$  is taken to be the characteristic time for the filamentation mechanism to change the dielectric constant appreciably over the transverse dimensions of the filament,  $\lambda_1$ . For the ponderomotive mechanism this averaging time is the ion-acoustic transit time of the filament,  $\lambda_1/C_s$ . For the thermal mechanism, the averaging time is the larger of the ion-acoustic transit time and the thermal conduction transit time,  $n_e \lambda_1^2/\kappa_e$ . The ion-acoustic transit time is larger when the ratio  $\gamma_{T1} \lambda_1/\lambda_o$  (see eqn [2.6b]) is less than one. This ratio is largest for cooler, short wavelength plasmas ( $\gamma_{T1} \sim 1/[T_e^2 \lambda_o]$ ) and large filaments. In a worst case ( $\lambda_o = 0.25 \mu\text{m}$  in a CH plasma with  $T_e = 1\text{keV}$ ,  $n/n_c = 0.25$ ) the ion-acoustic time is the dominant averaging time for  $\lambda_1 \lesssim 350 \mu\text{m}$ . Since this worst-case value of  $350 \mu\text{m}$  is larger than almost all filaments studied here, we will use the acoustic transit time as the averaging time for both thermal and ponderomotive filamentation.

The filamentation analysis presented in section III.A is now repeated, except that the background dielectric constant depends upon the time averaged intensity perturbation level, instead of the plane wave intensity. Thus, we substitute  $I_o(t_c/t_{avg})^{1/2}$  (with  $t_{avg} = \lambda_1/C_s$ ), for  $I_o$  in the expressions for the dielectric change,  $\delta\epsilon$ , given in section III.A. For the ponderomotive mechanism this substitution gives:

$$\delta\epsilon_p = \frac{n}{n_c} \gamma_p \tau_c^{1/2} [\tilde{k}_1]^{1/2}$$

and:

$$\delta\epsilon'_p = -\frac{1}{4} \frac{n}{n_c} \gamma_p \tau_c^{1/2} [\tilde{k}_1]^{5/2},$$

where we have defined a normalized coherence time as:

$$\tau_c = \frac{t_c C_s}{\lambda_o} \approx .31 \left[ \frac{(1+1/Z)}{A} T_e (\text{keV}) \right]^{1/2} \frac{t_c (\text{psec})}{\lambda_o (\mu\text{m})}.$$

For the thermal mechanism,

$$\delta\epsilon_t \approx \frac{n}{n_c} \gamma_{T2} \tau_c^{1/2} [\tilde{k}_1]^{-3/2}$$

and

$$\delta\epsilon_t' = \frac{3}{4} \frac{n}{n_c} \gamma_{T2} \tau_c^{1/2} [\bar{k}_1]^{1/2} .$$

Using these equations in eqns (3.1)-(3.3) gives the relations for ISI filamentation found in Table II. These results will be compared to results of the numerical simulations in the next section.

#### IV. Analysis and Discussion

In this section, we use the code described in section II to simulate filamentation behavior of different laser beam profiles. We proceed in a carefully structured manner, beginning with simple, well-characterized problems having known solutions. Complexity is added to the interaction a step at a time, gradually building up to simulations of realistic laser beams propagating in laboratory-type laser-plasmas. As we proceed, unique characteristics of the newly added features are identified and discussed. The analytic results of section III are also compared to these simulations, and the limitations of the analysis are addressed.

We begin with the simplest case of filamentation: the propagation of a Gaussian laser beam in a homogeneous, nonabsorbing, medium. Analytic solutions of this model for ponderomotive and thermal filamentation are developed in the appendix, and are compared to the numerical solutions. This comparison exposes the limitations of analytic methods for even the simplest cases of filamentation, and illustrates the physics that distinguishes the two types of filamentation. Next, the beam profile made more complex while the plasma remains simple: we consider generic and optically smoothed RPS and ISI laser beams. These more realistic beams are composed of randomly phased perturbations of different wavelengths, and introduce the possibility of nonlinear mode coupling. Finally, we add inhomogeneity and absorption to the plasma model, and consider laboratory plasmas relevant to ICF experiments.

Throughout this analysis, we will use two basic parameters to measure filamentation effects: the filament focal length and the focal intensity maximum. These quantities are useful filamentation measures for two reasons: first, these parameters can be directly compared to the analytic theory. Secondly, the focal length gives the minimum size of a plasma in which filamentation effects may be observed, while the maximum intensity quantifies the impact of filamentation on other nonlinear processes.

The filament focal length and intensity maximum are not easily defined except in the simplest of cases. In these simple cases, the propagation of a single-peaked incident intensity profile, the first intensity maximum in the propagation direction corresponds to the focus of the filament. In more complex beam profiles, however, there may be (and usually are) many intensity maxima along the propagation distance, of varying degrees of magnitude. The usual practice here is to identify the focus at the first intensity maximum encountered along the propagation direction; further, it is supposed that this first maximum is due to focusing of the fastest growing mode. In some cases, however, intensity maximums further along in the propagation may be considerably more intense than the first. In this case, more than one focal length or intensity maximum can be defined.

In the following discussion, we make the following definitions for notational convenience: the maximum value of a distribution  $I(x,z,t)$  over all values of the variable  $x$  is denoted as  $\text{MAX}\{I\}_x$ , while the first maximum of the distribution in the direction of the variable  $z$  (i.e., where  $dI/dz=0$  and  $d^2I/dz^2 < 0$  for the smallest value of  $z$ ) is denoted  $\text{MAX}_1\{I\}_z$ . Also, the filamentation focal length is sometimes abbreviated as  $l_f$ .

##### A. Filamentation in Homogeneous, Nonabsorbing Plasmas: Gaussian filaments

The accuracy of theoretical approximations and predictions is evaluated using the laser-plasma propagation code previously described. For the purposes of the calculation and comparison, we begin by using a nonabsorbing and homogeneous plasma. Nonabsorbing means that the laser energy is not depleted as it propagates through the plasma; however, the laser is allowed to heat the plasma to produce the thermal and pressure gradients needed for thermal filamentation. Homogeneity refers only to the background plasma; again, the laser is allowed to produce the inhomogeneity needed for filamentation. Although unrealistic in some ways, this plasma model provides a good test-bed for basic filamentation phenomena; it shows the qualitative filamentation behavior, and allows us to compare the calculations to the non-absorbing, homogenous plasma theory of section III. The first order effects of absorption and inhomogeneity only alter the quantitative behavior of filamentation. Absorption counteracts filamentation to first order by decreasing the growth rate by the amount  $-\kappa$ ; inhomogeneity, on the other hand, causes local variations in the strength of the focusing forces. Inclusion of these factors is considered in section IV.B, which addresses laboratory plasmas.

We begin by considering the focusing of a Gaussian filament in the steady state limit. The numerical results can then be compared directly to approximate solutions of the steady-state nonlinear propagation equation (2.3). The derivation and results of this Gaussian model for the ponderomotive and thermal mechanisms are given in the appendix to this paper: the scaling and magnitude of the

focal lengths found there are the same or similar to the results given in Table I. The Gaussian model also predicts peak intensities reached during self-focusing. We compare the calculations to the results of this model for the cases of ponderomotive and thermal filamentation separately.

As a first example, we calculate the intensity as a function of the distance of propagation into the plasma for a case where only the ponderomotive force is active (fig. 1). The initial radius of the filament is  $a_0 = 20\lambda_0$  and the interaction strength is  $\gamma_p = 5 \times 10^{-3}$  (this is 40 times the threshold value). The model and calculation results are comparable: the focal length ( $350\lambda_0$ ) lies within  $\sim 10\%$  of the predicted result ( $315\lambda_0$ ), implying that the Gaussian model is fairly accurate in determining focal lengths; this agrees with previous findings.<sup>3,29</sup> However, the predicted focal intensity is much larger than we find with the code. In part this is due to the sensitivity of the model's peak intensity to the focal spot radius: small changes in the radius give rise to large changes in the peak intensity when the focal spot radius is small ( $\text{MAX}\{I\}_x \sim 1/\text{width}$ ). In reality, the filament is not constrained to stay Gaussian, and the peak intensity is not so sensitive to the filament radius. (The inability of the Gaussian model to account for saturation effects in the dielectric response is not important here, as the maximum dielectric change in the simulation is  $\lesssim 0.5\%$ ).

After the first focus, the filament usually behaves quite differently from the model; propagation can be periodic, although it usually has a more complex periodicity than predicted. The behavior appears to depend on the power level of the filament. Looking at the long distance behavior of the simulation just described (fig. 2b, 40X threshold power), we observe the beam breaking up into two off-axis filaments which focus twice independently, and then combining again to form a single filament. The behavior is repeated again, but each time the central single filament is degraded in power; the periodicity is only approximate since the original Gaussian is not reproduced. At higher powers (fig. 2c, 450X threshold), the beam breaks into many filaments, which spray outward from the region of the first focus; in contrast a lower power example (fig. 2a, 10X threshold) exhibits the simple oscillation predicted by the model, although the oscillation is slowly damped by light escaping the filament. In general, the number of filaments formed after the first focus is an increasing function of the incident beam power.<sup>18</sup>

The scaling behavior of the spatial growth rate compares favorably with the model. Fig. 3a plots the focal distance as a function of  $\gamma_p$  for ponderomotively focused Gaussian filaments with initial 1/e radius  $a_0 = 40\lambda_0$ . (The focal distance is defined as the distance from the beginning of the propagation in the plasma to the point where the intensity reaches its first maximum.) A linear least-squares fit through the data points yields the empirical dependence  $l_f/a_0 \approx \gamma_p^{-0.8}$ , which is comparable to the predicted dependence  $l_f/a_0 \approx \gamma_p^{-0.5}$  (from the appendix and table I). Calculations performed for filaments with a Gaussian 1/e intensity radius  $a_0 = 20\lambda_0$  also exhibit this scaling.

The peak focal intensities are very weakly dependent upon  $\gamma_p a_0^2/\lambda_0^2$ , the theoretical controlling parameter, and are much smaller than predicted (fig. 3b). Again, the approximation  $\epsilon(E) \approx \epsilon + \epsilon'E$  in the model is not violated even for the largest values of  $\gamma_p a_0^2/\lambda_0^2$ . This indicates that deviations from the Gaussian constant-shape ansatz are the failure mode in the model. The deviations occur because the expansion  $\epsilon(x) \approx \epsilon(x=0) + .5\epsilon_{xx} x^2$  used in the Gaussian model is substantially violated in the simulation.

These calculations were repeated using only the thermal filamentation mechanism; the results are shown in fig. 4. The initial filament radius is again  $a_0 = 40\lambda_0$ , and the interaction strength parameter varies from  $\gamma_{T2} \approx 5 \times 10^{-8}$  to  $5 \times 10^{-5}$ . The behavior here is not as simple as in the ponderomotive case. At low powers the focal length varies as  $\sim \gamma^{-0.49}$ , matching quite closely the scaling of the predicted values, although the magnitude of the focal length is consistently  $\sim 20\%$  larger than the predicted value. Also, the maximum intensities are 50%-65% lower than predicted, though they show the correct scaling with the filament intensity.

Contrary to expectation, as the interaction strength increases to high values ( $\gamma_{T2} \approx 4 \times 10^{-8}$ ), the focal length increases and the focal intensity decreases. Closer examination of the simulation reveals the cause of this curious behavior: at high intensities, the temperature profile becomes flat-topped and sharp-sided (fig. 5). The electron thermal conductivity is a strong power of the temperature, so the hot region (high conductivity) is smooth, and the cold region (low conductivity) has steep temperature gradients. The density profile is shaped like the temperature profile ( $\delta n_e \sim \delta T_e^2$ ), so the filament refract primarily at the edges. The light refracted at this sharp edge is refracted into large angles, and the resulting interference of this light with the main body of the filament creates high frequency intensity structure. This structure increases the net diffractive force of the filament and

counteracts the focusing tendency of the density channel; thus the focusing is reduced. The deliberate creation of high frequency structure on the incident light has been suggested as a filamentation suppression mechanism<sup>30</sup>, and is also the basis of the RPS illumination technique. Here, however, the structure is created by the laser-plasma interaction itself.

The sharp-sided, flat-topped temperature profiles are dependent on the boundary conditions of the code. The largest wavelength temperature perturbation is limited to the size of the numerical mesh, which is only a few times larger than the filament. Normally, this is of little consequence: if there is moderate heating, the conductivity is approximately constant and the Fourier spectra of the temperature has the same spectral range as the source. When the heating is strong however, significant energy is transferred into both longer and shorter wavelength modes due to the nonlinearities in the electron thermal conductivity and collision frequency. This energy cannot be put into modes larger than the mesh size, so it is forced into the numerically resolvable spectrum, in modes with shorter wavelengths. These amplified short wavelength modes can then be further enhanced by the temperature steepening associated with the nonlinear conductivity. Although these particular results presented here are due in some part to the computational constraints, the profile steepening effect is a well-known phenomenon<sup>31</sup> in nonlinear heat transport. The defocusing effect for strong thermal filamentation exists, but the quantitative threshold calculated here is dependent on the actual boundary conditions of the system, and is not universal. As the size of the system increases (relative to the heated region), the defocusing threshold will tend to increase.

The results of Gaussian beam filamentation show the limitations of the analysis for ideal filaments in simple plasmas. Ponderomotive filamentation focal length scaling with intensity agrees well with theory, but the predictions of the peak focal intensity are very inaccurate. In addition, the propagation behavior is different than predicted; as the interaction gets stronger, more filaments are formed as the beam breaks up after the first focus. Calculations and predictions of thermal filamentation agree fairly well in scaling and magnitude, but only at lower powers. At higher powers, nonlinear temperature variations cause focusing effects to weaken. Aware of these constraints and behaviors, we are prepared to examine filamentation occurring with more complex laser illumination profiles.

#### B. Filamentation in Homogeneous, Nonabsorbing Plasmas: Complex Laser Beams.

In this section we investigate the behavior of realistic illumination profiles in simple plasmas. Three different laser beam types are considered here: the typical or generic laser beam, the RPS laser beam, and the ISI laser beam. In part (i), these profiles are defined and their characteristic features are discussed. Then, in parts (ii) through (iv), each profile is considered in turn, with the results of the filamentation simulations presented. The qualitative features of these simulations are discussed and the quantitative results are compared to theory.

##### i. Definition and Construction of Complex Laser Beams.

We will first consider a "generic" laser intensity profile, representing a typical, high-power laser beam. These profiles are determined by many installation-dependent (and time-dependent) parameters. Imperfections of the optical system design or components, optical misalignment, or temperature fluctuations present in the optical components during a specific shot, can cause unique aberrations in the output beam. In gain-saturated lasers, the aberration structure is preferentially in the phase of the laser electric field. Further aggravating the problem, the desired focal spot size for large scale-length laser-plasma interactions is much larger than the diffraction-limited spot size, and quasi-near field intensity distributions must be used. In the quasi-near field, even small amounts of aberration show up as significant structure in the intensity profile. Laser intensity profiles are sometimes characterized by their peak-to-valley intensity ratio; 3:1 to 10:1 are not uncommon values for this parameter.

In this study, a variety of generic laser profiles with different root-mean-square standard deviations are used ( $\sigma_{rms}^2 \equiv \int dx (I(x) - I_{avg})^2 / \int I(x)^2 dx$ ). The peak-to-average intensity difference is  $\sim 4$  times the value of  $\sigma_{rms}$ , so typical values of  $\sigma_{rms}$  are in the range of 0.25 to 1.0;  $\sigma_{rms} = 0.5$  is often used as the representative value. In the code, these profiles are constructed by adding randomly phased electric field fluctuations onto a DC ( $k_x = 0$ ) electric field term. Electric field fluctuations of all wavelengths (excepting the DC term) have the same amplitude, and span the wavenumber spectrum (from  $|k_x| = 1/X_{max}$  to  $1/2F$ , in increments of  $1/X_{max}$ ; recall that all spatial dimensions are scaled to  $\lambda$ ). Varying the  $k_x \neq 0$  amplitude relative to the DC amplitude gives different values of  $\sigma_{rms}$ . This construction gives two different characteristic amplitudes for the

Fourier intensity spectrum (fig. 6a). If the magnitude of the DC electric field term is  $A_0$ , and the magnitude of the finite wavenumber  $E$  field variations is  $a_1$ , then the intensity profile has Fourier amplitudes that are of order  $\sim 2A_0 a_1^2 + a_1^2$  and  $a_1^2$ , for the wavenumber ranges  $|k_1| = \{1/X_{\max}:1/2F\}$  and  $|k_1| = \{1/2F:1/F\}$  respectively. (The notation  $\{a:b\}$  denotes the range of values from  $a$  to  $b$ .) For small values of  $\sigma_{\text{rms}}$ ,  $a_1 \ll A_0$ , and the larger wavenumber range is of considerably smaller amplitude than the shorter wavenumber range. (In fig. 6a, with  $F/20$  optics and a plasma mesh length  $400\text{ }\mu\text{m}$  wide, these wavenumber ranges correspond to  $|k_1| = \{0.0025:0.025\}$  and  $|k_1| = \{0.025:0.05\}$ , respectively.)

Next we consider the random-phase-screen (RPS) illumination smoothing method. This is a potentially attractive near-term method for beam control, since it can be used on existing laser beams. The laser beam is passed through a simple random phase mask before it is focused down on the target. This phase mask consists of a large number of discrete areas which randomly apply a phase shift between 0 and  $2\pi$  radians to the section of beam passing through it. (This is slightly different than the current experimental version of RPS, where the randomly applied phase shifts are either 0 or  $\pi$ .<sup>10,11</sup>) At the lens focal plane, this produces a high frequency, spatially incoherent pattern with a smooth envelope determined by the diffraction pattern of the individual phase-shifting areas. This is similar to the ISI method, but without the laser bandwidth: the structure in the RPS method is stationary in time. In principle, if the spatial structure has a high maximum wavenumber  $k_1^{\max}$ , the filamentation growth rate will be suppressed (similar to the situation observed in section IV.A with thermal filamentation). This principle can be quantified using the relations in table I; filamentation is stabilized when  $k_1^2 (2n_e \gamma_p / n_c)^{1/2}$  (ponderomotive) or  $k_1^2 (2n_e \gamma_{T_2} / n_c)^{1/4}$  (thermal). When there is appreciable energy in the high wavenumber modes, they diffract substantially over distances smaller than the growth lengths of the unstable modes. If this small-scale diffraction causes significant changes to the structure or phase of the larger unstable modes, filamentation may be suppressed. Also, the presence of appreciable energy in these modes implies that there is less power in the unstable modes, which contributes to stabilization.

The RPS technique generates an intensity profile that contains both larger amplitude and higher wavenumber components than the generic profile. A typical profile (fig. 6) has higher peak intensities and higher spatial frequencies than a corresponding generic profile. The wavenumber spectrum of the RPS beam is controlled mainly by the  $F$  number of the lens: the highest wavenumber component of the incident electric field has a wavenumber  $k_1 \sim 1/2F$ . The DC ( $k_1=0$ ) electric field term is of the same order as the finite wavenumber ( $k_1 \neq 0$ ) electric field amplitudes, so the high and low wavenumber intensity ranges ( $|k_1| = \{1/X_{\max}:1/2F\}$  and  $|k_1| = \{1/2F:1/F\}$ , respectively) will have amplitudes of the same order. Since RPS requires fast optics (small  $F/\#$ ), the largest wavenumber in these profiles is usually much larger than in the corresponding generic profile. One of the purposes here is to bracket the acceptable  $F/\#$  range for the RPS method.

Finally, we also simulate the induced-spatial-incoherence optical smoothing method. ISI in its simplest form is produced by passing a broad-band laser beam through an echelon, or stepped transmitting plate. Each echelon step, like the random-phase-screen, produces a phase shift by imposing a time delay on the beam passing through. Unlike the RPS technique, the time delay of each echelon step relative to any other step is longer than the laser coherence time, so that the spatially incoherent structure produced at the focus completely changes on the time scale of the laser coherence time. Since the coherence time ( $\sim 1\text{ psec}$ ) can be made much shorter than gross plasma hydrodynamic response times ( $\sim 100\text{ ps}$ ), the plasma should respond hydrodynamically only to the time average of the laser profile, which asymptotically approaches a smooth envelope function.

Of these three laser profile types, only ISI is inherently a time-dependent profile. For the generic and RPS cases, the intensity profile is frozen in, and the plasma can reach a quasi-steady equilibrium if the laser pulse is long enough (multi-nanoseconds). We have performed time-dependent simulations using these stationary laser profiles, and they show close agreement with the steady state simulations after times on the order of a few  $\lambda_1/C_s$ . (In other specific cases, it has been shown that steady state laser profiles can result in inherently time-dependent behavior<sup>32</sup>. In our formalism, the neglect of axial density coupling in eqns. (2.7) and (2.9) has ruled out the possibility of this type of nonstationary behavior, so the issue is not addressed here. However, it deserves closer investigation in the future.)

## ii. Filamentation of Generic Laser Beams

We now consider the behavior of the generic laser beam in the homogeneous, nonabsorbing plasma where only the ponderomotive force is operative. Fig. 7 shows a typical result ( $\gamma_p = 1.3 \times 10^{-3}$ ,  $\sigma_{rms} = .5$ , and F/10 optics): in general, the hot spots behave like individual noninteracting filaments similar to the Gaussian filament shown earlier. Interaction between filaments tends to occur only if two hot spots happen to be initially close (distances on the order of their own diameter), or on an initially intersecting path.

The behavior of the individual Fourier modes in this simulation can be compared directly to perturbation theory. One might expect the comparison to be adequate up to the point where the mode coupling is appreciable. Fig. 8 shows the low order Fourier mode amplitudes of the intensity distribution, and compares them to the results found by applying the factor  $\exp(k_1(k_1)L)$  (from table I) to the incident intensity distribution. In theory, the most unstable mode is at  $k_1 = 0.025$  ( $\lambda_1 = 40\lambda_0$ ); in the simulation this mode closely follows the predicted growth for  $z \leq 400\lambda_0$ , after which it levels off and then decreases. Other theoretically unstable modes grow at rates different (and generally less) than predicted. For  $k_1 \geq 0.04$ , the modes are supposedly stable, yet significant energy appears to be going into these modes after propagation distances of  $100-200\lambda_0$ . This shift of energy from small  $k_1$  to large  $k_1$  is expected for filaments that focus and contract in size.

Although the individual modes do not behave as predicted due to mode coupling effects, the focal length predictions are fairly accurate. Fig. 9 shows the variation of focal length and focal intensity with  $\gamma_p$  for simulations with F/20 and F/10 optics and  $\sigma_{rms} = 0.5$  on a  $400\lambda_0$  wide mesh; the focus is defined at the point  $\text{MAX}_1(\text{MAX}\{I\}_{xz})$ . There is close agreement between the focal length prediction and simulation: the simulation results lie very near to the predicted values (from table I) shown by the dotted line. (This is partially fortuitous, since the formulas in table I are independent of  $\sigma_{rms}$ . Although different values of  $\sigma_{rms}$  result in different focal lengths (e.g., smaller  $\sigma_{rms}$  gives larger  $l_f$ ), the scaling of  $l_f$  with  $\gamma_p$  is similar.) For smaller values of  $\gamma_p$ ,  $l_f \sim \gamma_p^{-1}$  (table I) since the fastest growing mode is represented in the incident intensity profile ( $k_1^{\text{max}} \leq 1/F$ ). For  $\gamma_p > 0.005$ , however, the fastest growing mode is limited by the smallest perturbation wavelength in the incident spectrum:  $\lambda_1 = 20\lambda_0$ . In this range of  $\gamma_p$ , the fastest growing mode is constant and the focal length scales as  $l_f \sim \gamma_p^{-0.50}$  (table I). In contrast to the focal length predictions, the intensity maximum predictions are very inaccurate. Two regimes appear to have been reversed between theory and simulation: at small  $\gamma_p$ , we expect  $\text{MAX}\{I\}_{xz} \sim \text{constant}$  (since  $I_{\text{max}} = \gamma_p k_1^{-2}$  [see appendix], and  $k_1^{\text{max}} \sim \gamma_p^{1/2}$  [table II]), and instead we observe a rapidly increasing  $\text{MAX}\{I\}_{xz}$ . For  $\gamma_p > 0.005$  we expect  $\text{MAX}\{I\}_{xz} \sim \gamma_p^{-1}$  (table I, using  $k_1^{\text{max}} \sim \text{constant}$ ), and we observe a constant or slightly declining value of  $\text{MAX}\{I\}_{xz}$  with increasing  $\gamma_p$ .

In summary, the focal length predictions seem to apply better than expected for ponderomotive filamentation of generic laser profiles composed of many modes. In contrast, the predictions of intensity maxima are quite inaccurate in the same situation. The same tendencies were noted with the Gaussian beam simulations (see fig. 3).

With the thermal filamentation mechanism acting alone on the generic laser profiles, we observe a qualitatively different behavior: the filaments tend to attract one another over distances much greater than their own dimensions (fig. 10:  $\gamma_{T2} = 1.2 \times 10^{-8}$ , F/20, and  $\sigma_{rms} = 0.5$ ). The diffusive electron thermal conduction produces temperature and density structures much larger than the hot spots; the result is the development of large wavelength intensity modes, composed of many smaller scale filaments. This large scale "supermode" undergoes large scale periodic focusing and defocusing when propagating over large distances. Since the most unstable mode is at  $k_1 = 0$ , and the growth length decreases monotonically as  $k_1 \rightarrow 0$ , the dimension of this supermode is limited only by the size of the physical system. The gross illumination symmetry can be affected by this filament clustering behavior.

The applicability of the perturbation analysis to these type of profiles is assessed by examining a Fourier decomposition of the intensity profile (fig. 11). Simulation and theory agree that the fastest growing mode is the smallest wavenumber ( $k_1 = 0.0025$ ) of the system. The periodicity evident in the lowest order mode matches up with the gross periodicity of the distribution as seen in fig. 10. The theoretical period of this mode is  $\sim 580\lambda_0$ , about 1/3 of the measured periodicity of  $1500\lambda_0$ . The growth rates for other modes in the simulation also tend to be smaller than predicted, and mode coupling effects are evident after propagation distances of a few hundred  $\lambda_0$  into the plasma.

The observed filamentation parameters for thermal filamentation of generic beams are shown in fig. 12 as a function of  $\gamma_{T2}$ , for beams with  $\sigma_{rms}=0.5$  and F/20 optics. The theoretical focal length and  $\text{MAX}_1\{\text{MAX}\{I\}_x\}_z$  values are shown with the dotted lines. The scalings observed in the simulation match these fairly well, but the magnitude of the values indicate much less filamentation than is predicted: the focal lengths are  $\sim 3X$  larger, and the intensity maximums are  $\sim 100X$  larger. Although the intensity peaks are much smaller than predicted, there is a definite sensitivity to interaction strength, in contrast to the ponderomotive mechanism.

### iii. Filamentation of RPS Laser Beams

Next, we will consider the effect of the RPS optical smoothing method on filamentation. The profile of the RPS beam, as noted earlier, differs from a severely aberrated generic laser beam mainly in the larger extent of the RPS wavenumber spectrum; this extent is determined by the F/# of the focusing lens. Here, we vary the F/# of the RPS profile and measure the filamentation intensity increase. These are shown in fig. 13 for four cases: (a) ponderomotive mechanism only:  $\gamma_p=1.3\times 10^{-3}$ ,  $\gamma_{T2}=0$ ; (b) thermal mechanism only:  $\gamma_p=0$ ,  $\gamma_{T2}=1.2\times 10^{-8}$ ; (c) both mechanisms:  $\gamma_p=1.3\times 10^{-3}$ ,  $\gamma_{T2}=1.2\times 10^{-8}$ ; and (d) no mechanisms:  $\gamma_p=\gamma_{T2}=0$ . There is a clear trend towards smaller intensity maximums as the F/# decreases. For optics  $\leq F/5$ , there is little increase in the peak intensity compared to the levels attained in free propagation (i.e., all filamentation turned off). The threshold perturbation wavelengths for ponderomotive and thermal filamentation are about  $30\lambda_0$ , and the simulations were done on a mesh with a transverse length of  $400\lambda_0$ . Thus, as the F/# decreases more energy is put into the filamentation-stabilized wavelength region,  $\lambda_1 < 30\lambda_0$ . The amount of energy in the unstable modes ( $k_1 \gtrsim k^{\text{Th}}$  = Threshold wavenumber) is given approximately by the expression  $(1-k^{\text{Th}}[F/\#])^{3/2}$ , so different values of  $k^{\text{Th}}$  change the magnitude of the filamentation suppression effect. Also, since ponderomotive filamentation tends to have larger values of  $k^{\text{Th}}$  than thermal filamentation, the RPS method should be more effective in suppressing ponderomotive filamentation.

There are possible concerns with the RPS smoothing technique: first, the typical intensity maximum is still of order 10 times the average intensity value, even for the fastest optics. Another concern is that large laser-plasma interaction chambers and laser-fusion reactor designs require slow optics ( $\sim F/20$ ) in order to reduce damage to optics and minimize the surface area taken up by optics in the interaction chamber; fast optics can not be used in these applications. There is a possibility, however, that the many beams used in symmetrically illuminated reactor designs may provide the effect of fast optics: since any area of the pellet will be illuminated by a large number of beams incident at large relative angles, the small F/# ( $\sim F/1$ ) intensity distribution that is formed may suppress filamentation.

### iv. Filamentation of ISI Laser Beams

We now consider ISI illumination incident on the homogeneous nonabsorbing plasma. Direct comparison with the other methods is more difficult, since the inherent time dependence of ISI irradiation complicates the measurement of filamentation. The observables, instead of possessing a single value, are now represented by probability distribution functions of the independent variables  $z$ ,  $x$ , and  $t$ . As a result, filamentation parameters such as intensity peaks or focal distances can be defined in many different ways which give different values; we often use more than one definition when evaluating a parameter. (In the following, a time average of a distribution  $I(x,z,t)$  is denoted by the brackets  $\langle \rangle$ , defined as:  $\langle I(x,z) \rangle = \int dt' I(x,z,t') / \int dt'$ .)

An example of ISI with only the ponderomotive force acting is shown in fig. 14. The interaction parameters are  $\gamma_p=0.0051$ ,  $\tau=3.2$ , and  $n_e/n_{crit}=0.5$ ; the incident lens is F/20, and 10 echelon steps are resolved on the  $200\lambda_0$  wide calculational mesh. Fig. 14(c) shows the intensity distribution  $\langle I(x,z) \rangle$  averaged over 84 coherence times. Little intensity magnification is seen: the peak average intensity ( $\text{MAX}\{\langle I(x,z) \rangle\}_x$ ) is only  $\sim 1.5$  times the incident peak average intensity ( $\text{MAX}\{\langle I(x,z=0) \rangle\}_x = 1.28 I_0$ ). One of the most noticeable changes in the intensity is the development of high wavenumbers in the spatial structure as it propagates into the plasma. Plots of the instantaneous irradiation at  $42$  and  $84t_c$  exhibit high intensity filaments (peak intensities as large as  $12X I_0$ ) in the plasma. These filamentary structures move about rapidly in the plasma and produce a much smoother time-averaged distribution. This is favorable for hydrodynamic or other long-time scale processes which will respond only to the smoothed average intensity distribution. However, many laser-plasma parametric instabilities (e.g., SRS, SBS,  $2\omega_p$ , etc.) have growth times on the order of the laser coherence time and may respond to the rapidly shifting intensity spikes. The

magnitude of the differences in these two distributions is seen by comparing the time-averaged intensity maxima in the plasma,  $\langle \text{MAX}\{I(z,x,t)\} \rangle_x$ , to the maxima of the time-averaged intensity,  $\text{MAX}\{\langle I(x,z) \rangle\}_x$  (fig. 15a). The averaged intensity maxima show the long term existence of these spikes; the average maximum intensity is  $\sim 10I_0$ , compared to the average incident maximum of  $3.8I_0$ .

Another measure of the importance of the instantaneous filaments is given by the intensity probability distribution at a given point in the plasma. The (time averaged) incident intensity probability distribution is  $p_I(I/I_0) = \exp(-I/I_0)$ ; filamentation effects cause enhancement of the higher intensity portion of this distribution as the laser propagates into the plasma. When this enhancement occurs, it is useful to know how much energy resides in filaments; it could then be possible to estimate how much energy is available to drive other plasma instabilities. The energy redistribution is found by integrating the first moment of the intensity probability distribution function to determine how much energy is at or above a certain intensity. We call this the integrated energy distribution function (IEDF), and define it here as:

$$\text{IEDF}(I/I_0) \equiv \int_{I/I_0}^{\infty} dX X p_I(X) / \int_0^{\infty} dX X p_I(X)$$

The incident distribution function is:  $\text{IEDF}(I/I_0, z=0) = (1+I/I_0) \exp(-I/I_0)$ . The change in this distribution is shown as a function of the propagation distance in fig. 15b, where the high intensity enhancement due to filament formation is evident. The total amount of energy in the high intensity region is significant:  $\sim 5\%$  of the energy appears at intensities greater than  $\sim 9I_0$  in the bulk of the plasma. In contrast, at  $z=0$ ,  $\sim 0.1\%$  of the energy is at intensities greater than  $9I_0$ .

The density variations responsible for the filaments observed in the instantaneous intensity distributions are relatively small,  $\text{MAX}\{|\delta n_e/n_0|\}_{x,z} \sim 5\%$  (fig. 16). These shallow density channels produce filaments because the phase shifts are integrated over several hundred  $\lambda_0$  propagation distances. This is particularly true in these homogeneous nonabsorbing plasmas, since the coupling is high over the entire propagation region. In contrast, the high coupling regions in laboratory plasmas are much smaller in size, and occur after most of the propagation (and most of the absorption) has taken place; we find in the next section that laboratory plasmas generally do not give rise to the magnitude of filamentation seen in these simple plasmas.

The results of this particular simulation can be compared to the theory. Using Table II, we find that the fastest growing mode for  $\gamma_p \tau_c^{1/2} = 9.1 \times 10^{-3}$  and  $n/n_c = 0.5$  is  $\lambda_1 \approx 30\lambda_0$ . This mode is close to the minimum intensity wavelength generated by the F/20 optics ( $20\lambda_0$ ). The characteristic growth length ( $k^{-1}$ ) of this fastest growing mode is  $\lambda_g \approx 1800\lambda_0$  (Table II), and corresponds to a focal length  $l_f \approx 320\lambda_0$  (appendix). There are several ways of measuring a time-averaged focal length in the simulation, of which three are used here: (1.) the position of highest time-averaged maximum intensity ( $l_f$  at  $\text{MAX}\{\langle I \rangle_x\}_z$ ); (2.) the position of highest maximum time-averaged intensity ( $l_f$  at  $\text{MAX}\{\langle I \rangle_{x,z}\}$ ); and (3.) the time-averaged position of maximum intensity ( $l_f$  at  $\langle \text{MAX}\{I\}_{x,z} \rangle$ ). (1.) and (2.) can be found directly from fig. 15(a), the third is calculated during the simulation. These values are: (1.)  $200\lambda_0$ ; (2.)  $162.5\lambda_0$ ; and (3.)  $242\lambda_0$ , respectively. All are somewhat less than the predicted value; this suggests that the averaging done by the plasma is nonlinear, as it responds more to the intensity peaks in the distribution than the time averaged values.

As a more general test of the ISI theory, we examine a larger range of parameters, and calculate the scaling behavior. Many ISI ponderomotive filamentation runs have been made with different values of both interaction strength and coherence time.<sup>33</sup>  $\gamma_p$  and  $\tau_c$  were independently varied in the ranges  $5 \times 10^{-4} < \gamma_p < 2 \times 10^{-2}$  and  $0.05 < \tau_c < 3.2$ . All simulations shown in fig. 17 were done with 40 echelon steps, F/20 optics, and  $n/n_c = 0.5$  on a mesh  $200\lambda_0$  across; the results are not sensitive to  $F/\#$  (for  $F \gtrsim 10$ ) or mesh size. The focal lengths (using the three methods of determination mentioned previously) are shown as a function of the theoretical scaling parameter  $\gamma_p \tau_c^{1/2}$ . The dotted line is the focal length range expected from theory, as determined by the fastest growing mode occurring in the incident radiation. At the lower powers, the fastest growing mode varies as  $\sim \gamma_p \tau_c^{1/2} \sim 10^{-4/3}$  (table II). At higher intensities, the fastest growing mode in table II has a wavelength smaller than any in the incident spectrum ( $\lambda_{\min} = 20\lambda_0$ ), so  $\lambda_{\min}$  should be the fastest growing mode. The focal lengths at higher powers should then vary as  $\sim \gamma_p \tau_c^{1/2-1/3}$ . The data is

closer to the  $[\gamma_p \tau_c^{1/2}]^{-1/2}$  variation throughout; a least squares fit using all of the points gives  $I_f \sim [\gamma_p \tau_c^{1/2}]^{-0.54}$ . This scaling suggests that the dominant fastest growing wavelength ( $\lambda_1^{\max}$ ) is constant.

The averaged maximum intensities are plotted as a function of  $\gamma_p \tau_c^{1/2}$  in fig. 17(b). There is a distinct separation of these averaged values: the time averaged maximum values,  $\langle \text{MAX}\{I\} \rangle$ , are always much larger than the maximum time averaged values,  $\text{MAX}\{\langle I \rangle\}_x$ . There seems to be little consistent variation in the latter as the interaction strength is increased, whereas the values of  $\langle \text{MAX}\{I\} \rangle_x$  increase as  $\sim [\gamma_p \tau_c^{1/2}]^{1/3}$ .

Thermal filamentation calculations were also done using ISI illumination in these simple plasmas. An example is shown in detail in fig. 18; this particular simulation is performed with F/20 optics,  $\tau_c = 0.53$ ,  $n/n_c = 0.5$ ,  $\gamma_{T2} = 2 \times 10^{-6}$ , and  $\gamma_{T1} = 3.8 \times 10^{-4}$ . Even with incoherent illumination, the characteristic signature of thermal filamentation is apparent in the instantaneous intensity distributions: the filaments attract one another, forming large modes composed of high wavenumber structure. Again, this is associated with large-scale density and temperature fluctuations (fig. 19). As in the ponderomotive mechanism, the time averaging smears out most of the structure seen in the snapshots; however, significant structure in both high and low-wavenumber modes can still be seen in the time average, especially in the lowest order modes.

Once again the time-averaged distribution is much smoother than the instantaneous distributions suggest; the averaged maximum intensity  $\langle \text{MAX}\{I\} \rangle_x$  is significantly larger than the maximum averaged intensity  $\text{MAX}\{\langle I \rangle\}_x$  (fig. 20a). The energy distribution looks very similar to the ponderomotively driven case (fig. 20b; cf. fig. 15b); the integrated energy distribution function reveals that ~5% of the laser energy is at intensities greater than  $10I_0$ , comparable to the ponderomotive example.

In fig. 21 the theoretical predictions are compared with a wide variety of runs at different intensities and coherence times.  $\gamma_{T2}$  and  $\tau_c$  were independently varied in the ranges  $2.5 \times 10^{-7} < \gamma_{T2} < 5 \times 10^{-6}$  and  $0.5 < \tau_c < 5.4$ . All of the simulations included the theoretical fastest growing mode in the incident intensity spectrum, so the growth length should scale as  $[\gamma_{T2} \tau_c^{1/2}]^{4/7}$ . The agreement between theory and calculation is better than expected in both scaling and magnitude. There is a large scatter in the peak intensity values  $\text{MAX}_1\{\text{MAX}\{\langle I \rangle\}_x\}_z$  for small values of  $\gamma_{T2} \tau_c^{1/2}$  because the focusing is very mild; these intensities are only a few percent greater than the incident peak (fig. 21b). Such peaks are probably due to statistical scattering of the light, not filamentation. The expected separation between the values of  $\text{MAX}\{\langle I \rangle\}_x$  and  $\langle \text{MAX}\{I\} \rangle_{x,z}$  is observed, and a slight dependence on the interaction strength ( $\sim [\gamma_{T2} \tau_c^{1/2}]^{1/25}$ ) is noted.

These simulations of ISI in simple plasmas show that the ISI filamentation formulas in table II are only moderately accurate. The focal length predictions fit the observed thermal filamentation behavior (fig. 21a) better than the observed ponderomotive filamentation behavior (fig. 17a). This can be explained by noting that thermal filaments experience longer time-averaging than ponderomotive filaments. The ponderomotively unstable filaments are smaller in size (so the averaging time  $\lambda_1/C_s$  is smaller) than the thermally unstable modes. Since they are averaged less, ponderomotively driven perturbations have a larger statistical deviation. Some perturbation modes (that happen to be larger than average) will grow faster, and produce shorter focal lengths, than predicted. This is the behavior seen with the ponderomotive simulations in fig. 17a. Thus, it is reasonable to expect our ISI filamentation theory to model thermal filamentation more accurately than ponderomotive filamentation.

#### C. Filamentation of Complex Laser Beams in Laboratory Plasmas

We conclude the analysis with a treatment of filamentation in more realistic (i.e., absorbing and inhomogeneous) plasmas, in particular those that are produced in ICF research laboratories or foreseen for ICF applications. We cannot attempt an exhaustive description, as there is a huge range of conditions encountered in these laboratory plasmas; instead, we concentrate on examples of plasmas that are generated by moderately high power laser light at wavelengths of  $1.08\mu\text{m}$ ,  $0.53\mu\text{m}$ , and  $0.25\mu\text{m}$ . These wavelengths correspond to Nd-glass lasers, frequency-doubled Nd-glass lasers, and KrF or Nd-glass frequency-quadrupled lasers, respectively. For the  $1.08$  and  $0.53\mu\text{m}$  cases, plasma profiles were generated by the NRL FAST2D hydrocode to simulate near-term flat-target experiments<sup>12,34,35</sup>; the two-dimensional density and temperature distributions are averaged in the transverse direction to produce the one-dimensional density and temperature profiles used in the code. The  $0.25\mu\text{m}$  laser-

plasma profile was generated by the NRL FAST1D hydrocode<sup>36</sup> in a simulation of a few-megajoule KrF-driven reactor-sized pellet<sup>1</sup>. The first two plasmas have scalelengths on the order of  $10^3 \lambda_0$ , while the last is a plasma with a scalelength on the order of  $10^4 \lambda_0$ . These density and temperature profiles, along with the associated laser parameters, are shown in fig. 22. In all of the calculations presented here, the laser light is propagated in the region from  $0.01n_{\text{crit}}$  to  $0.5n_{\text{crit}}$ ; propagation to higher density is limited by the assumptions underlying the validity of the parabolic wave equation. The filamentation coupling is high in the region between  $0.01$  and  $0.5n_{\text{crit}}$ , but the propagation distance is small, and the absorption is relatively high (especially for the shorter wavelength plasmas). Thus, little additional filamentation should occur in this higher density region.

In each plasma there is a range of perturbation wavelengths over which either the ponderomotive or thermal mechanism dominates. Thermal filamentation dominates at larger scales, ponderomotive at the shorter scales. As noted in section III.A, these regions are delineated by the characteristic wavelength  $\lambda_1/\lambda_0 = (\gamma_p/\gamma_{T2})^{1/2}$ . As the laser wavelength decreases (with constant intensity), the relevant plasma density increases and the plasma temperature decreases slightly (due to the higher plasma heat capacity). Thus, with smaller laser wavelength, the ponderomotive contribution decreases ( $\gamma_p \sim \lambda_0^2$ ), the thermal contribution increases ( $\gamma_{T2} \sim T_e^{-5}$ ), and thermal filamentation dominates over a wider range of wavelengths. In addition, the absorption rate ( $\kappa_b \sim n_e T_e^{3/2}$ ) of the plasma increases as the laser wavelength decreases. The higher absorption raises the filamentation threshold and lowers the growth rate, since the filament must now grow faster than it is absorbed. We find that absorption can effectively suppress filamentation in shorter wavelength plasmas.

The  $1.06\mu\text{m}$  laser-plasma absorbs little laser light in the region  $0.01n_{\text{crit}}$  to  $0.5n_{\text{crit}}$ , and the ponderomotive mechanism is strong ( $\gamma_p \sim 0.016$ ,  $\gamma_{T2} \sim 2 \times 10^{-7}$  at  $n/n_{\text{crit}} = 0.25$ ). The ponderomotive mechanism dominates the thermal mechanism for  $\lambda_1 \gtrsim 270\lambda_0$ , which includes most of the range of the simulations. This plasma efficiently filaments laser light, including incident light that is very uniform. Fig. 23a shows simulation results for generic laser profiles with different incident  $\sigma_{\text{rms}}$ : incident beams with perturbation levels  $\sigma_{\text{rms}} \gtrsim 0.05$  begin to filament. Since most high-power laser beams have  $\sigma_{\text{rms}} > 0.05$ , this implies that filamentation is a common event at this laser wavelength. Using a random-phase screen with 80 phase shift sections and F/5 optics does not improve matters significantly: filaments with peak intensities  $\gtrsim 25I_0$  are still observed.

When ISI is applied at  $1.06\mu\text{m}$  with  $\tau_c = 0.25$  ( $t_c = 1\text{psec}$ , or  $\Delta w/w \approx 0.003$ ), filamentation is appreciably, but not completely, suppressed (compare fig. 24b to fig. 23a). The instantaneous intensity distributions (fig. 24a), the time averaged intensity maximums ( $\langle \text{MAX}\{I\} \rangle_x$ , fig. 24b), and the integrated energy distribution (fig. 24c) all show evidence of instantaneous filament formation. The integrated energy distribution reveals constantly increasing levels of energy at all intensity levels; although the beam begins with less than  $5 \times 10^{-2}\%$  of its energy above  $10I_0$ , at  $n/n_{\text{crit}} = 0.5$ , more than 2% of its energy is above  $10I_0$ . The structure of these instantaneous filaments (fig. 24a) reflects the dominance of the ponderomotive filamentation mechanism. The time averaged intensity distribution (averaged over  $250\tau_c$  (fig. 24d) is much smoother, since the filaments move about and do not concentrate in a single area. Residual fluctuations left on the incident profile show little growth compared to generic beams ( $\text{MAX}\{\langle I \rangle\}_{x,z} \gtrsim 2I_0$  in fig. 24d; cf. fig. 23a where  $\text{MAX}\{\langle I \rangle\}_{x,z} \sim 10-40I_0$ ).

Filamentation is less dominant in the plasma created with the  $0.53\mu\text{m}$  wavelength laser. Although a significant fraction of the incident light gets to  $0.5n_{\text{crit}}$ , and the plasma is 60% larger than the plasma at  $1.06\mu\text{m}$ , the smaller laser wavelength reduces the ponderomotive force effect ( $\gamma_p \approx 0.0057$  at  $n/n_{\text{crit}} = 0.25$ ). Thermal filamentation is stronger ( $\gamma_{T2} \sim 3 \times 10^{-7}$ ), and should dominate ponderomotive effects for filaments with  $\lambda_1 \gtrsim 80\lambda_0$ . With generic laser profiles (fig. 23b), we find that filamentation begins to occur when a moderate fluctuation level ( $\sigma_{\text{rms}} \gtrsim 0.3$ ) is incident; this fluctuation level is well within the typical range. The RPS method with F/5 optics suppresses filamentation somewhat, reducing filament intensities to about 12 times the average intensity (square symbols, fig. 23b).

When ISI is applied to the  $0.53\mu\text{m}$  plasma with  $\tau_c = 1$  ( $t_c = 3.1\text{psec}$ , or  $\Delta w/w \approx 1.7 \times 10^{-5}$ ), it suppresses filamentation about as well as the  $1.06\mu\text{m}$  case (fig. 25; cf. fig. 24). Apparently the smaller interaction strength is offset by the longer interaction region (as measured in laser wavelengths) in this plasma. Although thermal filamentation is stronger in this plasma, the structure of the intensity distributions suggests that ponderomotive effects are still quite dominant.

Finally, we consider filamentation in the  $0.25\mu\text{m}$  laser wavelength plasma. At  $n_e/n_{\text{crit}}=0.25$ , the ponderomotive mechanism ( $\gamma_p \sim 8.8 \times 10^{-4}$ ) dominates the thermal filamentation mechanism ( $\gamma_{T2} \sim 3.7 \times 10^{-8}$ ) for filament sizes  $\lambda_f \lesssim 150\lambda_0$ . Thermal filamentation is actually less important here than in the  $0.53\mu\text{m}$  case because  $Z$  is smaller ( $Z=1$  as opposed to  $Z=3.5$ ) and the temperature is slightly greater (due to a higher intensity and longer pulse length). This example is also different from the other two cases because it has a much longer plasma scalelength, as would be generated in a direct-drive laser-fusion reactor. The large scalelength presents a worse-case test for filamentation at this wavelength, since it provides a longer gain path for the unstable modes. Counteracting this effect is the higher absorption efficiency of short-wavelength laser plasmas. The amount of filamentation in these plasmas will be determined by which one of these two opposing effects is dominant.

Generic laser beams filament in this  $0.25\mu\text{m}$  plasma when the incident perturbation level is greater than  $\sigma_{\text{rms}} \sim 0.2$  (fig. 23c). The  $\text{MAX}\{I\}_{x,z}$  vs.  $\sigma_{\text{rms}}$  curve is similar to the curves from the longer laser wavelength interactions, except that the peak intensities are smaller. These smaller intensities are due primarily to the higher absorption rate. The RPS method with F/5 optics does not appear to significantly affect the filamentation tendency (see the square symbols in fig. 23c); peak filament intensities  $\gtrsim 12I_0$  are still observed.

ISI is significantly more effective at suppressing filamentation in this  $0.25\mu\text{m}$  plasma than it is at the longer laser wavelengths. Applying ISI with  $\tau_c=1$  ( $t_c=0.9\text{psec}$ , or  $\Delta\omega/\omega \approx 9 \times 10^{-4}$ ) eliminates filamentation over both short and long time averages (figs. 26a and 26d). The integrated energy distribution (fig. 26c) and  $\text{MAX}\{I\}_x$  curves (fig. 26b) show steadily decreasing energy levels at all intensities as the beam propagates into the plasma. In addition, the ratio  $\text{MAX}\{\langle I \rangle\}_x - \text{MIN}\{\langle I \rangle\}_x\}/\langle I_{\text{avg}}(z) \rangle$  (fig. 26b) shows that the nonuniformity level is not increasing as the laser propagates. The high absorptivity of the plasma appears to dominate any filamentation enhancements due to the longer plasma scalelength.

## V. Conclusions

We have examined ponderomotive and thermal filamentation mechanisms for Gaussian, ISI, RPS, and generic (typical) laser beams in laser-produced plasmas. Time-dependent and steady-state laser-plasma propagation codes have been constructed to simulate filamentation under these conditions. A standard theoretical formulation of filamentation was presented and extended to account for incoherent light, such as that found in ISI laser beams. The predictions of this analysis were then compared to the results of the laser-plasma propagation codes. First, a simple plasma (homogeneous and non-absorbing) was used to study quantitative aspects of filamentation, and to compare the results to the theory. Then, simulations were done with realistic laboratory plasmas to determine the importance of filamentation in more complex experimental environments.

There is a distinctive behavior that differentiates the ponderomotive and thermal-conduction dominated filamentation mechanisms. In general, ponderomotively-driven filaments interact locally through interference effects of the light waves; these filaments tend to be independent from one another. In thermally-driven filamentation, the high plasma conductivity creates long-scale density gradients that cause light filaments to attract one another at large distances. This attraction mechanism decreases the spatial coherence of the beam, increases the width of the perturbation wavenumber spectrum, and can reduce or stabilize further large-scale self focusing. At high powers, the effect is enhanced by the nonlinear behavior of the temperature profile.

Simulations of Gaussian laser beams show the limitations of the theoretical analysis. The ponderomotive focal length predictions agree quite well with the theoretical predictions, but the behavior of the light in and after the first focus can differ markedly from the predictions. Gaussian beams undergoing thermal filamentation agree with theoretical predictions only at lower intensities; at higher intensities the focal length increases rather than decreases, and the peak intensities decrease rather than increase. Both of these effects are due to the stabilization effects of the nonlinear temperature profile. In both the ponderomotive and thermal filamentation cases, peak intensities found in the simulations fall far short of their predicted values.

There are significant discrepancies between the perturbation theory and the simulations for the generic and RPS smoothed laser beams: the fastest-growing mode is often different than predicted, and the growth rates for most longer wavelength unstable modes are lower than predicted. The supposedly stable higher wavenumber modes grow, apparently due to nonlinear mode-mode coupling. In spite of these discrepancies, comparisons of the results to the theoretical focal length scaling laws show rough agreement. Comparisons to the peak intensity scaling laws are again poor. The RPS optical control technique is able to suppress filamentation under some plasma conditions, but requires relatively fast focusing optics ( $\leq F/5$ ).

The ISI smoothing technique is first simulated in homogenous, nonabsorbing plasmas. Time averages on the order of a hundred coherence times show relatively smooth laser illumination, but there can be a simultaneous increase in the proportion of laser energy at the higher intensities. This has important implications for nonlinear interactions that respond to the light on times of order of the laser coherence time ( $\sim$ psec). Scaling studies of the ISI focal lengths show agreement between theory and calculations. In contrast, the maximum intensity levels in the plasma are found to be relatively insensitive to the interaction strength, in disagreement with our theoretical predictions.

Simulations using near-term laboratory plasmas demonstrate that filamentation tends to be much stronger at longer laser wavelengths (i.e.,  $\lambda = 1.06\mu\text{m}$  and  $0.53\mu\text{m}$ ). Ponderomotive filamentation is dominant at  $1.06\mu\text{m}$ , and is exacerbated by the relatively small underdense-plasma absorption. Generic beams of high quality and RPS-smoothed beams both filament rapidly (producing filament intensities  $\sim$ 25-30 times the average). ISI also shows some evidence of enhanced energy at higher intensity in the  $1.06\mu\text{m}$  laser-plasma. The strong filamentation tendency exhibited by the  $1.06\mu\text{m}$  wavelength interaction (also at  $0.53\mu\text{m}$ ) underscores the importance of filamentation in near-term laser-plasma experiments: the laser-plasma interactions at these longer laser wavelengths are probably dominated by filamentation effects.

In reactor-sized plasmas at shorter laser wavelengths ( $\lambda_o=0.25\mu m$ ), the increased absorption reduces filamentation for all types of laser beams. When filamentation occurs, maximum intensities are ~10-15 times the average incident intensity. RPS smoothed beams do not reduce these maximum intensity levels. However, the ISI smoothing technique or very clean beam profiles ( $\sigma_{rms} \leq 1$ ) can eliminate filamentation in short wavelength laser plasmas.

Acknowledgements

The author would like to acknowledge valuable discussions with Dr. S. Bodner, Dr. R.H. Lehmberg, and Dr. S. Obenschain. This research was supported by the U.S. Department of Energy.

## Appendix

The quasi-optic equation (2.3) can be solved using the paraxial approximation, which consists of expanding the nonlinear dielectric constant in the transverse variable and keeping only the first order, quadratic terms<sup>3</sup>. It is a well known that a beam that initially has a Gaussian intensity profile and a constant or quadratically varying phase front remains Gaussian as it propagates through a quadratically varying dielectric constant. We thus consider a Gaussian filament for consistency. The electric field of the filament is written:

$$\psi(x, \eta) = \psi_0(x) \left[ \frac{a_0}{a(\eta)} \right]^{N/2} \exp\{-x^2/2a(\eta)^2 + i(\phi_0(\eta) + \phi_1(\eta)x^2)\} \quad (A.1)$$

where  $a(\eta)$  is the 1/e radius of the filament at distance  $\eta$ ,  $a_0$  is the initial filament radius,  $N$  is the number of transverse dimensions, and  $\phi_0$  and  $\phi_1$  are real. As written, the field conserves energy as  $a(\eta)$  varies. Inserting (A.1) in equation (2.3), using the paraxial approximation  $\epsilon(\eta, x) \approx \epsilon(\eta, x=0) + (\partial[\epsilon(\eta, x=0)]/\partial[x^2])x^2$  (assume that  $\partial\epsilon/\partial x^2$  is real), separating real and imaginary parts, and equating like powers of  $x$ , we find the following equation for the filament radius  $a(\eta)$ :

$$4\pi^2 \frac{d^2 a(\eta)}{d\eta^2} = \frac{1}{a(\eta)^3} + 4\pi^2 \frac{\partial\epsilon}{\partial x^2} a(\eta) \quad (A.2)$$

### A.1 Ponderomotive Filamentation

For ponderomotive filamentation,  $\partial\epsilon(\eta, x)/\partial x^2 = \partial(n_e(\eta, x)/n_c)/\partial x^2 \approx -n_{eo}/n_c \gamma_p a(\eta)^{-2} (a_0/a(\eta))^N$ , where  $\gamma_p$  is evaluated at  $x=0$ . This leads to the equation:

$$4\pi^2 \frac{d^2 a(\eta)}{d\eta^2} = \frac{1}{a(\eta)^3} - 4\pi^2 \frac{(n/n_c)\gamma_p a_0^N}{a(\eta)^{1+N}} \quad (A.3)$$

The filamentation threshold is determined when  $da(\eta)/d\eta = 0$  and  $d^2 a(\eta, z=0)/d\eta^2 = 0$  at  $\eta=0$ . The threshold filament radius is:

$$a_{op}^{th} \geq \frac{1}{2\pi} \left( \frac{n}{n_c} \gamma_p \right)^{-1/2} \quad (A.4)$$

This radius is independent of the dimension  $N$ , and agrees with table I if we define the effective perturbation wavelength of the Gaussian distribution to be  $\lambda_{fp}(\text{Gaussian}) = \pi\sqrt{2}a_0 \approx 4.4a_0$  (assuming  $2n/n_c \gamma_p \ll N$ ).

The solutions are dependent upon  $N$ , and are straightforward when  $n/n_c$  is independent of  $\eta$ , and  $\eta = z/\epsilon_0^{1/2}$ . For  $N=2$ , the solution of (A.3) is:

$$a^2(\eta) = a_0^2 + \frac{(1-4\pi^2(n/n_c)\gamma_p a_0^2)}{4\pi^2 \epsilon_0} \left( \frac{z}{a_0} \right)^2 \quad (A.5)$$

This predicts that for filaments above threshold, the radius will go to zero at:

$$\lambda_{fp}(N=2) = 2\pi \epsilon_0^{1/2} a_0^2 \left[ 4\pi^2 \frac{n}{n_c} \gamma_p a_0^2 - 1 \right]^{-1/2} \approx \frac{\epsilon_0^{1/2} a_0}{\left( \frac{n}{n_c} \gamma_p \right)^{1/2}} \quad (A.6)$$

The collapse of the filament to zero radius at  $z=l_{fp}$  occurs in this model because the dielectric constant (previous to (A.3)) is approximated as directly proportional to the intensity. The induced  $\epsilon$  causes refractive forces that are always larger than diffractive forces, and the filament collapses to zero radius and infinite peak intensity. In a real plasma, the induced  $\epsilon$  saturates at  $\epsilon=1$ , and diffraction eventually overtakes the filamentation forces when the radius is of the order of  $\lambda$ . Although the solution is technically invalid at  $z=l_{fp}$ , the collapse is rapid enough that the solution is valid close to  $l_{fp}$ , and  $l_{fp}$  is a good approximation to the focal distance in the real case. This value is in agreement with table I if we use the previous definition of the Gaussian wavelength ( $\lambda_{fp}=\pi\sqrt{2}a_0$ ), and define the Gaussian growth wavelength  $\lambda_{gp}=2\pi l_{fp}$ .

When  $N=1$  the solution  $a(z)$  to (A.3) is:

$$\left[Ca(z)^2 + 2\beta a(z) - 1\right]^{1/2} = \frac{z}{z_0} - \frac{\beta}{|C|^{1/2}} \left[ \frac{\pi}{2} + \sin^{-1} \left[ \frac{Ca(z) + \beta}{(C + \beta^2)^{1/2}} \right] \right] \quad (A.7)$$

where:  $z_0 \equiv \frac{2\pi\epsilon^{1/2}}{|C|^{1/2}}$ ;  $C \equiv (1-2\beta a_0)/a_0^2$ ; and  $\beta \equiv 4\pi^2(n/n_c)\gamma_p a_0$ .

$\beta a_0 = 1$  is equivalent to the threshold condition given by (A.4). This displays a focal length given by:

$$l_{fp}(N=1) = \frac{8\pi^4 a_0^4 (n/n_c) \gamma_p \epsilon_0^{1/2}}{(8\pi^2 (n/n_c) \gamma_p a_0^2 - 1)^{3/2}} \approx \frac{\pi a_0 \epsilon_0^{1/2}}{(8\frac{n}{n_c} \gamma_p)^{1/2}} \quad (A.8)$$

The approximation on the RHS of (A.8) is valid for filaments far over threshold:  $8\pi^2(n/n_c)\gamma_p a_0^2 >> 1$ . In this limit,  $l_{fp}(N=1) = (\pi/\sqrt{8})l_{fp}(N=2) \approx 1.1l_{fp}(N=2)$ , and matches table I if we define  $\lambda_{gp}=4\sqrt{2}l_{fp}(N=1) \approx 5.7l_{fp}(N=1)$ . Like the perturbation analysis in section III, this model predicts very similar focal lengths for  $N=1$  and  $N=2$ .

The minimum filament radius, attained at  $l_{fp}$ , is:

$$\frac{a_{\min}}{a_0} = \left[ 8\pi^2 \frac{n}{n_c} \gamma_p a_0^2 - 1 \right]^{-1}$$

Thus, the maximum filament intensity ( $\text{MAX}\{I\}_x/I_0 = a_0/a_{\min}$ ) exhibits a linear dependence on the incident filament intensity.

#### A.2 Thermal Filamentation

For the thermal conduction dominated filamentation mechanism, the dielectric constant expansion gives  $\partial\epsilon(\eta, x)/\partial x^2 = \partial(n_e(\eta, x)/n_c)/\partial x^2 \approx -2\pi^2(n/n_c)\gamma_{T2}(a_0/a(\eta))^N$ . Substituting this in (A.2) yields:

$$4\pi^2 \frac{d^2 a(\eta)}{d\eta^2} = \frac{1}{a(\eta)^3} - 8\pi^4 (n/n_c) \gamma_{T2} a_0^N a(\eta)^{1-N} \quad (A.9)$$

The filamentation threshold is then:

$$a_{0T}^{\text{Th}} \geq \frac{1}{\pi} \left[ 3\frac{n}{n_c} \gamma_{T2} \right]^{-1/4} \quad (A.10)$$

This agrees with table I if we define the effective perturbation wavelength as  $\lambda_{1T} = \pi\sqrt{2}a_{oT}$ , the same relation as we have previously found. The solution  $a(\eta, \gamma_{T2})$  for  $N=1$  can be found by integrating eqn (A.9) twice. First it is helpful to define the transform variables  $u = (8\pi^4(n/n_c)\gamma_{T2}a_o)^{1/3}a(z)$  and  $y = (8\pi^4(n/n_c)\gamma_{T2}a_o)^{2/3}z/2\pi\sqrt{\epsilon_o}$ . Then (A.9) can be expressed in a canonical form:

$$\frac{d^2u(y)}{dy^2} = \frac{1}{u(y)^3} - 1 \quad (A.11)$$

Integrating this twice, we find:

$$*y = \int_{u_o}^{u(y)} \frac{u \, du}{[2(u_o - u)(u - u_+)(u - u_-)]^{1/2}} \quad ,$$

where:

$$u_o = (8\pi^4 \frac{n}{n_c} \gamma_{T2} a_o^4)^{1/3} \quad ,$$

$$u_+ = \frac{1 + [1 + 8u_o^3]^{1/2}}{4u_o^2} \quad ,$$

and:

$$u_- = \frac{1 - [1 + 8u_o^3]^{1/2}}{4u_o^2} \quad .$$

This has the solution:

$$y = 2^{1/2} u_- (u_o - u_+)^{-1/2} F\left(\left[\frac{u_o - u}{u_o - u_+}\right]^{1/2}; \frac{u_o - u_+}{u_o - u_-}\right) \\ + [2(u_o - u_-)]^{1/2} E\left(\left[\frac{u_o - u}{u_o - u_+}\right]^{1/2}; \frac{u_o - u_+}{u_o - u_-}\right) \quad (A.12)$$

where  $F(\phi; p)$  and  $E(\phi; p)$  are elliptic integrals of the first and second kind, defined as:<sup>37</sup>

$$F(\phi; p) = \int_0^\phi dx \left[ (1 - px^2)(1 - x^2) \right]^{-1/2}$$

$$E(\phi; p) = \int_0^\phi dx \left[ (1 - px^2)/(1 - x^2) \right]^{1/2}$$

In the limit  $u_o \gg 1$  (i.e.,  $a_o \gg 1$ ), eqn (A.12) can be simplified; using the limiting forms  $E(\phi;1)=\phi$ ,  $F(\phi;1)=\ln(\sec(\sin^{-1}\phi)+\tan(\sin^{-1}\phi))$ , and  $u_+ \approx (2u_o)^{-1/2}$  we find:

$$y = -\frac{1}{u_o} \ln \left[ \left( \frac{u_o}{u(y)} \right)^{1/2} (1 + \left( 1 - \frac{u(y)}{u_o} \right)^{1/2}) \right] + \sqrt{2} [u_o - u(y)]^{1/2} \quad (A.13)$$

The focus occurs where  $u(y)=u_+$  (this is the minimum radius achieved by the filament), at  $y_f \approx (2u_o)^{1/2}$ . Transforming back, we find the focal length:

$$l_{FT} = \frac{1}{\pi} \left[ \frac{\epsilon_o}{(n/n_c)\gamma_{T2}} \right]^{1/2} \quad (A.14)$$

This is again independent of the filament radius, and agrees with the sinusoidal perturbation result (table I) if we define the Gaussian growth wavelength as  $\lambda_{gT} = \sqrt{2\pi}l_{FT}$ . The maximum intensity, which occurs at the focus, is:

$$\frac{I_{\max}}{I_o} = \frac{u_o}{u_+} \approx \sqrt{2} u_o^{3/2} = 4\pi^2 \left[ \frac{n}{n_c} \gamma_{T2} \right]^{1/2} a_o^2 \quad (A.15)$$

References

1. A.J. Schmitt and J.H. Gardner, *J. Appl. Phys.* 60, 6 (1986).
2. S. Skupsky and K. Lee, *J. Appl. Phys.* 54, 3671 (1983);  
A.J. Schmitt, *Appl. Phys. Lett.* 44, 399 (1984).
3. Y.R. Shen, *Prog. Quant. Electr.* 4, 1 (1975);  
J.H. Marburger, *Prog. Quant. Electr.* 4, 35 (1975); and references therein.
4. P.K. Kaw, G. Schmidt, and T. Wilcox, *Phys. Fluids* 16, 1522 (1973).
5. C. Max, *Phys. Fluids* 19, 74 (1976).
6. F.W. Perkins and E.J. Valeo, *Phys. Rev. Lett.* 32, 1234 (1974);  
V.K. Tripathi and L.A. Pitale, *J. Appl. Phys.* 48, 3288 (1977).
7. E. Kane and H. Hora, *Austr. Journ. Phys.* 34, 385 (1981).
8. H.A. Baldis and P.B. Corkum, *Phys. Rev. Lett.* 45, 1260 (1980);  
M.J. Herbst, J.A. Stamper, R.R. Whitlock, R.H. Lehmberg, and B.H. Ripin, *Phys. Rev. Lett.* 46, 328 (1981);  
Z. Lin, *Opt. Commun.* 42, 351 (1982);  
K.A. Tanaka, B. Boswell, R.S. Craxton, L.M. Goldman, F. Guglielmi, W. Seka, R.W. Short, and J.M. Soures, *Phys. Fl.* 28, 2910 (1985).
9. R.H. Lehmberg and S.P. Obenschain, *Opt. Comm.* 46, 27 (1983);  
R. Lehmberg, A. Schmitt, and S. Bodner, *Journ. Appl. Phys.*, in press.
10. Y. Kato and K. Mima, *Appl. Phys.* B29, 186 (1982).
11. Y. Kato, K. Mima, N. Miyanaga, S. Arinaga, Y. Kitagawa, M. Nakatsuka, and C. Yamanaka, *Phys. Rev. Lett.* 53, 1057 (1984).
12. S.P. Obenschain, J. Grun, M. Herbst, K. Kearney, C. Manka, E. McLean, A. Mostovych, J. Stamper, R. Whitlock, S. Bodner, J. Gardner, and R. Lehmberg, *Phys. Rev. Lett.* 56, 2807 (1986).
13. Y. Kitagawa, T. Yabe, Y. Kato, and C. Yamanaka, *Phys. Rev. Lett.* 56, 2804 (1986).
14. R.H. Lehmberg and J. Goldhar, *Fusion Tech.* 11, 532 (1987).
15. R.S. Craxton and R.L. McCrory, *Journ. Appl. Phys.* 56, 108 (1984);  
K. Estabrook, W.L. Kruer, and D.S. Bailey, *Phys. Fluids* 28, 19 (1985).
16. S. Sartang, R.G. Evans, and W.T. Toner, *J. Phys. D: Appl. Phys.* 16, 955 (1983).
17. J.A. Stamper, R.H. Lehmberg, A. Schmitt, M.J. Herbst, F.C. Young, J.H. Gardner, and S.P. Obenschain, *Phys. Fluids* 28, 2563 (1985).
18. A 3D version of the computer code presented here has been used to simulate ISI filamentation driven by the ponderomotive force only. Preliminary runs were performed with  $1.06\mu\text{m}$  wavelength ISI light in the plasma shown in fig. 22a. The results indicated that although some filaments grow to much higher intensities, they do not contain much energy: the intensity probability distributions are similar to the 2D results shown in section IV (fig. 24).
19. M.S. Sodha, A.K. Ghatak, and V.K. Tripathi, *Progress in Optics*, Vol XIII (E. Wolf, ed.), Amsterdam: North-Holland, 1976, and references therein.
20. A.J. Schmitt and R.S.B. Ong, *J. Appl. Phys.* 54, 3003 (1983).
21. M.S. Sodha, D.P. Singh, and R.P. Sharma, *J. Appl. Phys.* 50, 2678 (1979).
22. J.A. Fleck, J.R. Morris, and M.D. Feit, *Appl. Phys.* 10, 129 (1976).
23. K. Lee, D.W. Forslund, J.M. Kindel, and E.L. Lindman, *Phys. Fluids* 20, 51 (1977);  
C.E. Max, C.F. McKee, and W.C. Mead, *Phys. Fluids* 23, 1620 (1980);  
W.M. Manheimer, D.G. Colombant, and J.H. Gardner, *Phys. Fluids* 25, 1644 (1982).
24. N.E. Andreev, V.P. Silin, and P.V. Silin, *Sov. Phys. JETP* 52, 653 (1980);  
R.W. Short, R. Bingham, and E.A. Williams, *Phys. Fluids* 25, 2302 (1982);  
V.V. Amelin and L.A. Zelekszon, *Sov. J. Plasma Phys.* 10, 625 (1984);  
A.A. Andreev, I.G. Lebo, and V.B. Rozanov, *Sov. J. Quantum Electron.* 16, 1412 (1986).
25. M.J. Herbst, J. Stamper, R. Lehmberg, R. Whitlock, F. Young, J. Grun, and B. Ripin, *NRL Memorandum Report 4983* (1982).
26. A.R. Bell, R.G. Evans, and D.J. Nicholas, *Phys. Rev. Lett.* 46, 243 (1981).
27. P.K. Kaw, G. Schmidt, and T. Wilcox, *Phys. Fl.* 16, 1522 (1973).
28. V.A. Petrishev, *Radio. Quant. Elec.* 14, 1062 (1971).
29. D.J. Nicholas and S.G. Sajjadi, *J. Phys. D: Appl. Phys.* 12, 737 (1986).

30. V.V. Korobkin and V.N. Sazonov, Sov. Phys. JETP 54, 636 (1981);  
A.B. Langdon, 1983 Laser Program Annual Report, Lawrence Livermore National Laboratory, Livermore CA, UCRL-50021-83 (1983), p.3-35.
31. Ya.B. Zel'dovich and Yu.P. Raizer, Physics of Shock Waves and High Temperature Hydrodynamic Phenomena, Vol II (Academic Press, New York, 1967).
32. E. Valeo, Phys. Fluids 17, 1391 (1974);  
S. Coggeshall, W. Mead, and R. Jones, Bull. Am. Phys. Soc. 31, 1585 (1986).
33. Varying the coherence time arbitrarily has practical limitations: as the bandwidth decreases ( $t_c$  increases), the ISI echelon steps must be thick enough to satisfy the requirement that all of the beamlets are temporally incoherent with respect to one another. The maximum thickness step must be at least  $cNt_c$  long for an echelon with N total sections; N is typically of order several hundred.
34. J. Gardner, private communication.
35. A.J. Schmitt, Bull. Am. Phys. Soc. 31, 1408 (1986).
36. J.H. Gardner and S.E. Bodner, Phys. Fluids 29, 2672 (1986).
37. M. Abramowitz and I.E. Stegun, Handbook of Mathematical Functions, (National Bureau of Standards, Washington DC, 1964).

Table I  
Steady State Filamentation Parameters

Ponderomotive:

A.  $\bar{k}_1^{\text{Th}}$ ; Threshold Perturbation Wavenumber:

$$\{\bar{k}_{1P}^{\text{Th}}\}^2 \leq \left\{ \frac{1}{2 \frac{n}{n_c} \gamma_p} + \frac{1}{N\epsilon_0} \right\}^{-1}$$

Thermal:

$$\{\bar{k}_{1T}^{\text{Th}}\}^2 \leq \left\{ 2 \frac{n}{n_c} \gamma_{T2} \right\}^{1/2}$$

B.  $\bar{k}_g$ ; Spatial Growth Rate:

$$\bar{k}_{gP} = \frac{1}{2\sqrt{\epsilon}} \bar{k}_1^2 \left\{ 2 \frac{n}{n_c} \gamma_p \left[ \bar{k}_1^{-2} - \frac{1}{N\epsilon_0} \right] - 1 \right\}^{1/2}$$

$$\bar{k}_{gT} = \frac{1}{2\sqrt{\epsilon_0}} \left\{ 2 \frac{n}{n_c} \gamma_{T2} \left[ 1 - \frac{\bar{k}_1^2}{N\epsilon_0} \right] - \bar{k}_1^4 \right\}^{1/2}$$

$$\bar{k}_{gP} \approx \bar{k}_1 \left\{ \frac{1}{2\epsilon_0} \frac{n}{n_c} \gamma_p^{-1} \right\}^{1/2}$$

$$\bar{k}_{gT} \approx \left\{ \frac{1}{2\epsilon_0} \frac{n}{n_c} \gamma_{T2} - \bar{k}_1^2 \right\}^{1/2}$$

C.  $\bar{k}_1^{\text{max}}$ ; Fastest Growing Perturbation Wavenumber:

$$\{\bar{k}_{1P}^{\text{max}}\}^2 = \frac{1}{2} \left\{ \frac{1}{2n/n_c \gamma_p} + \frac{1}{N\epsilon_0} \right\}^{-1}$$

$$\bar{k}_{1T}^{\text{max}} = 0$$

D.  $\bar{k}_g^{\text{max}}$ ; Fastest Spatial Growth Rate:

$$\bar{k}_{gP}^{\text{max}} = \frac{1}{2} \frac{n}{n_c} \gamma_p \left\{ \epsilon_0 + \frac{2}{N} \frac{n}{n_c} \gamma_p \right\}^{-1/2}$$

$$\bar{k}_{gT}^{\text{max}} = \left\{ \frac{1}{2\epsilon_0} \frac{n}{n_c} \gamma_{T2} \right\}^{1/2}$$

$$\bar{k}_{gP}^{\text{max}} \approx \frac{1}{2} \frac{n}{n_c} \frac{\gamma_p}{\sqrt{\epsilon_0}}$$

Table II  
ISI Filamentation Parameters

Ponderomotive:

A.  $\bar{k}_{1P}^{\text{Th}}$ ; Threshold Perturbation Wavenumber:

$$\bar{k}_{1P}^{\text{Th}} \leq \left[ 2 \frac{n}{n_c} \gamma_p \tau_c^{1/2} \right]^{2/3}$$

Thermal:

$$\bar{k}_{1T}^{\text{Th}} \leq \left[ 2 \frac{n}{n_c} \gamma_{T2} \tau_c^{1/2} \right]^{2/7}$$

B.  $\bar{k}_g$ ; Spatial Growth Rate:

$$\bar{k}_{gP} \approx \frac{1}{2\sqrt{\epsilon_0}} \bar{k}_1^2 \left\{ 2 \frac{n}{n_c} \gamma_p \tau_c^{1/2} \bar{k}_1^{-3/2} - 1 \right\}^{1/2} \quad \bar{k}_{gT} \approx \frac{1}{2\sqrt{\epsilon_0}} \bar{k}_1^2 \left\{ 2 \frac{n}{n_c} \gamma_{T2} \tau_c^{1/2} \bar{k}_1^{-7/2} - 1 \right\}^{1/2}$$

C.  $\bar{k}_1^{\text{max}}$ ; Fastest Growing Perturbation Wavenumber:

$$\bar{k}_{1P}^{\text{max}} \approx \left[ \frac{5}{4} \frac{n}{n_c} \gamma_p \tau_c^{1/2} \right]^{2/3}$$

$$\bar{k}_{1T}^{\text{max}} \approx \left[ \frac{1}{4} \frac{n}{n_c} \gamma_{T2} \tau_c^{1/2} \right]^{2/7}$$

D.  $\bar{k}_g^{\text{max}}$ ; Fastest Spatial Growth Rate:

$$\bar{k}_{gP}^{\text{max}} \approx \frac{0.52}{\sqrt{\epsilon_0}} \left( \frac{n}{n_c} \gamma_p \tau_c^{1/2} \right)^{4/3}$$

$$\bar{k}_{gT}^{\text{max}} \approx \frac{0.6}{\sqrt{\epsilon_0}} \left( \frac{n}{n_c} \gamma_{T2} \tau_c^{1/2} \right)^{4/7}$$

These results assume that  $\bar{k}_1 \ll 1$ , and  $(n/n_c)(\gamma_p, \gamma_{T2})\tau_c^{1/2} \ll 1$ .

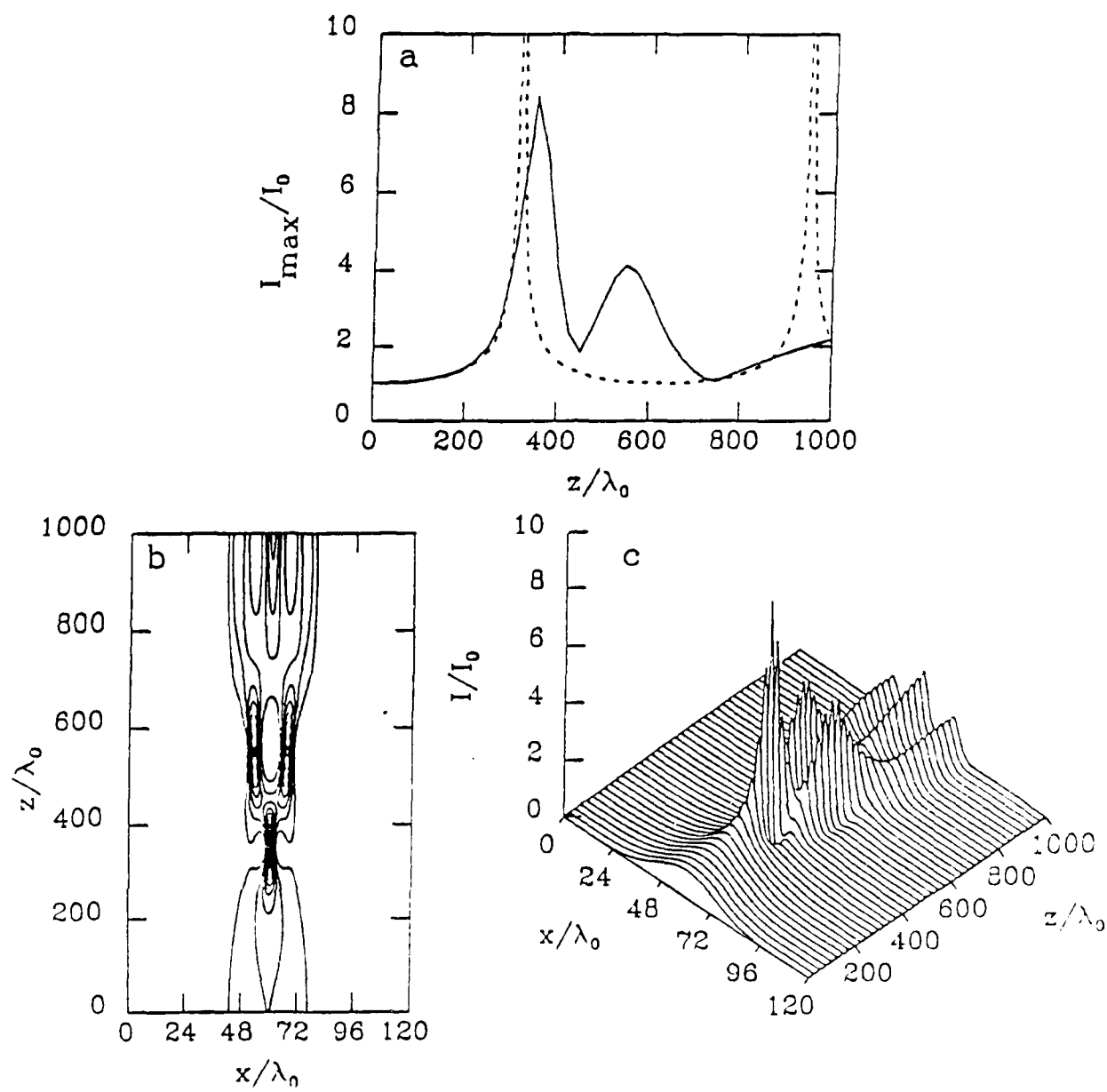


Fig. 1 Focusing of a Gaussian filament with  $\gamma = 0.005$ ,  $a_0 = 20\lambda_0$ . (a)  $\text{MAX}\{I\}_x$  vs.  $z$ ; dotted line is the analytic result [from appendix], solid line is the simulation result. (b) Contour and isometric plots of  $I(x,z)$  from the simulation.

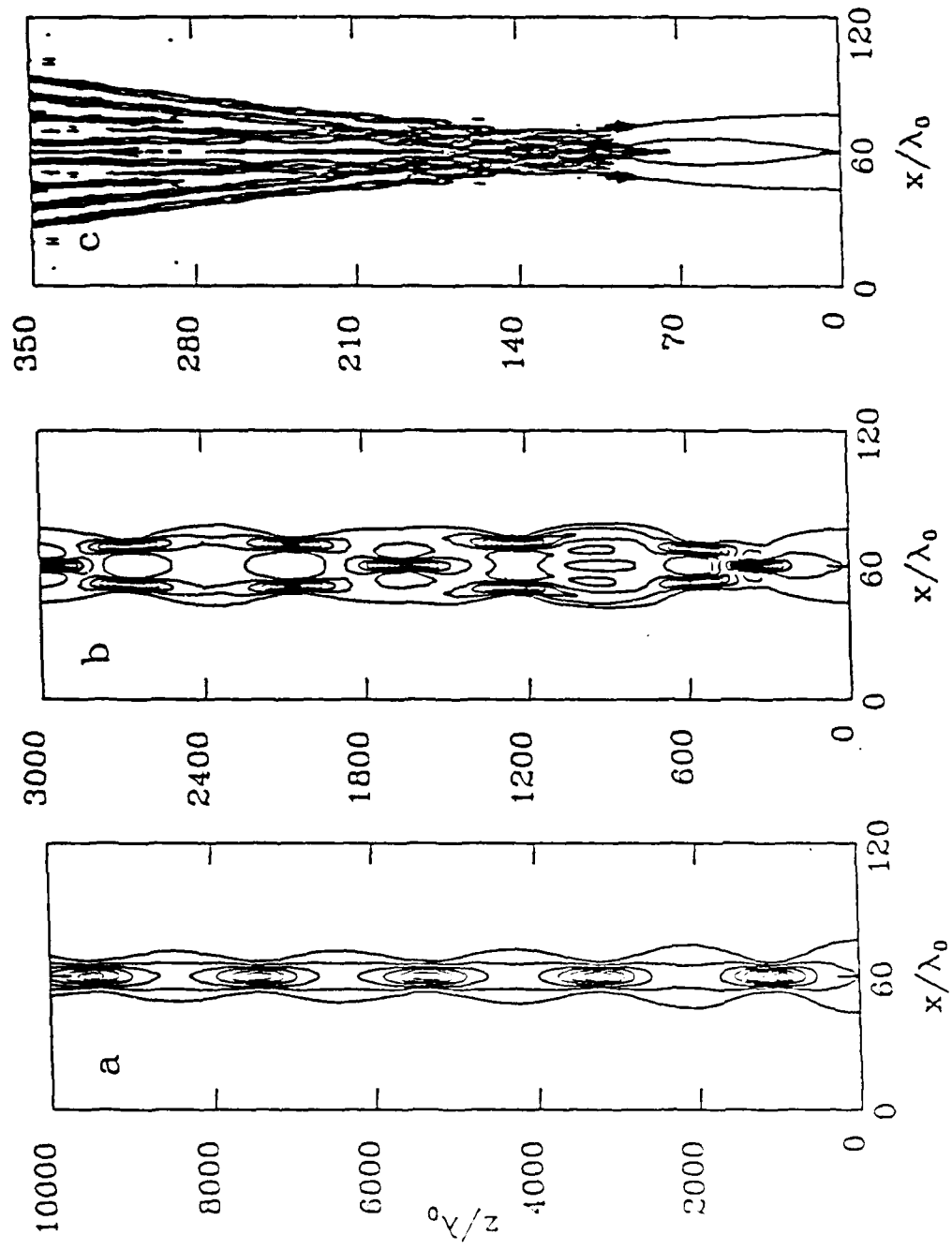


Fig. 2 Filamentation of Gaussian filaments for (a)  $\gamma = 0.0013$ ,  $a_0 = 20\lambda_0$ ; (b)  $\gamma = 0.005$ ,  $a_0 = 20\lambda_0$ ; and (c)  $\gamma = 0.05$ ,  $a_0 = 20\lambda_0$ . As the beam power increases, the beam breaks up into more filaments.

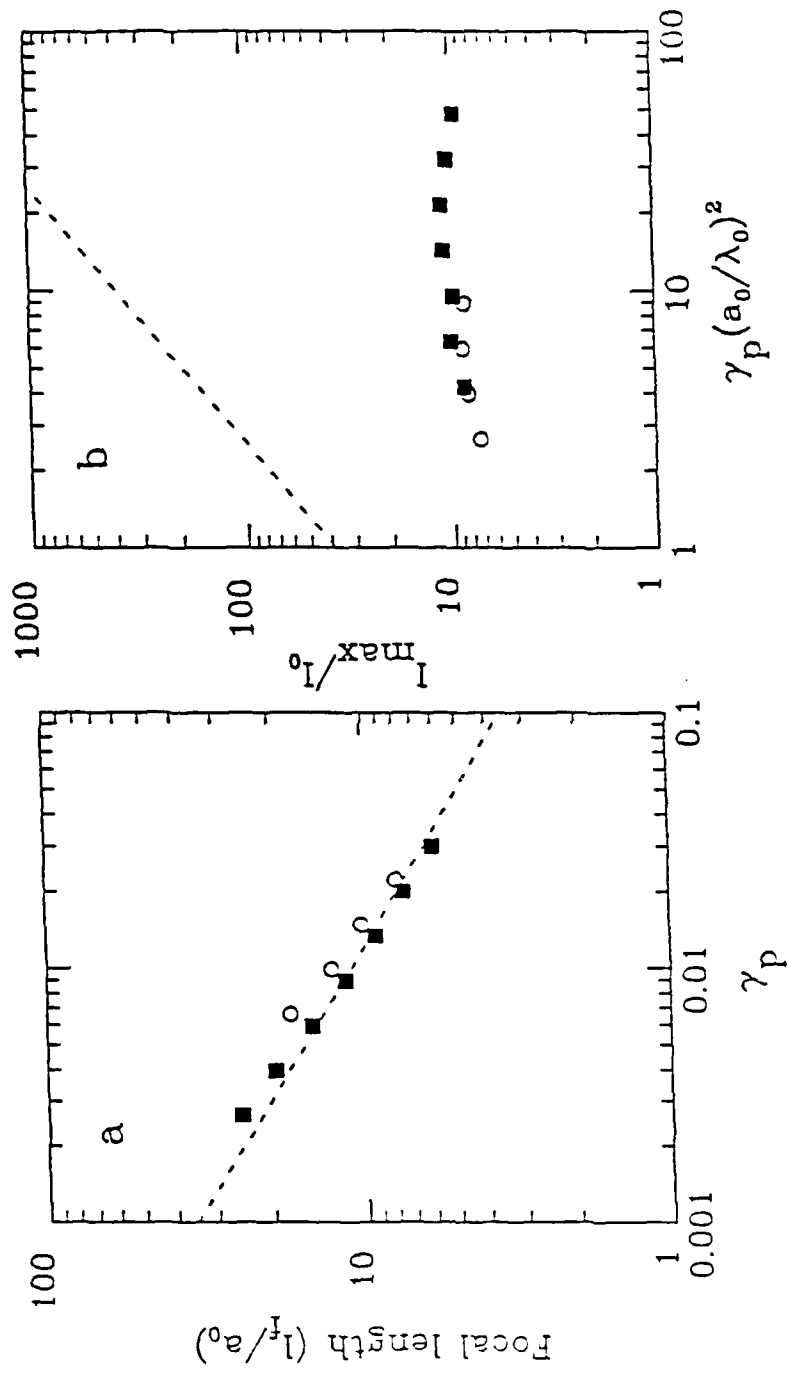


Fig. 3 Filamentation of gaussian beams:  
 (a) the normalized focal length,  $l_f/a_0$  vs.  $\gamma_p$ ,  
 and (b) focal intensity  $I_{\text{max}}/I_0$  vs.  $\gamma_p$ ; the  
 threshold power is  $\gamma_{p,0}^{\text{a}}=0.05$ . The dotted  
 line shows the predictions of the Gaussian  
 beam model given in the appendix, the dark  
 square points are calculations with  $a_0/\lambda=40$ ,  
 and the open circles are calculations with  
 $a_0/\lambda=20$ .

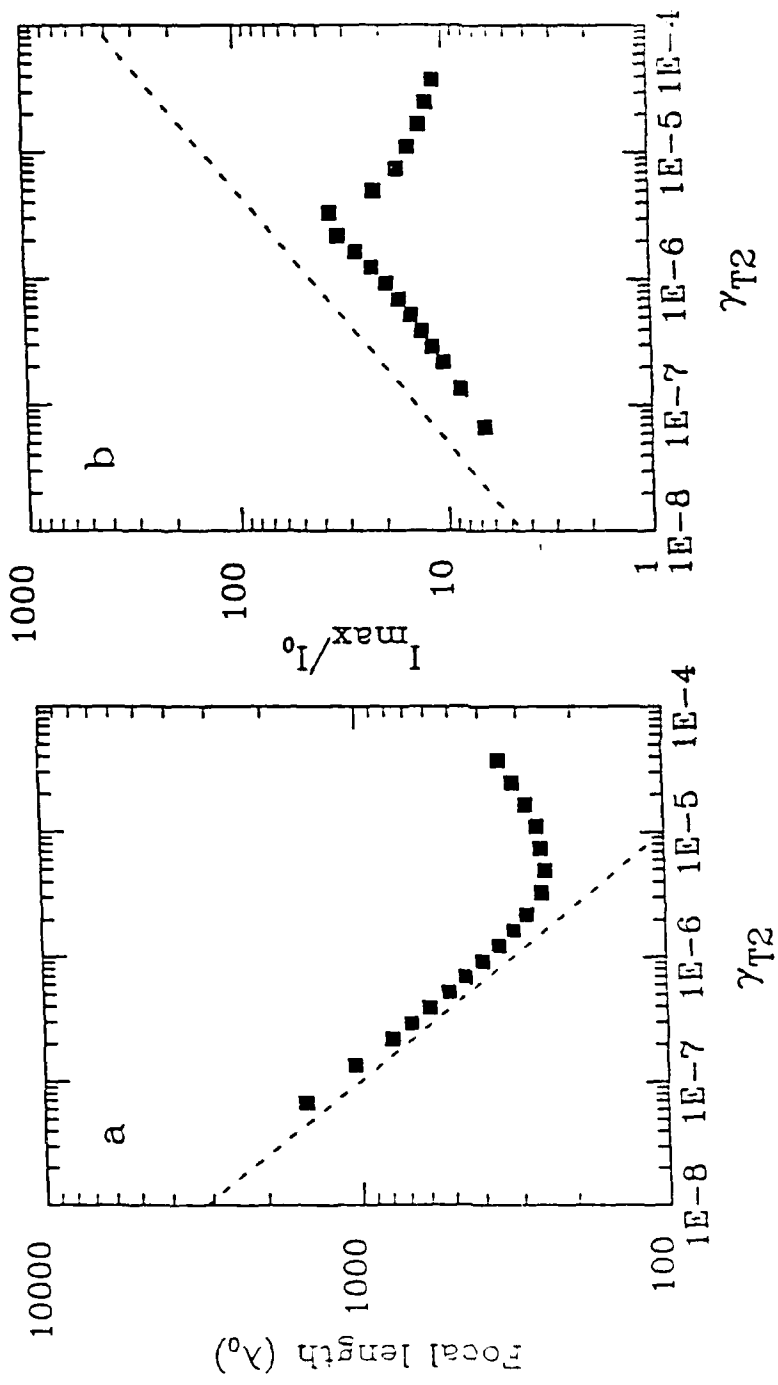


Fig. 4 Filamentation of gaussian beams:  
 (a) the focal length,  $\lambda_f$  vs.  $\gamma_{T2}$ , and  
 (b) focal intensity,  $I(z=1)$ , vs.  $\gamma_{T2}$  for  
 Gaussian beams with  $a_0 = 40\lambda_0$ .

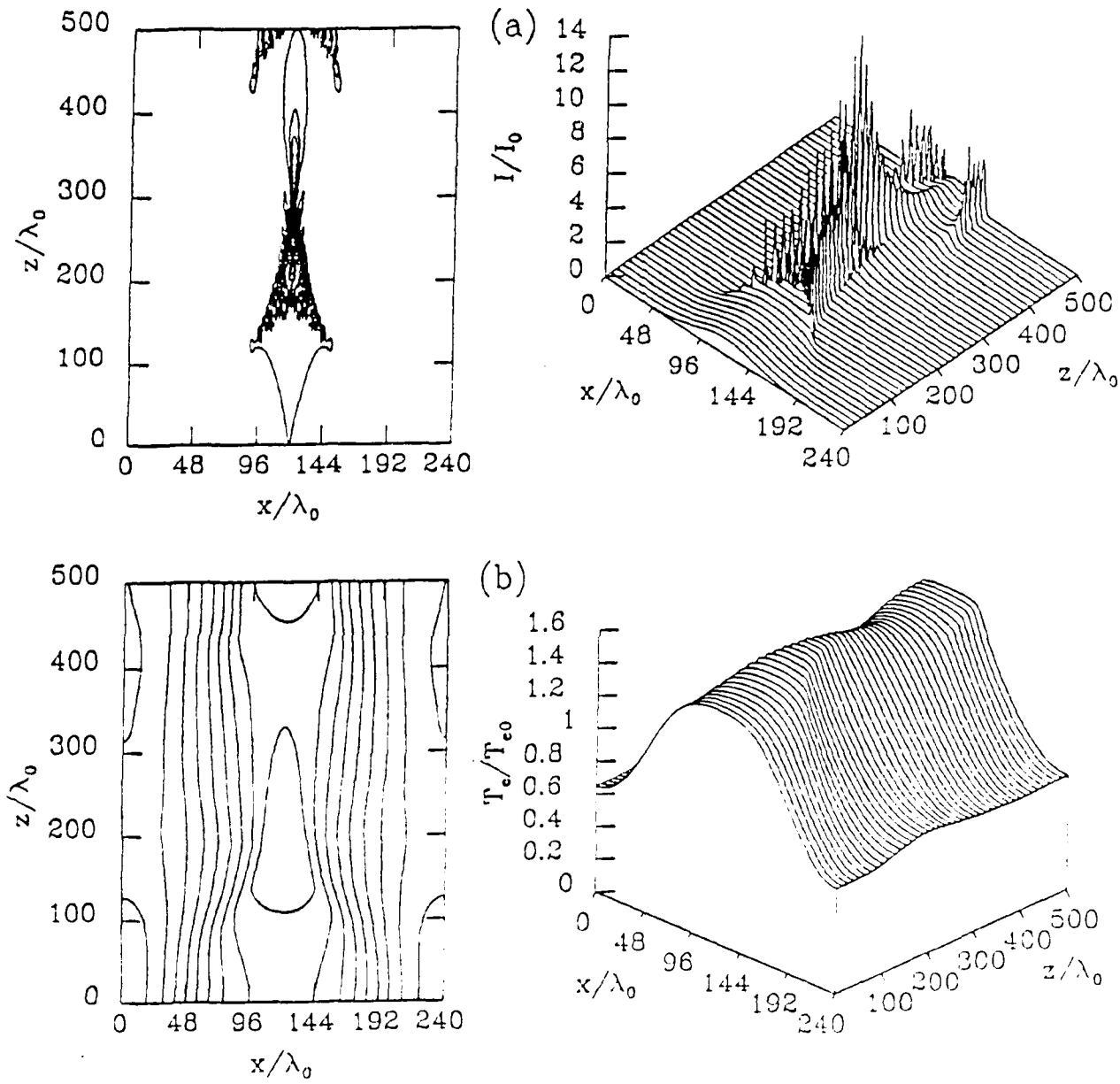


Fig. 5 Development of Gaussian beam during strong heating ( $\gamma_{T2} = 1.76 \times 10^{-5}$ ,  $a_0 = 40\lambda_0$ ). (a) intensity profile, and (b) temperature profile; both contour and isometric plots are shown.

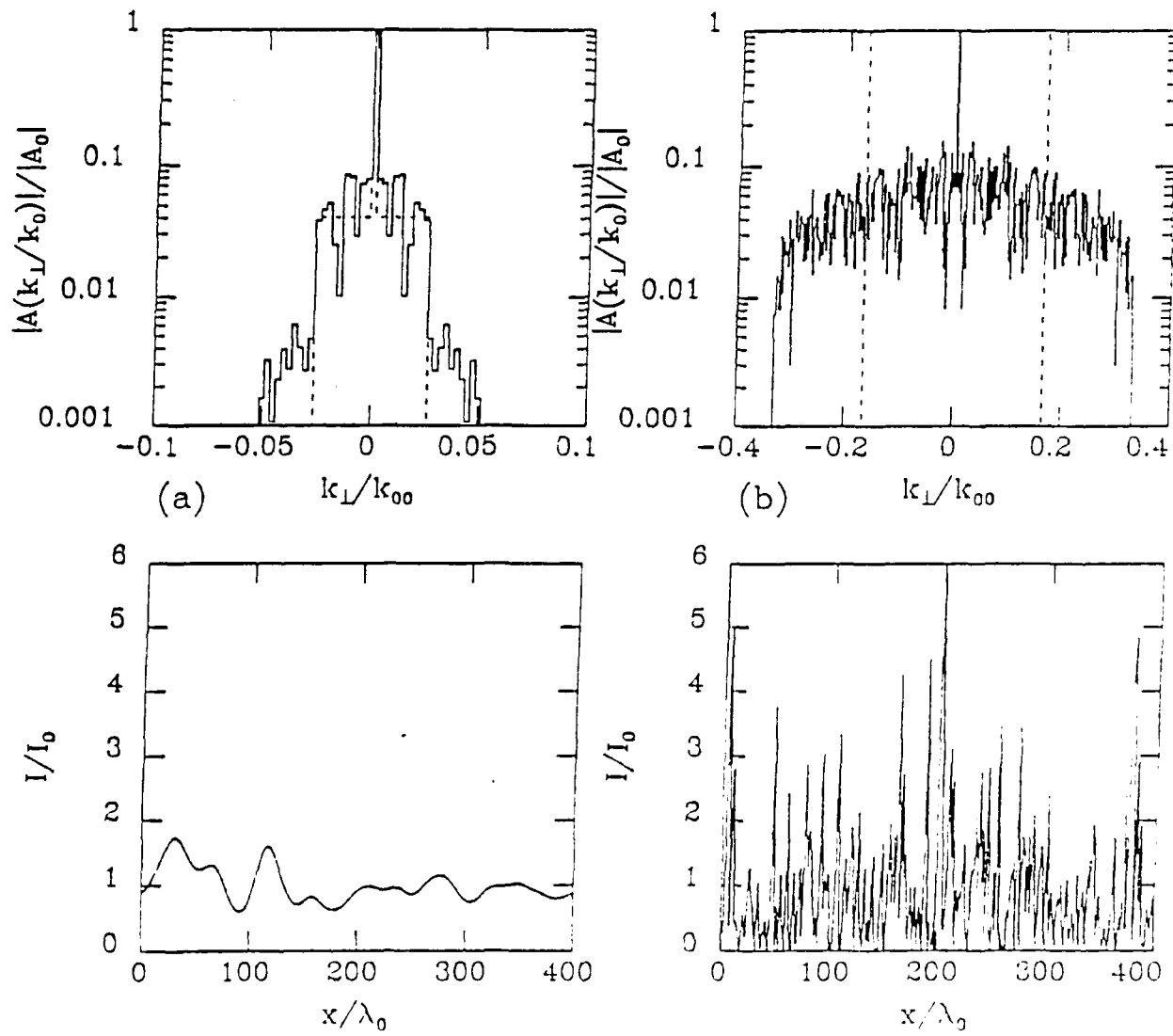


Fig. 6 Typical laser intensity profiles for (a) the generic laser beam (with  $F/20$  optics and  $\sigma_{rms}=0.25$ ); and (b) the RPS optical technique (with  $F/3$  optics). The top figures show the Fourier spectra of the electric fields (dotted lines) and the intensity (solid lines); the bottom figures show the corresponding intensity profiles  $I(x, z=0)$ .

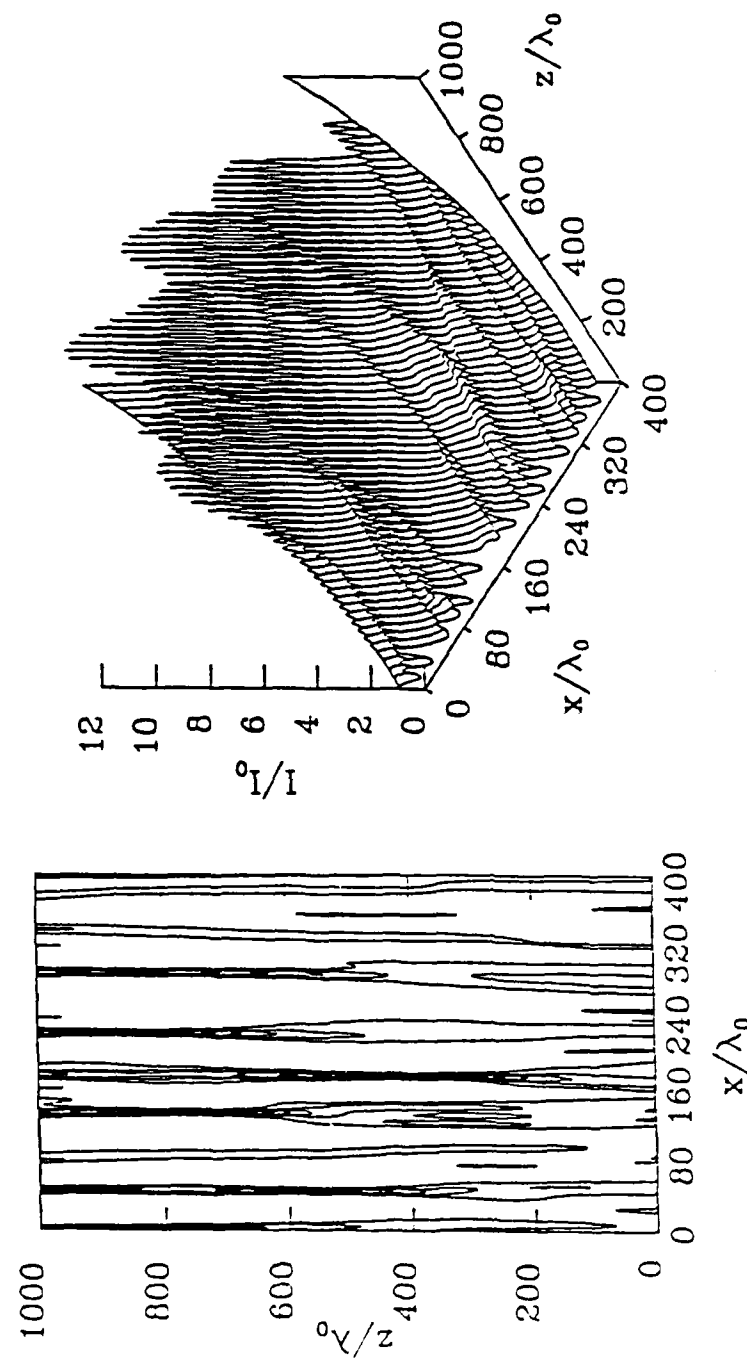


Fig. 7 Contour and isometric plots of a generic laser beam undergoing ponderomotive filamentation. Interaction parameters are:  $\gamma = 1.3 \times 10^{-3}$ ,  $n_e = 0.5 n_{\text{crit}}$ ,  $\sigma_{\text{rms}} = 0.5$ , and  $1/10$  optics.

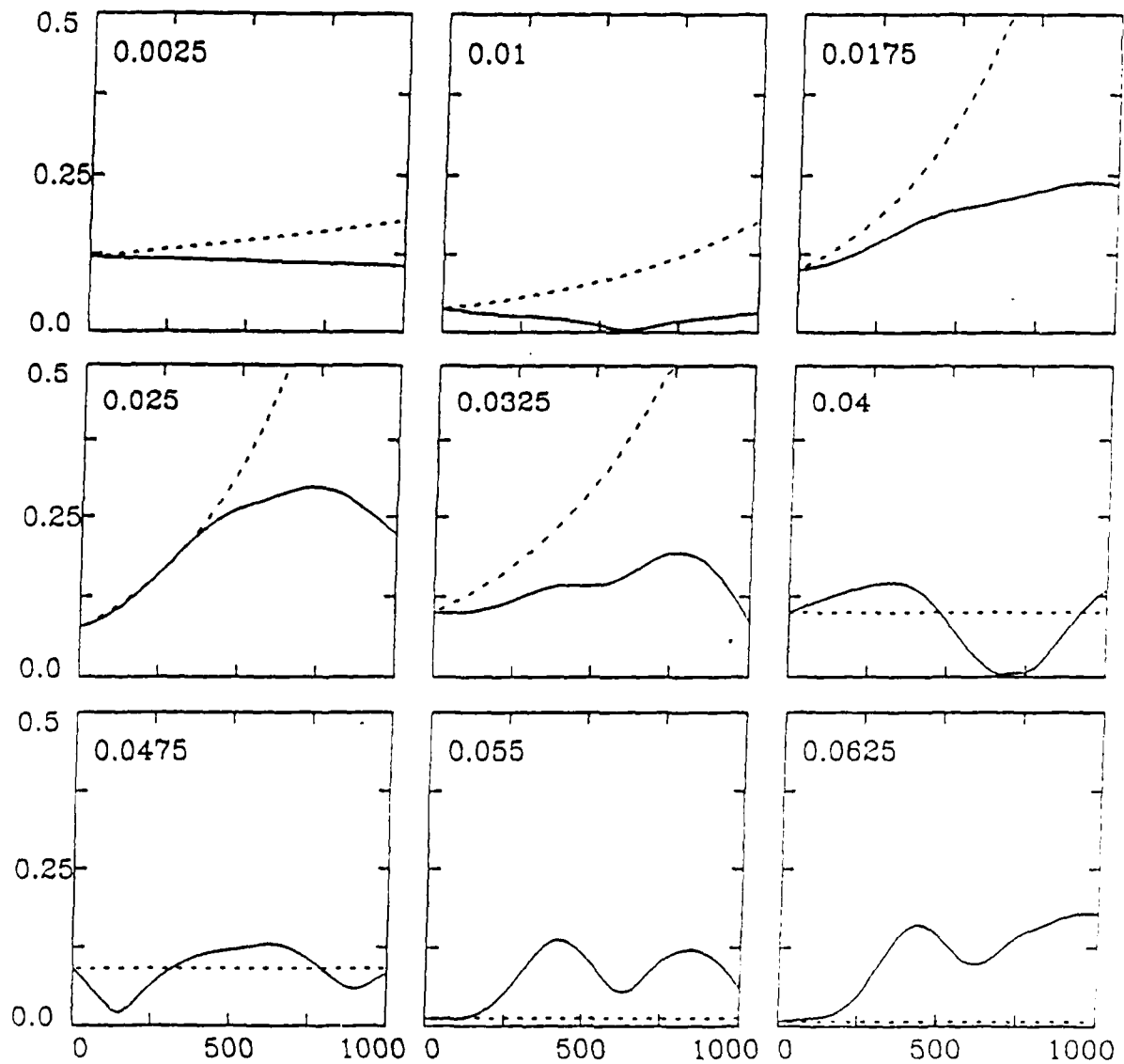


Fig. 8 The Fourier amplitudes of lowest modes of the intensity distribution shown in fig. 7, as a function of the propagation distance. The number in the upper left hand corner of each graph is the value  $k_{\perp}$  of the plotted mode. Horizontal axis is in units of  $\lambda_0$ , and the vertical axis is the normalized mode amplitude  $a(k_{\perp})/a(k_{\perp}=0)$ . The solid line shows the simulation results, while the dotted line shows theoretical predictions (table 1).

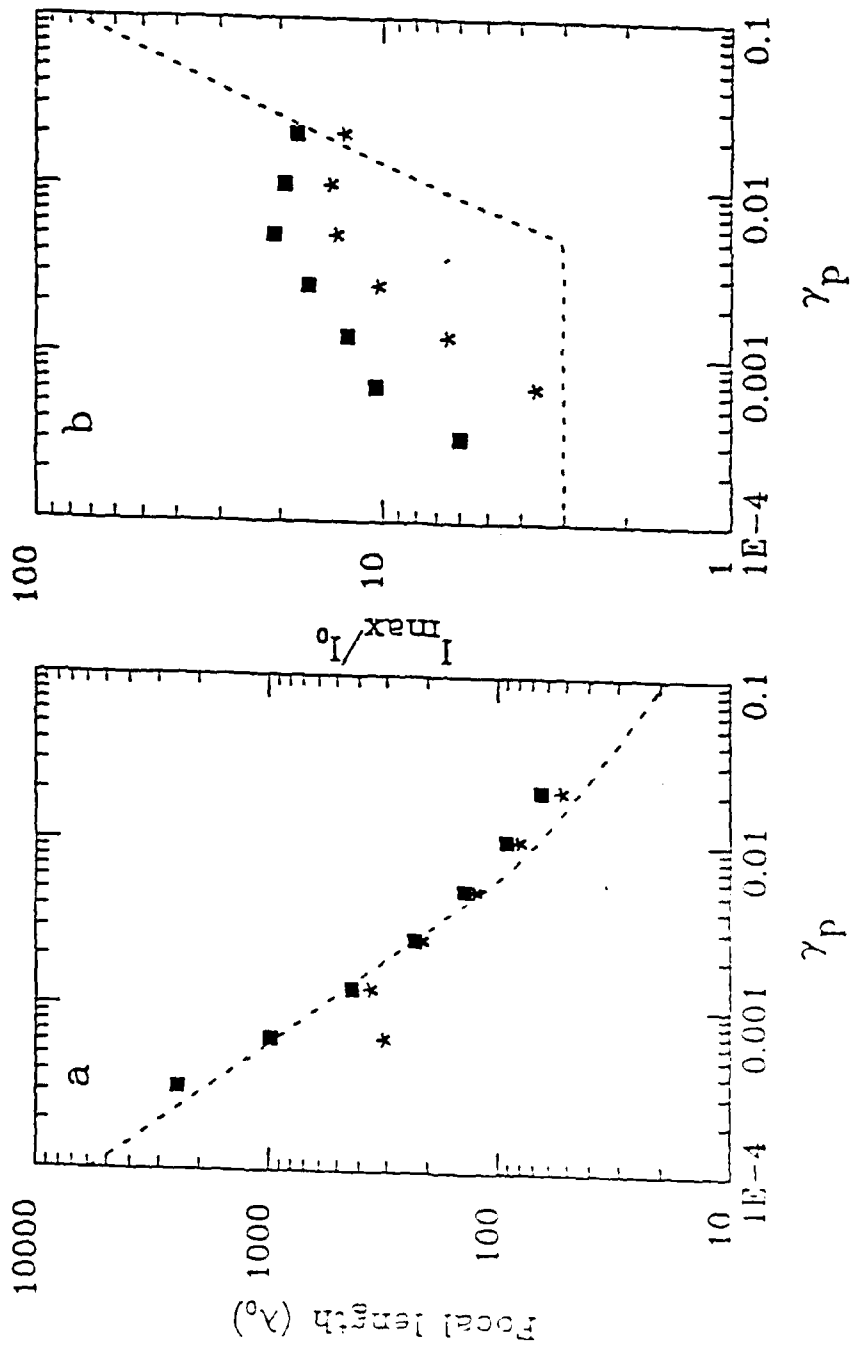


Fig. 9 Variation of  $\text{MAX}\{I\}_x$  and focal length  $f$  vs.  $\gamma_p$  for generic laser beams undergoing ponderomotive filamentation; other simulation parameters are the same as fig. 7. The dotted lines are the theoretical curves (using table I and the Appendix); the square symbols are the results using  $F/20$  optics, and the asterisk symbols are results using  $F/10$  optics.

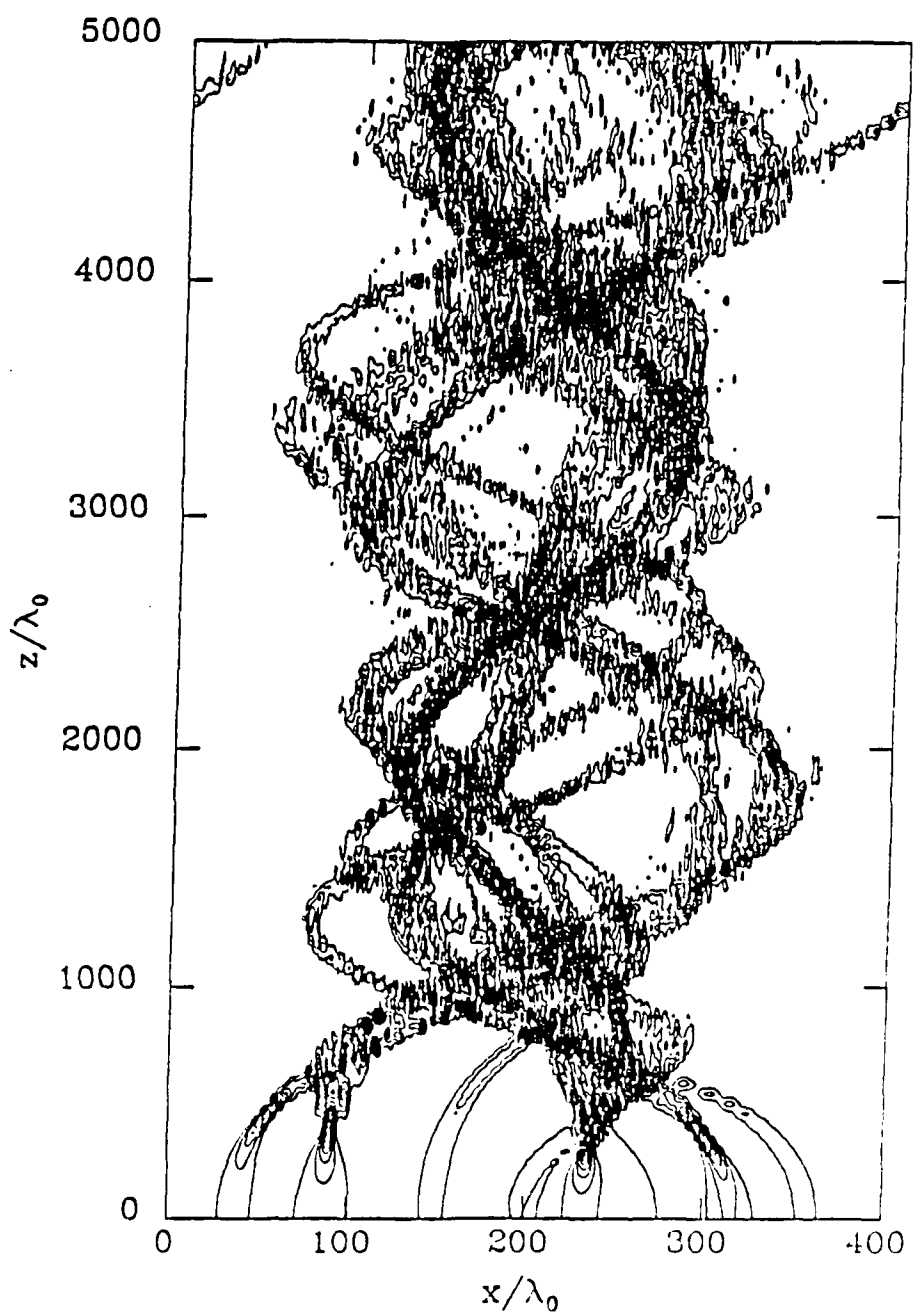


Fig. 10 Contour plot of a generic laser beam undergoing thermal filamentation; contours are at multiples of  $I_0$ . Interaction parameters are:  $\gamma_{T_0} = 1.2 \times 10^{-9}$ ,  $n_e/n_{crit} = 0.5$ ,  $\sigma_{rms} = 0.5$ , and  $F = 20$  optics.

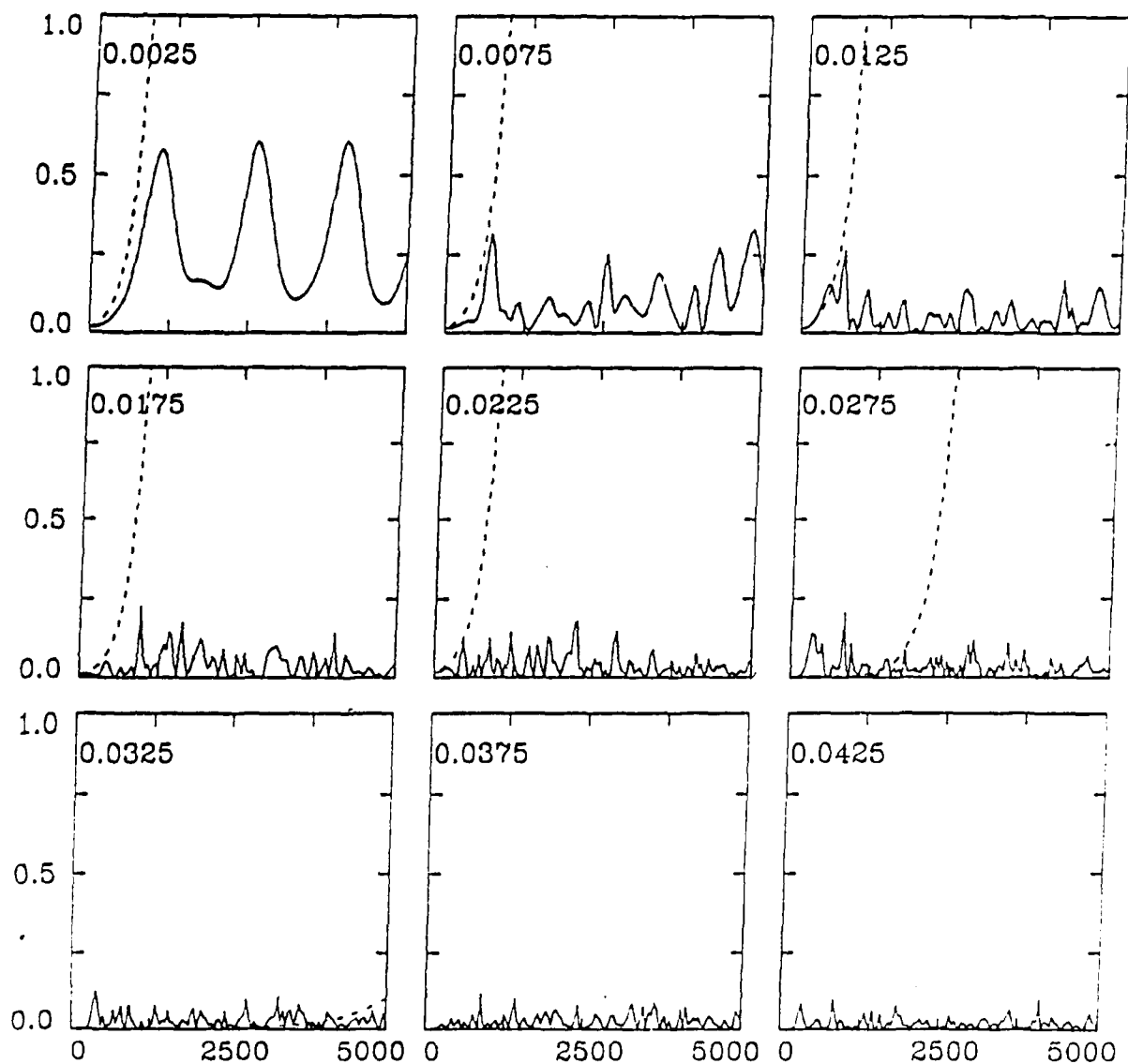


Fig. 11 The Fourier amplitudes of lowest modes of the intensity distribution shown in fig. 10, as a function of the propagation distance. The number in the upper left hand corner of each graph is the value  $k_{\perp}$  of the plotted mode. Horizontal axis is in units of  $\lambda_0$ , and the vertical axis is the normalized mode amplitude  $a(k_{\perp})/a(k_{\perp}=0)$ . The solid line shows the simulation results, while the dotted line shows theoretical predictions (table IV).

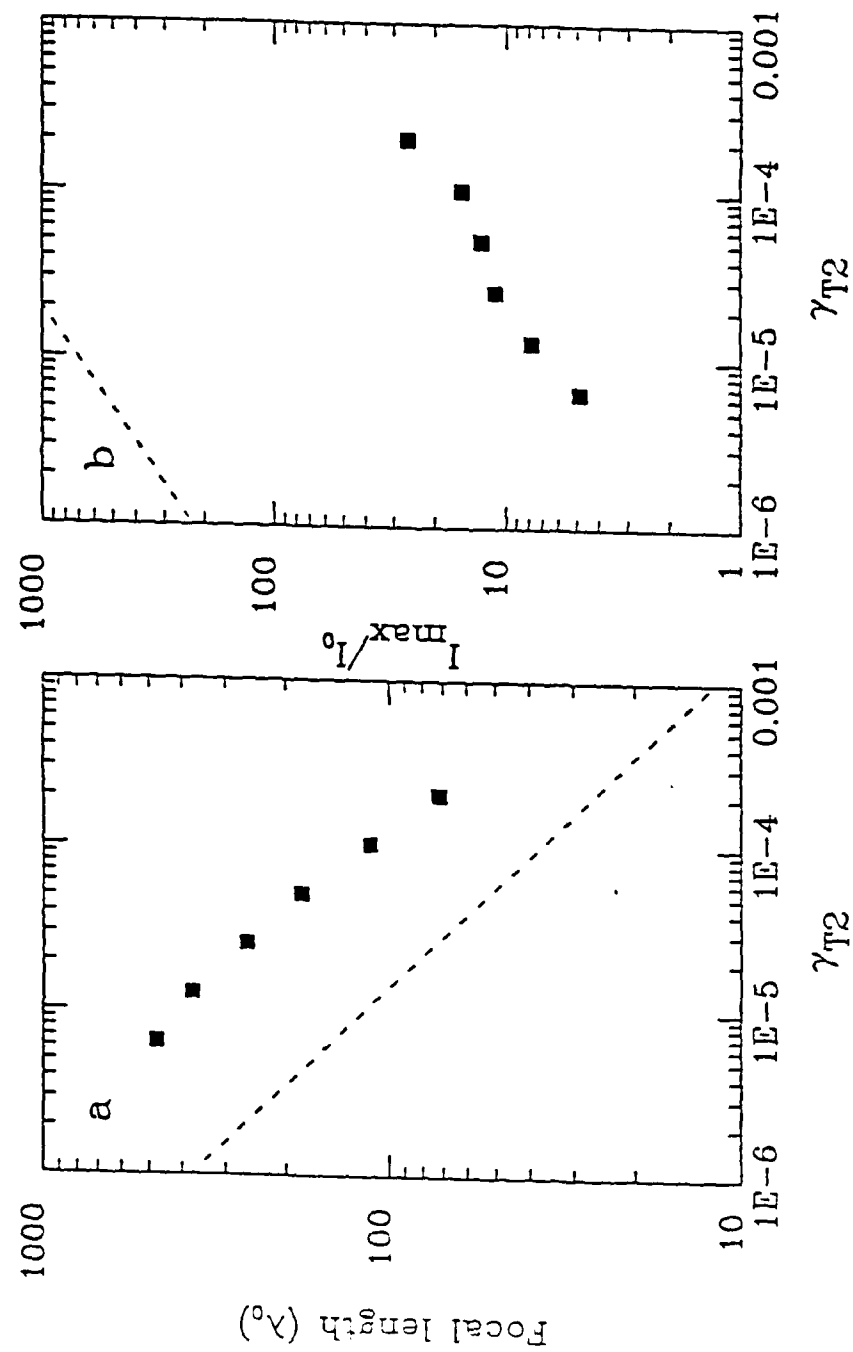


Fig. 12 Variation of  
 (a)  $\text{MAX}_1\{\text{MAX}\{I_x\}\}$  vs.  $\gamma_{T2}$  and (b) focal  
 length  $l$  vs.  $\gamma_{T2}$  for generic laser beams  
 undergoing thermal filamentation. Other  
 parameters are as in fig. 10. The dotted line  
 shows the theoretical result from table I and  
 the appendix.

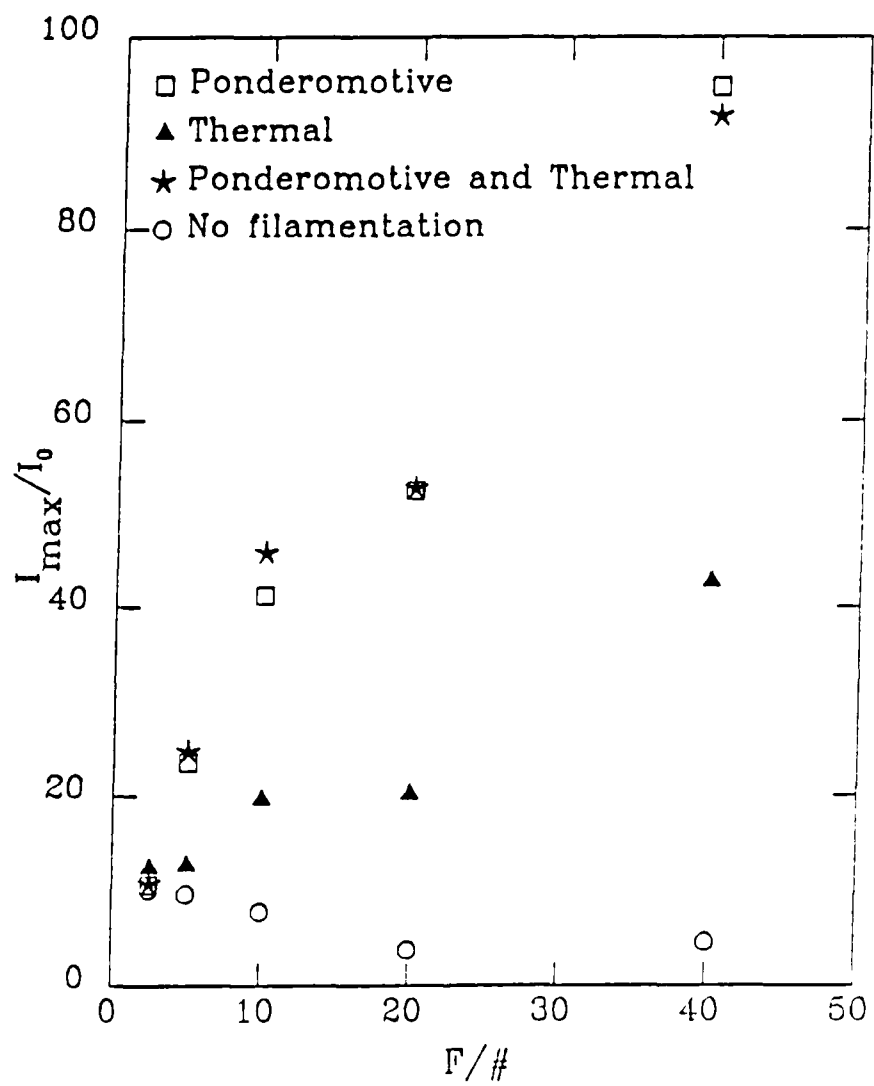


Fig. 13 Variation of  $\text{MAX}\{I\}_{x'}/I_0$  vs. lens F number shows decreased filamentation effects for fast optics. Other parameters are the same as in figs. 7 and 10.

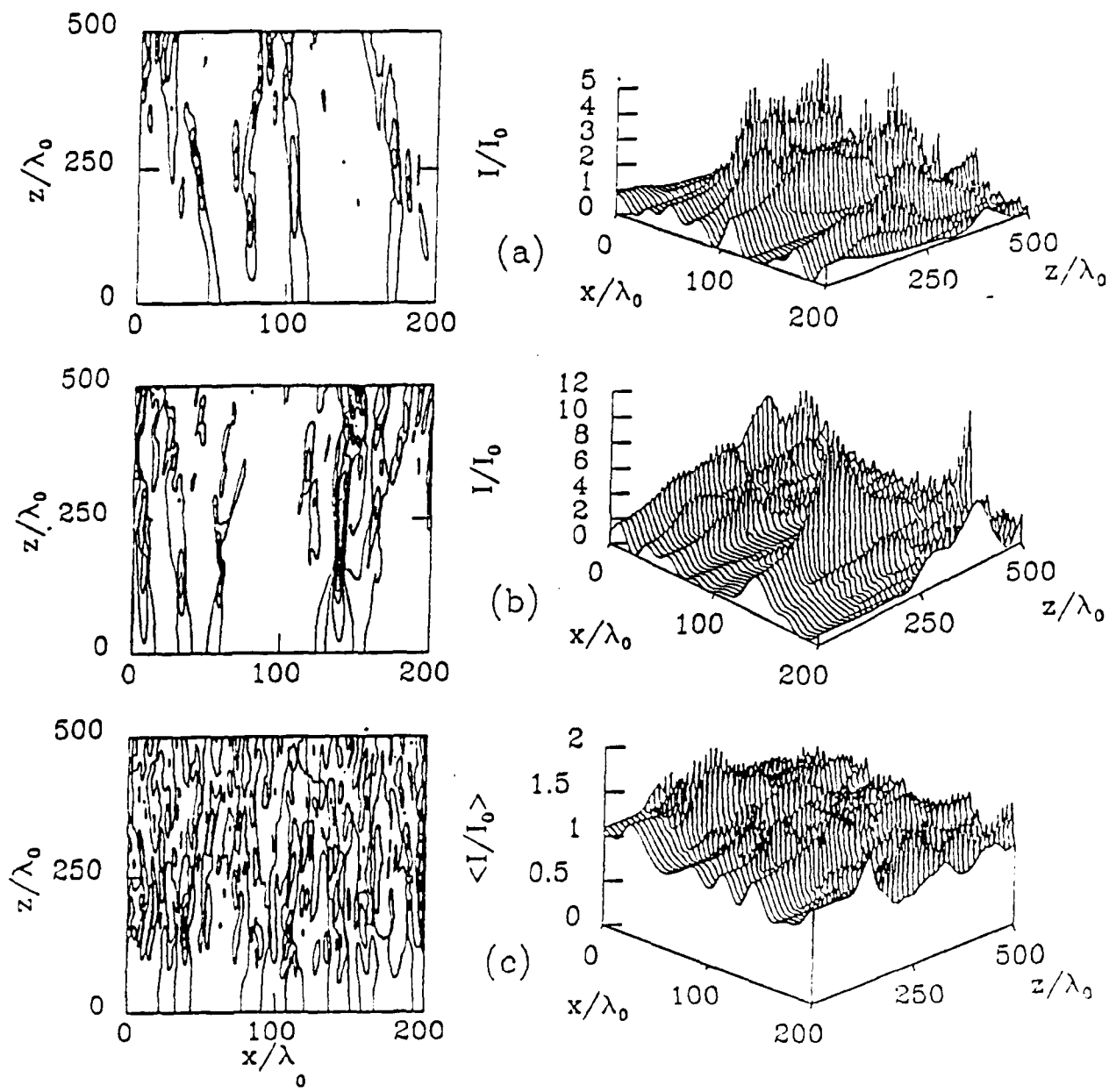


Fig. 14 Ponderomotive filamentation of ISI light in a homogeneous plasma: contour and isometric plots of the intensity distributions. (a) and (b): instantaneous intensities at  $427\tau_c$  and  $347\tau_c$ ; (c) time-averaged intensity vs.  $x,z$  over  $347\tau_c$ . Interaction parameters are:  $\gamma_p = 0.0051$ ,  $\tau_c = 3.2$ ,  $n_z/n_{crit} = 0.5$ , and  $F/20$  optics.

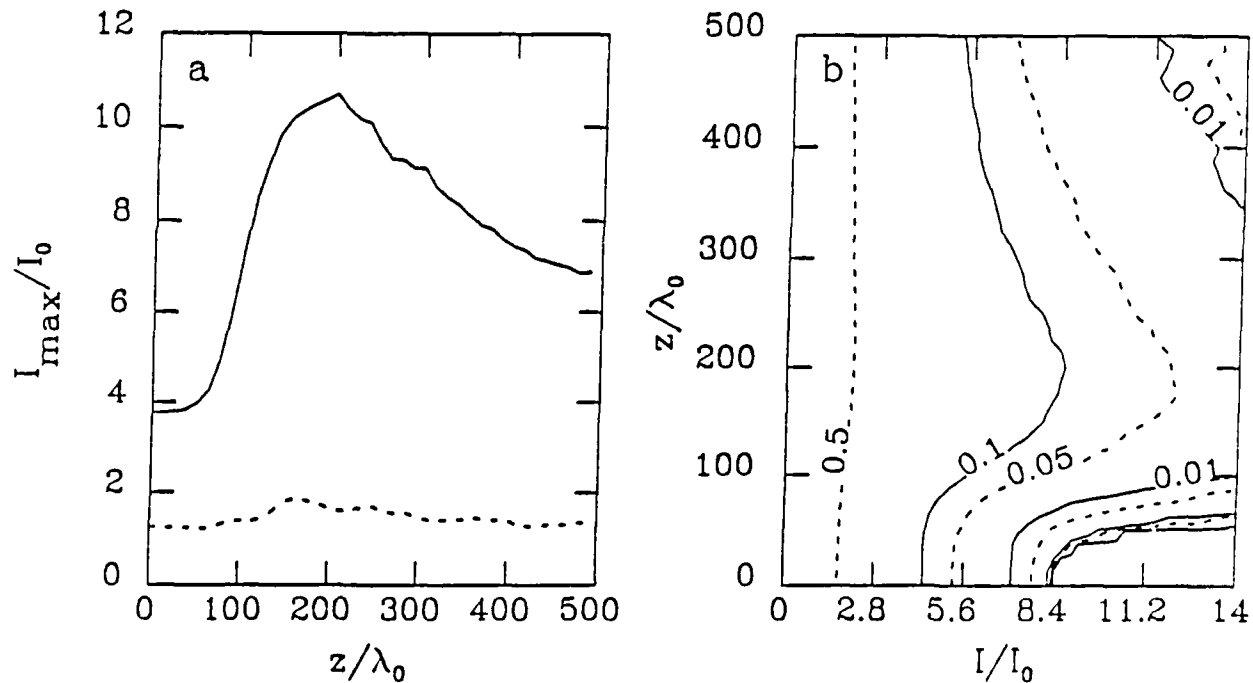


Fig. 15 ISI ponderomotive filamentation in a homogeneous plasma: (a) Normalized maximum intensities  $\langle \text{MAX}\{I\} \rangle / I_0$  (solid line) and  $\text{MAX}\{\langle I \rangle\}_x / I_0$  (dotted line) vs. propagation distance. (b) Contour plot of the integrated energy distribution function, IEDF( $I/I_0$ ), or the fraction of laser energy greater than intensity  $I/I_0$ , as a function of laser propagation distance. Interaction parameters are the same as in Fig. 14.

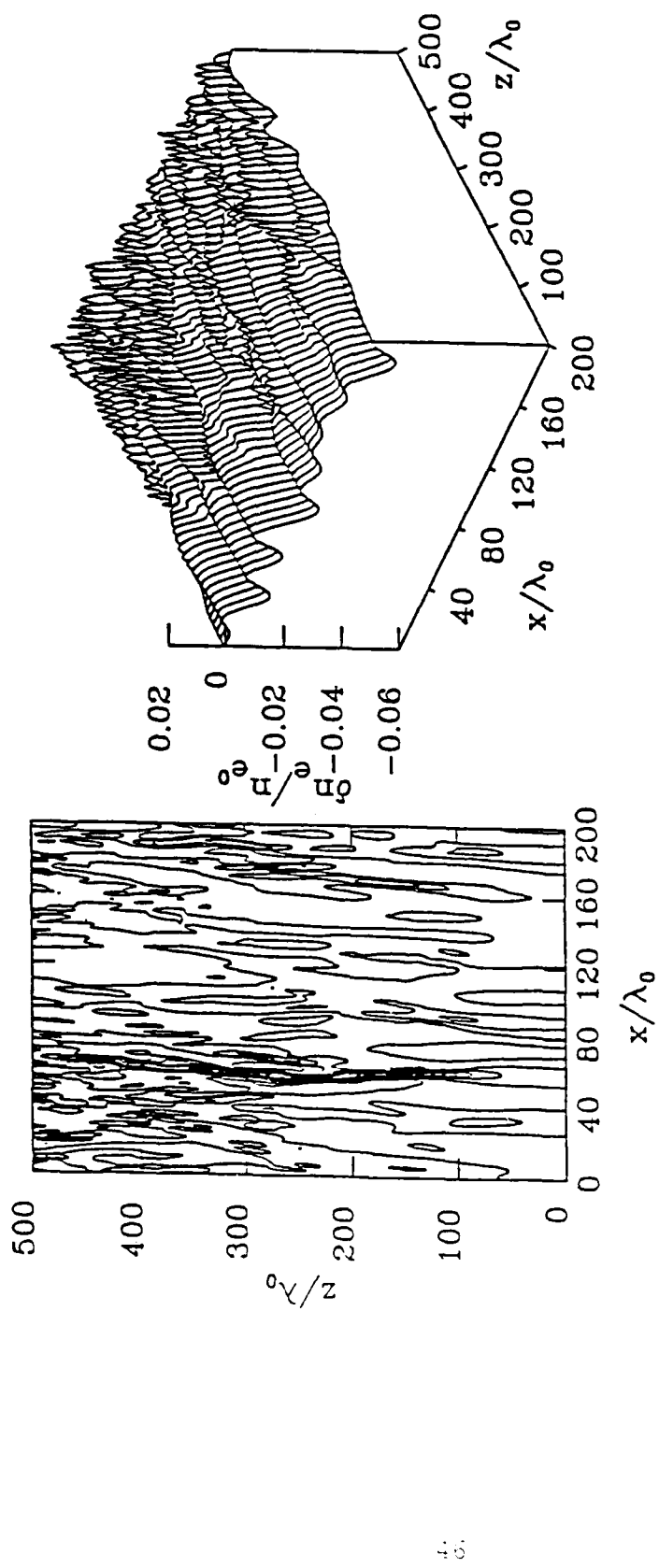


Fig. 16 ISI ponderomotive filamentation in a homogeneous plasma: Contour and isometric plots of the instantaneous density fluctuations in the plasma,  $\delta n(x,z)/n_0$ , at  $84T_c$ . Parameters are the same as in Fig. 14.

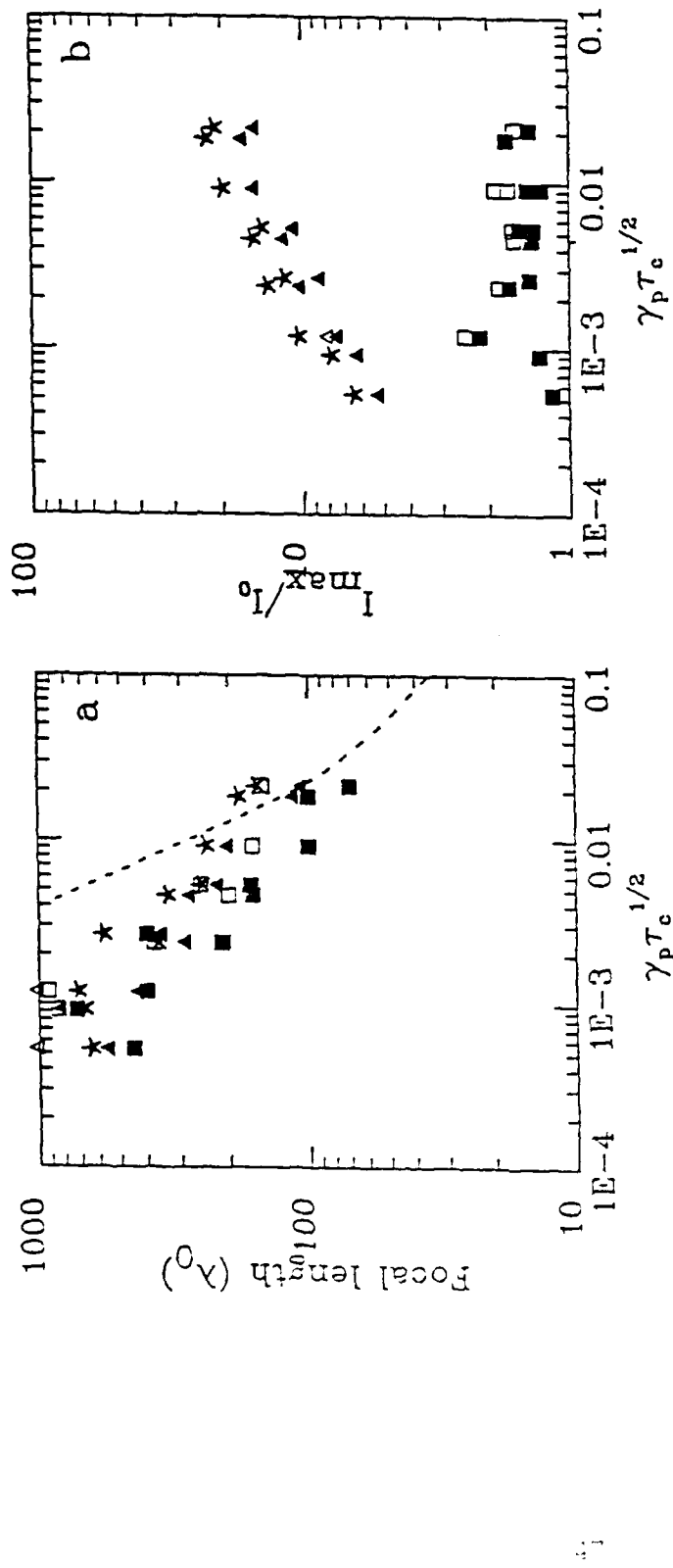


Fig. 17 ISI Ponderomotive filamentation in a homogeneous plasma: Variation of focal lengths vs.  $\gamma_p \tau_c^{1/2}$ . Legend: (i.) (star): Time averaged position of maximum intensity  $\langle \text{MAX}\{\text{MAX}\{I\}\}_x \rangle$ ; (ii.) (filled triangle): position of first intensity peak  $\text{MAX}_1\{\langle \text{MAX}\{I\}_x \rangle\}$  and (open triangle):  $\text{MAX}_1\{\langle \text{MAX}\{I\}_x \rangle\}$ ; (iii.) (filled box): position of first peak  $\text{MAX}\{\langle \text{MAX}\{I\}_x \rangle\}_x$ ; (iv.) (box): position of  $\text{MAX}_1\{\langle I \rangle\}_x$  and (box): position of largest peak  $\text{MAX}\{\langle I \rangle\}_x$ ; (iv.) the dotted line shows the expected values using the results in Table II. All simulations are with  $n/n_{\text{crit}} = 0.5$ , F/20 optics, on a  $200\lambda_0$  wide simulation mesh.

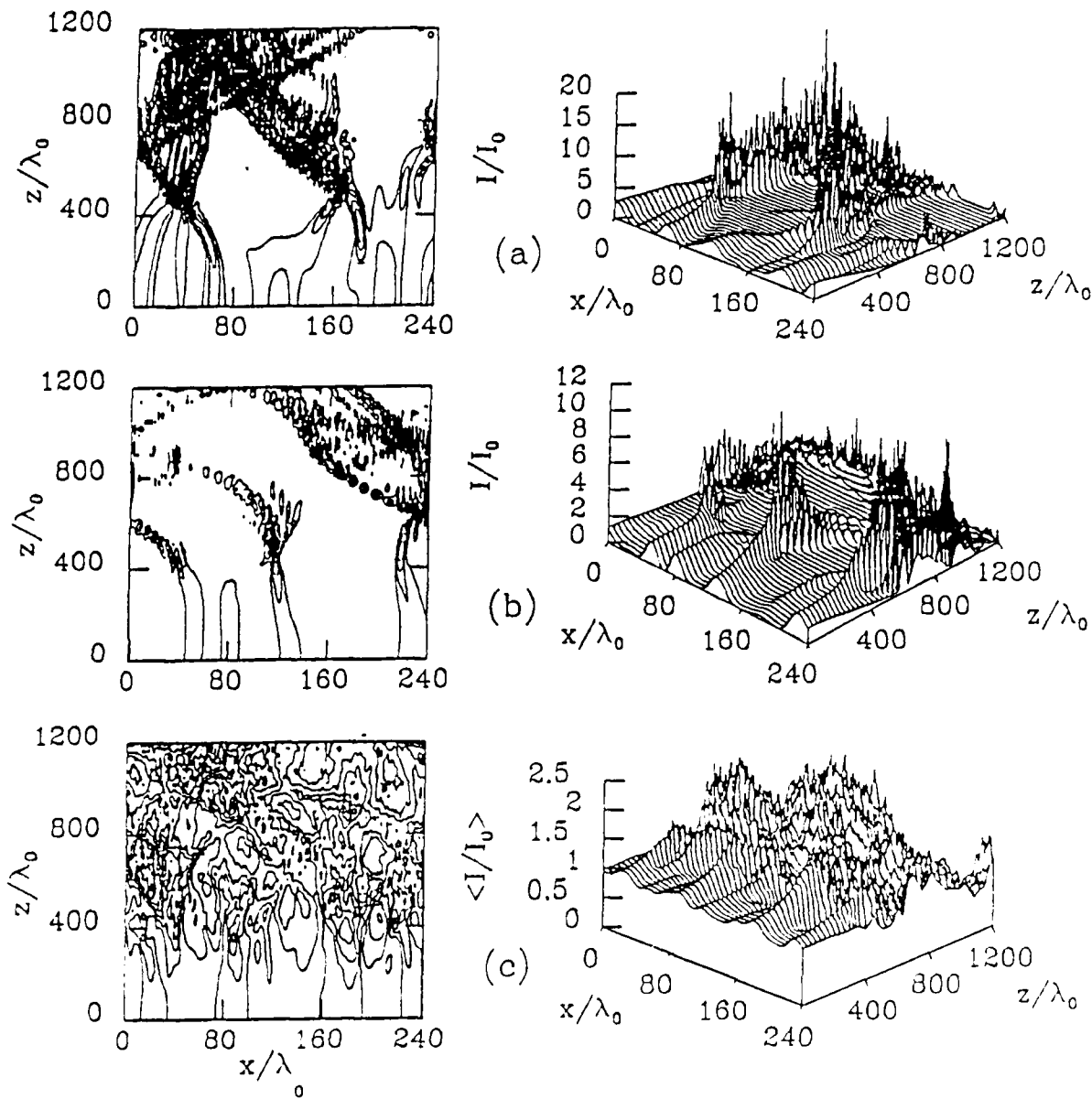


Fig. 18 ISI Thermal filamentation in a homogenous plasma: contour and isometric plots of intensity distributions. (a) and (b): instantaneous intensities at  $125T_c$  and  $250T_c$ ; (c) time-averaged intensity vs.  $x, z$  over  $250T_c$ .  $\gamma_{T2}=2 \times 10^{-3}$ ,  $\tau_c=0.53$ ,  $\gamma_{T1}=3.8 \times 10^{-4}$ ,  $n_{e'}/n_{crit}=0.5$ , and F/20 optics.

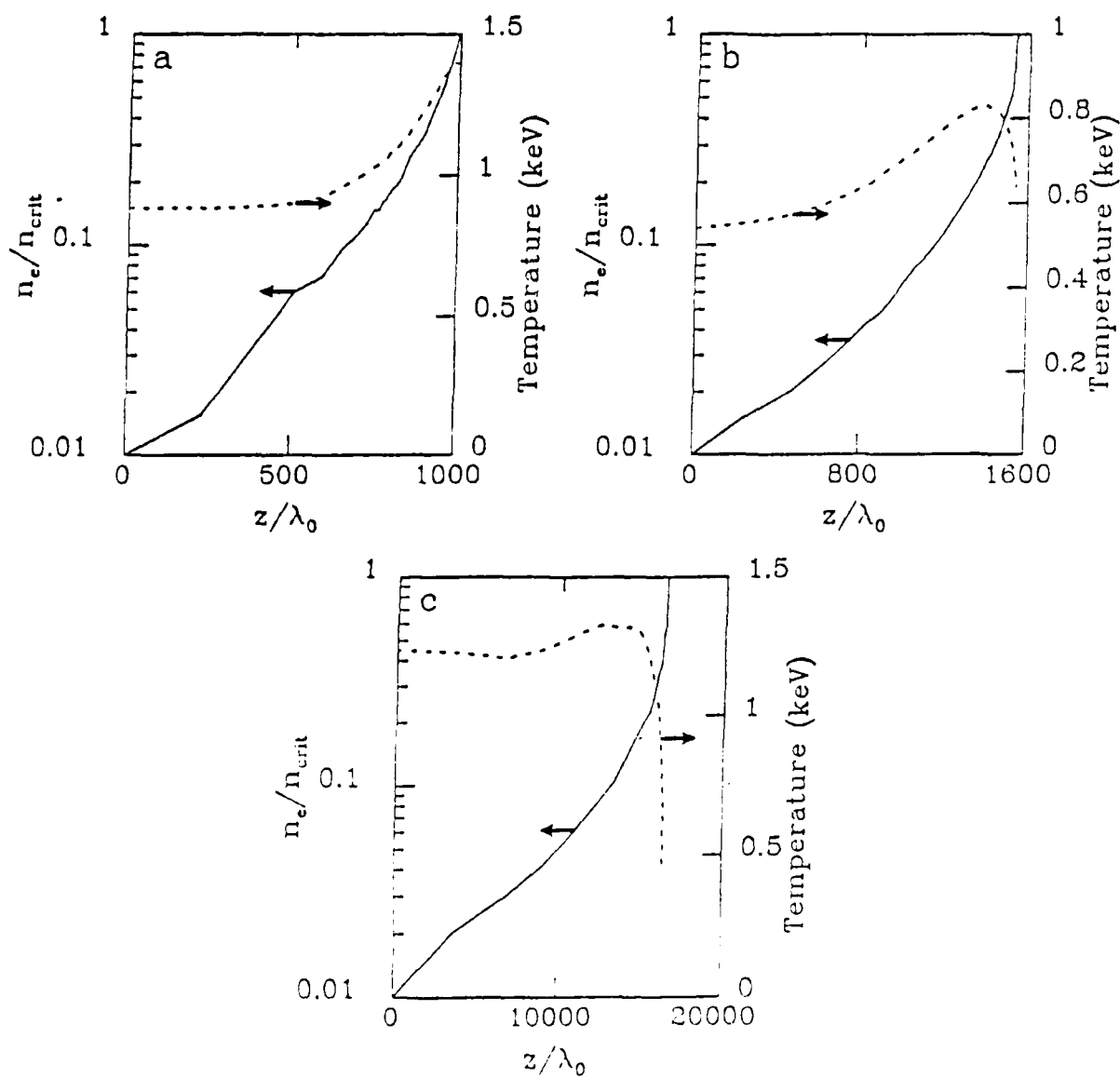


Fig. 22 Density and temperature profiles for laboratory plasmas at different laser wavelengths. (a)  $\lambda_0 = 1.08 \mu\text{m}$ ,  $I_0 = 2 \times 10^{14} \text{ W/cm}^2$ , F/10 optics and a CH foil; (b)  $\lambda_0 = 0.53 \mu\text{m}$ ,  $I_0 = 2 \times 10^{14} \text{ W/cm}^2$ , F/20 optics and a CH foil; and (c)  $\lambda_0 = 0.25 \mu\text{m}$ ,  $I_0 = 3 \times 10^{14} \text{ W/cm}^2$ , F/20 optics and a DT pellet.

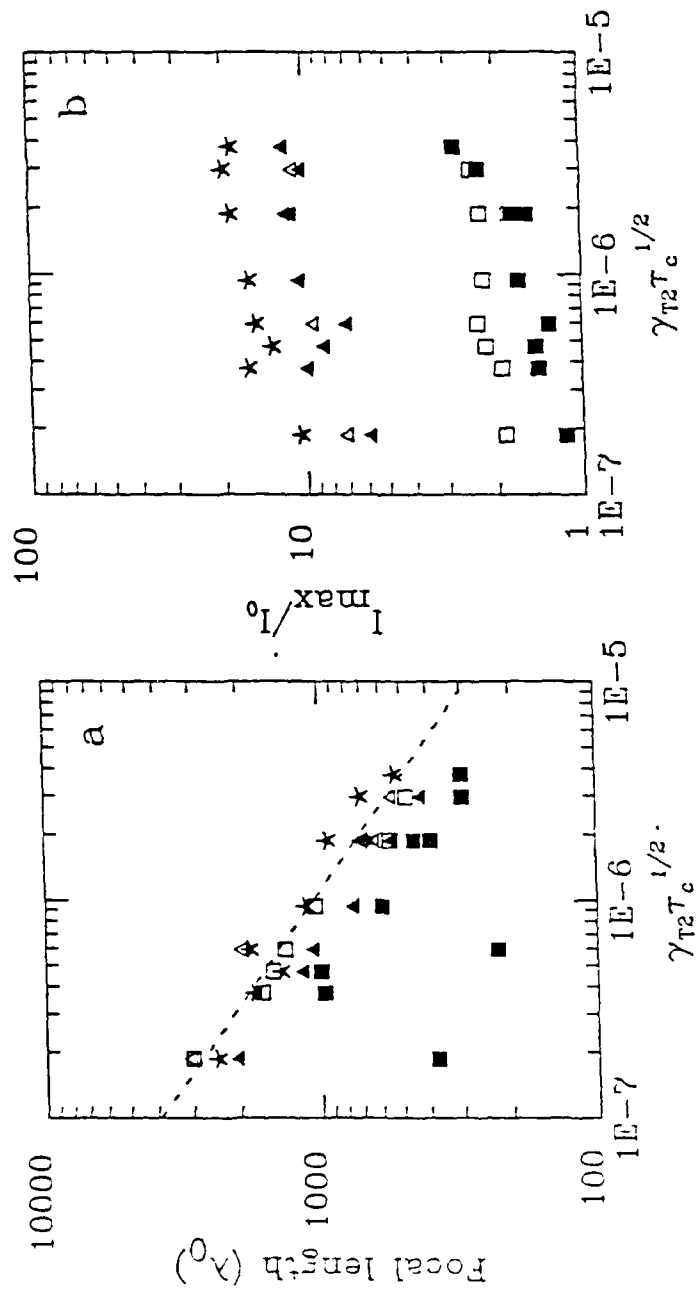


Fig. 21 ISI Thermal filamentation in a homogeneous plasma: Variation of (a) focal lengths and (b) intensity maximum vs.  $\gamma_{\text{tr2}} \tau_c^{1/2}$ . Legend is the same as fig. 17. All runs are with  $n/n_{\text{crit}} = 0.5$ ,  $\gamma_{\text{tr1}} = 3.8 \times 10^{-4}$ ,  $F/20$  optics, on a  $240 \lambda_0$  wide simulation mesh.

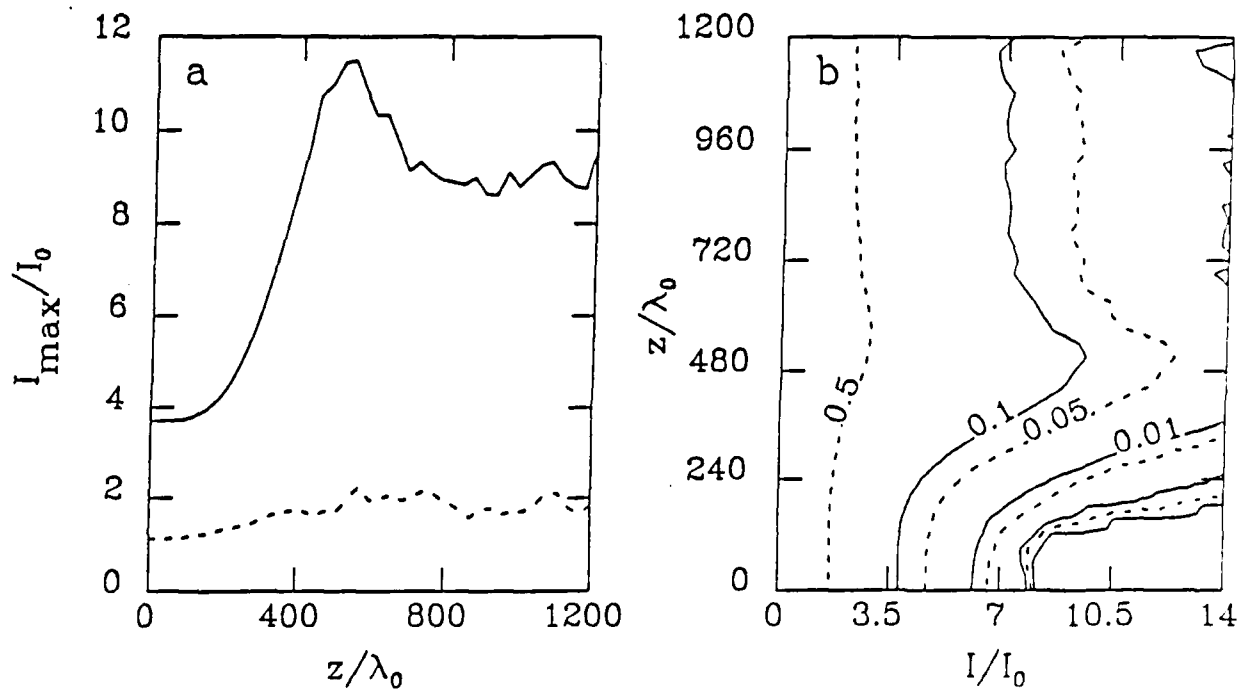


Fig. 20 ISI Thermal filamentation in a homogeneous plasma: (a)  $\langle \text{MAX}\{I\}_x \rangle/I_0$  (solid line) and  $\text{MAX}\{\langle I \rangle_x\}/I_0$  (dotted line) vs. propagation distance,  $z/\lambda_0$ . (b) Contour plot of the integrated energy distribution function  $\text{IEDF}(I/I_0)$  (the fraction of energy greater than a given intensity) as a function of the propagation distance,  $z/\lambda_0$ . From the simulation shown in Fig. 18.

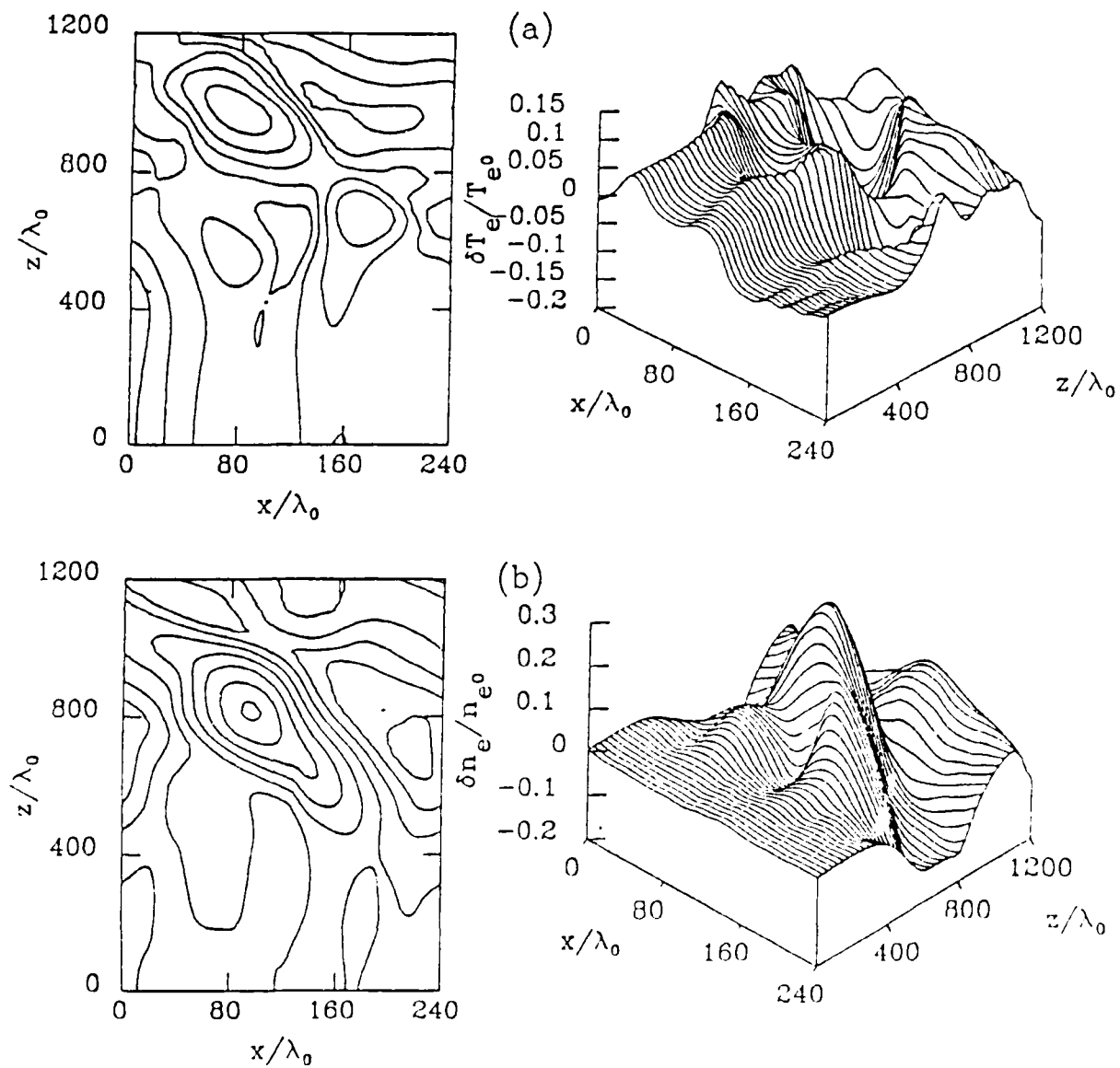


Fig. 19 ISI Thermal filamentation in a homogeneous plasma: contour and isometric plots of the instantaneous (a) temperature and (b) density distributions in the plasma at  $250\tau_e$ , from the simulation shown in fig. 18.

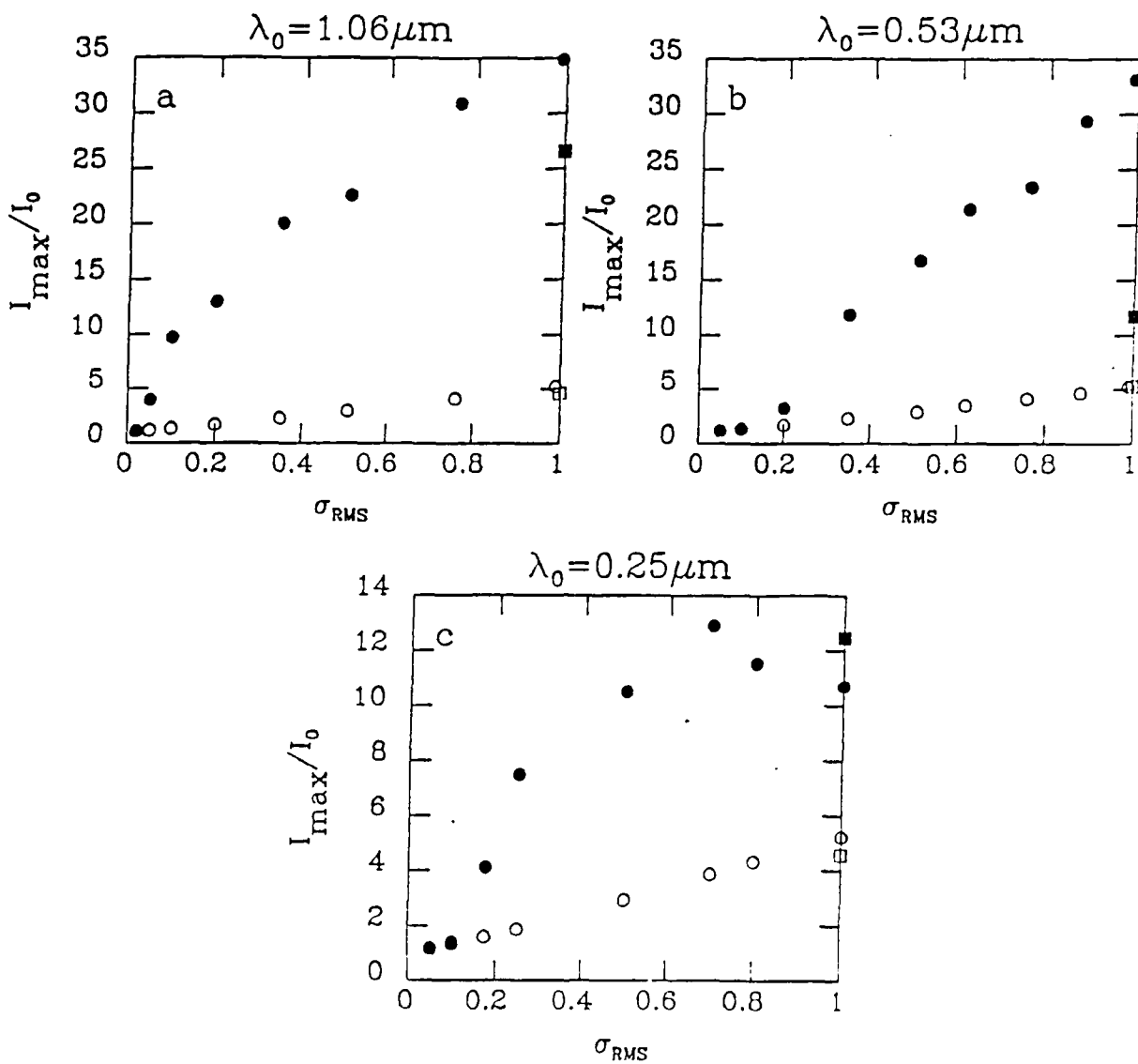


Fig. 23 Results of filamentation of the generic profile lasers for laser wavelengths of (a)  $1.06\mu\text{m}$ ; (b)  $0.53\mu\text{m}$ , and (c)  $0.25\mu\text{m}$  (using density, temperature profiles shown in fig. 22), showing  $\text{MAX}\{I\}_x$  vs.  $\sigma_{\text{rms}}$  of the incident beam. The open circles mark the incident values of  $\text{MAX}\{I(z=0)\}_x$ ; the solid circles are the absolute maximum values of the intensities reached in the plasmas,  $\text{MAX}\{I\}_{x,z}$ . Also shown (square symbols) are the results achieved using the RPS method with F/5 optics (the solid square denotes the value of  $\text{MAX}\{I\}_{x,z}$ , the open square the value of  $\text{MAX}\{I(z=0)\}_x$ ).

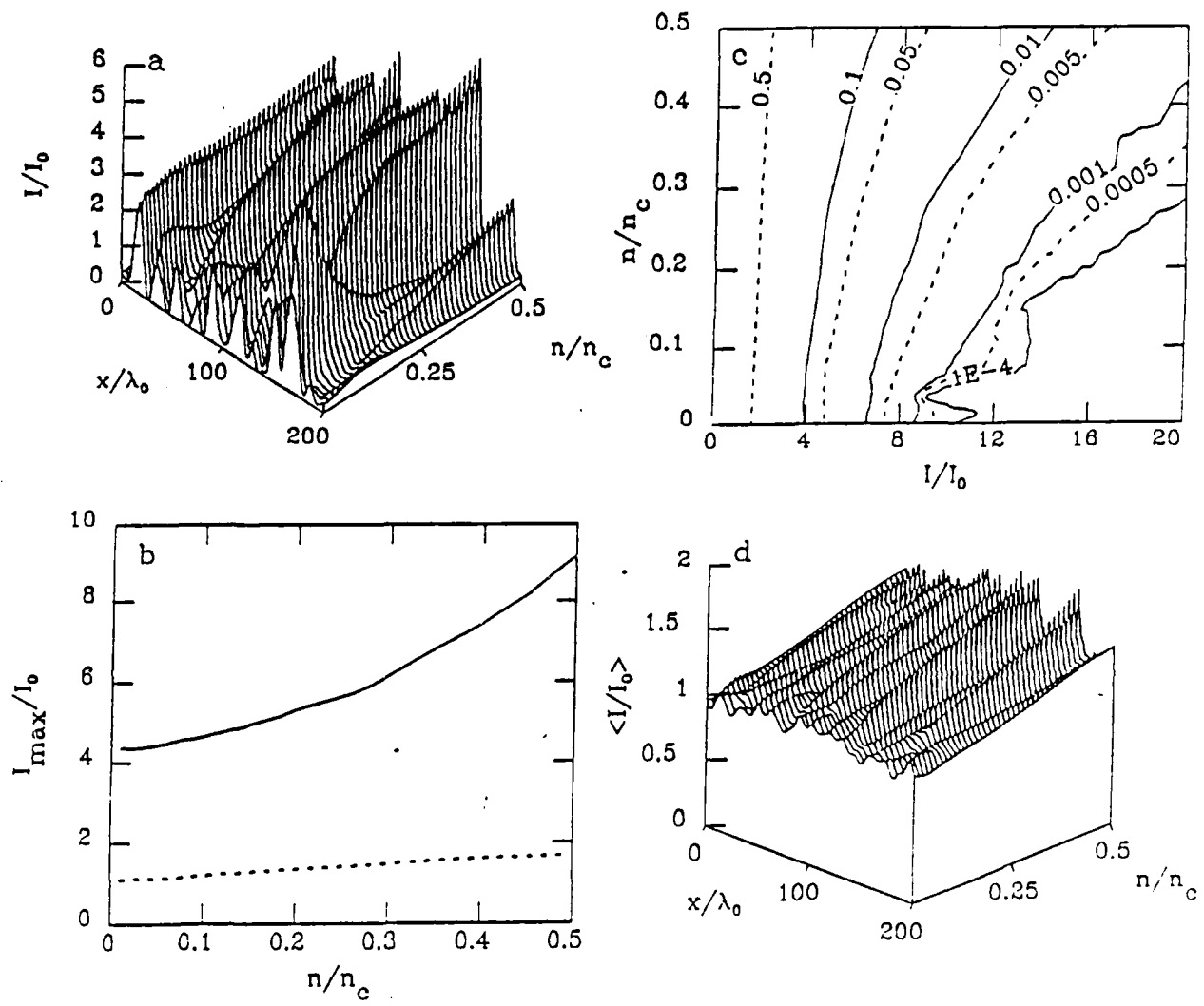


Fig. 24 ISI filamentation at  $1.06\mu\text{m}$  laser wavelength in laboratory plasma fig. 2a.  
 (a) Instantaneous intensity distribution at  $250\tau_{\text{ci}}$ ; (b) time averaged intensity maximum  $\langle \text{MAX}(I) \rangle$  (solid line) and  $\text{MAX}(\langle I \rangle)_x$  (dotted line); (c) contour plot of the integrated energy distribution function (fraction of energy greater than a given intensity  $I/I_0$ ), IEDF( $I/I_0, n/n_c$ ); and (d) time averaged distribution  $\langle I(x,s) \rangle$ .

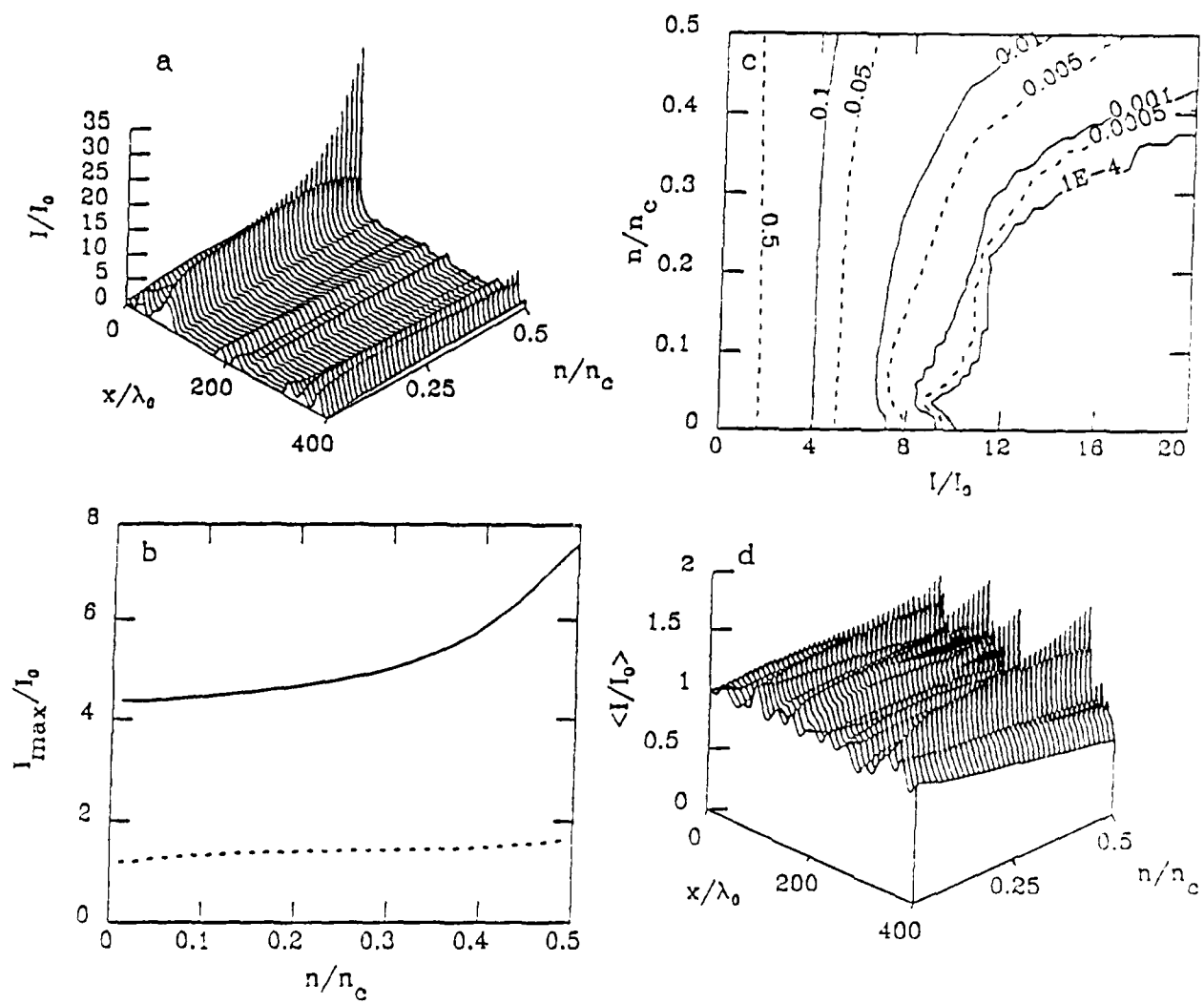


Fig. 25 ISI filamentation at  $0.53\mu\text{m}$  wavelength in laboratory plasma fig. 22b.  
 (a) Instantaneous intensity distribution at  $250T_c$ ; (b) time averaged intensity maximum  $\langle \text{MAX}\{I\} \rangle$  (solid line) and  $\text{MAX}(\langle I \rangle)_x$  (dotted line); (c) contour plot of the integrated energy distribution function (fraction of energy greater than a given intensity  $I/I_o$ ), IEDF( $I/I_o, n/n_c$ ); and (d) time averaged distribution  $\langle I(x,z) \rangle$ .

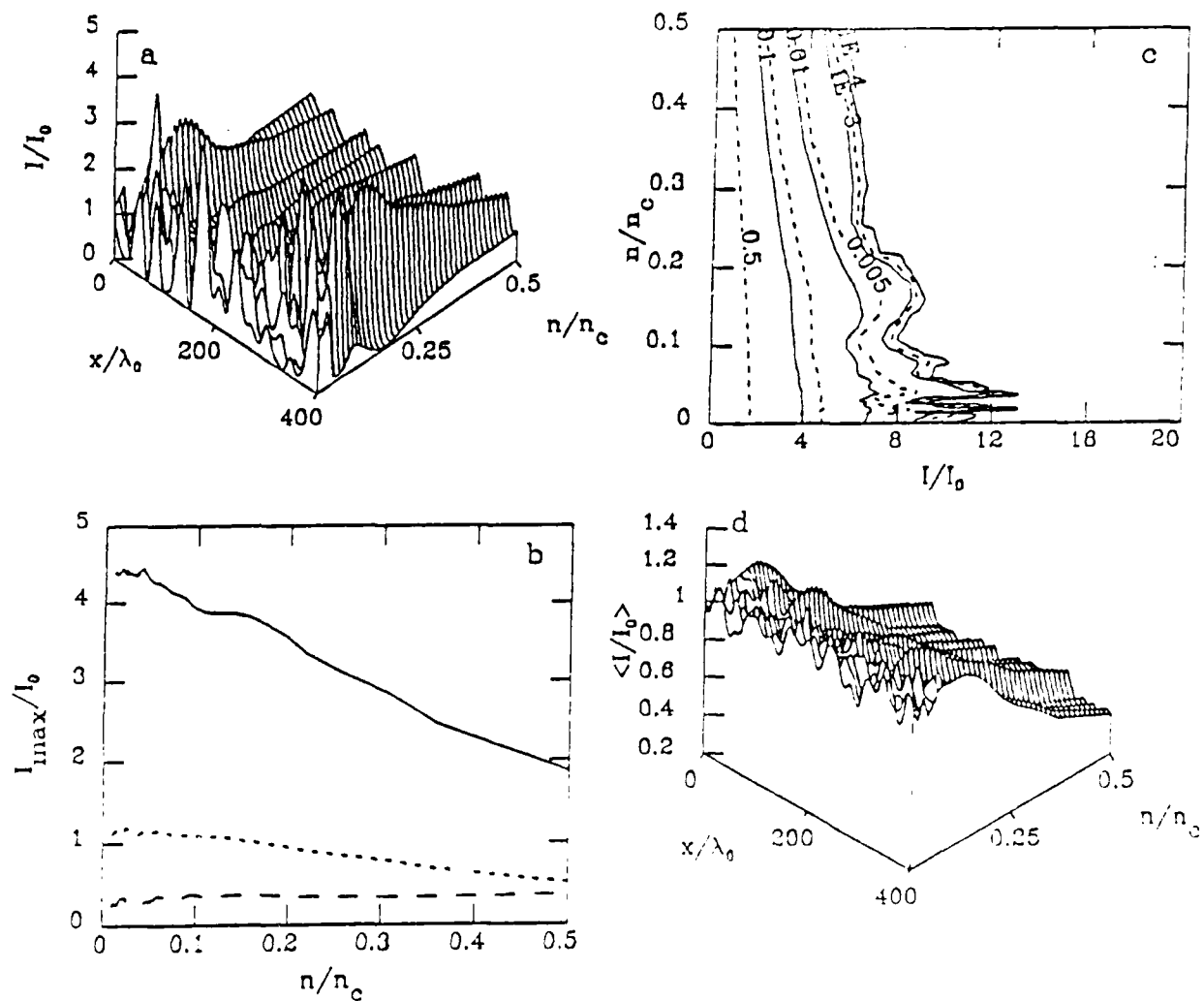


Fig. 26 ISI filamentation at  $0.25\mu\text{m}$  laser wavelength in laboratory plasma (Fig. 22c).  
 (a) Instantaneous intensity distribution at  $250\tau_{\text{c}}$ ; (b) time averaged intensity maximums  $\langle \text{MAX}\{I\}_x \rangle$  (solid line) and  $\text{MAX}\{\langle I \rangle\}_x$  (dotted line), and relative peak-to-valley uniformity  $(\text{MAX}\{\langle I \rangle\} - \text{MIN}\{\langle I \rangle\})/\langle I_{\text{avg}}(s) \rangle$  (dashed line); (c) contour plot of the integrated energy distribution function (fraction of energy greater than a given intensity  $I/I_0$ ),  $\text{IEDF}(I/I_0, n/n_c)$ ; and (d) time averaged distribution  $\langle f(x, s) \rangle$ .

"The Effects of Optical Smoothing Techniques  
on Filamentation in Laser Plasmas"

DISTRIBUTION LIST

Dr. Y. Kato  
Dr. K. Imasaki  
Institute Laser Engineering,  
Osaka University  
Osaka 565, Japan

Dr. John E. Murray  
Dr. John Lindl  
Dr. Eric Storm  
Lawrence Livermore National Laboratory  
P.O. Box 5508  
Livermore, CA 99550

Dr. J.P. Vandevender  
Sandian National Laboratories  
Albuquerque, NM 87185

S. Kahalas  
R. Schriever  
U.S. Dept. of Energy  
Office of Inertial Fusion  
Washington, D.C. 20545

Prof. M. Rosenbluth  
Institute for Fusion Studies  
University of Texas  
Austin, TX 78712

Dr. John McLeod  
Dr. Larry Blair  
MS 548  
Los Alamos National Laboratory  
P.O. Box 1663  
Los Alamos, NM 87545

Dr. William Kruer  
Dr. Bruce Langdon  
Dr. Barbara Lasinski  
Dr. Max Tabak  
Dr. Alex Friedman  
Dr. J. Mark  
L-477  
Lawrence Livermore National Laboratory  
P.O. Box 808  
Livermore, CA 99550

David Whelan  
L-45  
Lawrence Livermore National Laboratory  
P.O. Box 808  
Livermore, CA 99550

Warren Mori  
I-130 Knudsen Hall  
UCLA  
Los Angeles, CA 90024

Dr. R. Sigel  
Abteilung Laser-Plasmen  
Max-Planck-Institut fur Quantenoptic  
Postfach 1513  
Boltzmanstrasse 2  
D-8046  
Garching bei Munchen DB

Dr. Roger Haas  
Applied Physics Dept.  
University of California  
Davis, CA 95616  
Prof. E. Fabre  
Prof. Guy Laval  
Ecole Polytechnique  
F-91128 Palaiseau  
France

Dr. Robert Dautray  
Centre D'etudes de limeil  
Boite Postale No. 27  
94190 Villeneuve, St. Georges  
France

Dr. M. Key  
Dr. F. O'Neill  
Dr. D.J. Nicholas  
Laser Division  
Rutherford Appleton Laboratory  
Chilton, Didcot, Oxon, OX11 0QX, United Kingdom

Dr. G.L. Kulcinski  
Fusion Technology Institute  
University of Wisconsin  
Madison, WI 53706

Dr. S. Skupsky  
Dr. R.S. Craxton  
Dr. R.L. McCrory  
Dr. W. Seka  
Laboratory of Laser Energetics  
University of Rochester  
Rochester, NY 14627

Dr. V. Happer  
Physics Dept.  
Jadwin Hall  
Princeton University  
P.O. Box 708  
Princeton, NJ 08540

Dr. D. Pewitt  
Dr. E. Frieman  
Science Applications Inc. Corp.  
P.O. Box 2351  
La Jolla, CA 92038

Dr. S. Coggeshall  
Dr. Roger D. Jones  
Dr. W.C. Mead  
MS-E531  
Los Alamos National Laboratory  
Los Alamos, NM 87545

L. Vahala  
Physics Dept.  
William & Mary College  
Williamsburg, VA 23185

R. Marchand  
Dept. of Electro. Eng.  
University of Alberta  
Edmonton, Alberta  
Canada

J.P. Matte  
INRS-Energie  
C.P. 1020  
Varennes, QC, J0L 2PO, Canada

Monsier Tudor Wyatt Johnston  
INRS-Energie  
1650 Montee Ste-Julie  
Varennes, QC, J0L 2PO, Canada

Dr. Linda V. Powers  
Dr. R. Berger  
KMS Fusion Inc.  
P.O. Box 1567  
Ann Arbor, MI 48103

Dr. R. Davidson  
Plasma Fusion Center  
Mass. Inst. of Tech.  
NW16-202  
167 Albany St.  
Cambridge, MA 02139

Code 1220 1 cp.

Code 2628 22 cps.

Director of Research  
U.S. Naval Academy  
Annapolis, MD 21402 2 cps.

A. Schmitt  
Code 4730 30 cps.

Code 4700 26 cps.

END

FILMED

MARCH, 1988

DTIC